Characterisation of Supramolecular Structures by Novel Recoupling Methods in Solid-State NMR

Dissertation
zur Erlangung des Grades

"Doktor der Naturwissenschaften"

am Fachbereich Chemie und Pharmazie der
Johannes Gutenberg-Universität
in Mainz

Anke Hoffmann
geboren in Freiburg

Mainz 2005

Contents

Chapter 1

Introduction

In the field of nanotechnology, particular interest is focused on the controlled design of materials whose functionality arises from, or is supported by, their structure on the nanoscale. To arrive at such nanostructured materials, classical approaches of chemical synthesis which are primarily concerned with the molecular structure rather than the "superstructure" adopted by the molecules have to be overcome. Therefore, the principles of supramolecular chemistry have attracted considerable interest in this context.

In the last 25 years, supramolecular chemistry [Lehn 78] has developed into a rapidly growing field of science that deals with the design of complex materials based on self-assembly of molecular building blocks via non-covalent interactions. Where technological and physical limitations may soon prevent the continuing miniaturisation of e.g. electronic devices via current "top-down" lithographic approaches, supramolecular self-assembly opens up the possibility of fabricating ordered nanoscale structures via a "bottom-up" approach. The self-assembly, structure, and functionality of these systems is mainly controlled by secondary-interactions, such as hydrogen-bonding, π-interactions and metal-ligand interactions.

Hence, understanding these interactions is crucial in order to control and direct the self-assembly process, to produce materials with predictable structure and properties and, finally, to improve known and design new materials. As supramolecular systems often lack long-range order and can be partially mobile, diffraction techniques provide only limited insight and full crystal structures are usually not available. To fill this gap, solid-state nuclear magnetic resonance (NMR) spectroscopy has proven to be a powerful, indispensable method for the investigation of non-crystalline materials, as it provides information on the local structure and does not rely on long-range order. In addition,

it can serve as a means to study dynamics over a large range of correlation times from about 10^{-10} s to 10 s [Schmidt-Rohr 94].

NMR benefits from the vastly different resonance frequencies of nuclear isotopes, which make it a highly selective method. Furthermore, the resonance frequencies are influenced by the local electronic structure and, in this way, render NMR sensitive to the chemical structure. At the same time, however, solid-state NMR spectra usually consist of severely broadened lines due to the anisotropic internal interactions, such as dipole-dipole or the quadrupole couplings. It was therefore rarely possible to obtain sufficient resolution in, e.g., proton NMR spectra of complex solid materials, until, in the 1950s, Andrew [Andrew 58] and Lowe [Lowe 59] introduced a technique where the sample is rapidly spun about an axis tilted with respect to the static magnetic field $\underline{B}_0$ by an angle $\theta_{\mathrm{M}} = 54.7°$, the so-called *magic angle*. Thereby, the anisotropic interactions are averaged to zero. This provides spectral resolution in solid-state NMR, but this is accomplished at the expense of a wealth of information on the geometry of the sample, which is inherent to the anisotropic interactions: The dipole-dipole interaction between two nuclei has an inverse cubed dependence on the internuclear distance and, hence, can be used to determine internuclear distances or distance constraints. The quadrupole interaction tensor is proportional to the electric field gradient, and is therefore sensitive to the local charge distribution. The anisotropy of both, the dipole-dipole interaction and the quadrupole interaction, renders them sensitive to molecular motion and orientation.

In the last decades, numerous solid-state NMR techniques have been developed which selectively re-introduce, i.e. "recouple", these interactions in order to retain the structural information under magic-angle spinning [Gullion 97, Lee 95, deAzevedo 99, Dusold 00, Schnell 01a, Saalwächter 02, Stejskal 77, Blümich 90, Terao 86]. In this context, the work presented in this thesis is concerned with the development of recoupling techniques that are applicable under fast MAS conditions, i.e., at sample spinning frequencies of about 30 kHz, which are only available for routine studies since about five years.

Chapter 2 reviews the general theoretical background of solid-state NMR as well as the experimental techniques used in this thesis. **Chapter 3** is devoted to the development of new and the improvement of existing recoupling methods. A new two-dimensional ^{2}H NMR experiment, performed under off-magic-angle spinning, is presented, which allows for site-selective determination of quadrupole coupling parameters in samples deuterated at multiple sites. Furthermore, it is shown that ^{7}Li -^{7}Li dipolar recoupling NMR techniques provide the possibility to investigate the electronic environment and mobility on lithium ions, exemplified on lithium intercalated into TiO_2. In the last section of

chapter 3, the precision of proton-carbon distance measurements, using the REREDOR recoupling technique, will be discussed.

In organic solids and supramolecular systems, protons are an especially sensitive probe for the investigation of secondary interactions. However, from NMR experiments alone, usually only qualitative information on these interactions is accessible, and in large systems the distinction and assignment of resonance lines can be obscured. It has been found that the combination of solid-state NMR and quantum-chemical calculations can help to overcome these problems [Ochsenfeld 01, Sebastiani 03, Brown 01, Ochsenfeld 02], especially as quantum-chemical calculations on large systems have become more and more feasible. In **chapter 4** two examples of this combined experimental and theoretical approach will be given, namely the investigation of inclusion of solvent molecules in calix[4]hydroquinone nanotubes and the helical stacking of C_3-symmetrical discs.

Chapter 2

Theory

The magnetic moment of nuclear spins is about three orders of magnitude smaller than that of electrons and is therefore not visible in static measurements in terms of a macroscopic net magnetisation. For frequency-dependent experiments in static magnetic fields the situation is completely changed, since the resonance frequencies of electrons and nuclei occur in two clearly separated frequency bands. This goes even further, as the differences of nuclear magnetic moments of various isotopes are large enough to facilitate selective excitation and, in this way, to distinguish the isotopes. In NMR experiments, resonance frequencies of transitions between ZEEMAN energy levels, and thus the corresponding differences of the energy levels, are measured. The precision of the measurements is high enough to resolve energy shifts of the ZEEMAN levels in the range of ppm, caused by the interactions of the nuclei with local fields. In this way, the nuclei probe their environment and reveal dynamic and structural information on the sub-molecular scale.

The first NMR experiments were independently conducted in 1946 by Bloch [Bloch 46] and Purcell [Purcell 46]. In the beginning, resonances were determined by varying the magnetic field under continuous r.f. irradiation (CW methods). This technique was later replaced by measuring the response of the system on a short high power r.f. pulse and obtaining the spectrum as the Fourier transformation of the response (FT method). This opened up the possibility to manipulate the spin system by r.f. pulses prior to detection and to perform multi-dimensional NMR experiments. Today, the only reminder of CW experiments is a reverse plotting of the frequency axes in NMR spectra.

The first part of this chapter provides the background required for the theoretical description of NMR experiments. In the second part, some basic NMR experiments, as well as the more advanced methods used in this thesis will be introduced. For a more detailed

description the interested reader is referred to the literature [Abragam 61, Slichter 96, Mehring 83, Schmidt-Rohr 94, Ernst 87].

2.1 Quantum Mechanical Description of a Spin System

In NMR experiments the time dependent evolution of the net magnetisation of an ensemble of N nuclear spins I^i is measured to gain information on the various interactions of the nuclei. Such a system is usually in a mixed state, i.e. the exact wave function of the system is not known. The mixed state can be considered as an incoherent mixture of pure states $|\alpha^{(i)}\rangle$ with statistical weight W_i, and is described by a density operator

$$\hat{\rho} = \sum_i W_i |\alpha^{(i)}\rangle\langle\alpha^{(i)}| \tag{2.1}$$

The density operator is a statistical operator acting on the product HILBERT space H, i.e. the tensor product of the HILBERT spaces $\mathrm{H}^{(i)}$ of the single spins I^i.

$$\hat{\rho} : \mathrm{H} \to \mathrm{H}, \;\; \hat{\rho} = \hat{\rho}^+, \;\; \mathsf{Tr}[\hat{\rho}] = 1 \tag{2.2}$$

The expectation value of an operator $\hat{A}$ is obtained by taking the trace of its product with the density matrix

$$\langle \hat{A} \rangle_{\hat{\rho}} = \mathsf{Tr}[\hat{\rho}\hat{A}]. \tag{2.3}$$

The time dependence of the density matrix in the SCHRÖDINGER picture is given by the LIOUVILLE-VAN NEUMANN equation

$$\dot{\hat{\rho}}(t) = -i[\hat{H}, \hat{\rho}(t)] \tag{2.4}$$

which can be generally solved by

$$\hat{\rho}(t) = \hat{U}(t)\hat{\rho}(0)\hat{U}^+(t). \tag{2.5}$$

If the Hamiltonian does not explicitly depend on time, the propagator $\hat{U}$ takes the simple form

$$\hat{U}(t) = e^{-i\hat{H}t}. \tag{2.6}$$

For an explicitly time-dependent Hamiltonian the situation is further complicated by the fact that the Hamiltonian does not commute with itself at arbitrary times and the propagator is given by

$$\hat{U}(t) = \hat{T} e^{-i \int_0^t dt' \hat{H}(t')} \tag{2.7}$$

where the Dyson time ordering operator $\hat{T}$ ensures a proper time order. A way to treat explicitly time-dependent Hamiltonians is average Hamiltonian theory (AHT), which will be discussed later when dealing with time-dependent Hamiltonians.

In Eq. (2.4), $\hat{\rho}(0)$ denotes the density operator at time zero, which must be a known starting point. Starting with a spin ensemble in thermal equilibrium the initial state is a BOLTZMANN distribution of the spins among the different energy levels of the system. Since the ZEEMAN interaction usually by far exceeds all other interactions in a spin system only the ZEEMAN energy levels are taken into account for calculating the initial state. This will be further discussed in Section (2.2.1)

As a convention, NMR Hamiltonians are usually given in units of $\hbar$, in which case they have the dimension of reciprocal time, i.e., frequency.

2.2 Solid State NMR Interactions

In NMR experiments, interactions of the nuclei with electric and magnetic fields are observed. These fields can either originate from the external apparatus, such as the external static magnetic field and the oscillating magnetic field of the r.f. pulses, or they can originate from the sample itself. In the first case, one speaks of external spin interactions, while in the second case the term internal spin interactions is used. In solids the internal interactions that have to be considered are the diamagnetic shielding of the electrons (chemical shielding), the interaction of a nuclear spin with the magnetic field of the other spins (dipole-dipole interaction) and the interaction of the electric quadrupole moment of nuclei with $I > \frac{1}{2}$ with the electric field gradient (quadrupole interaction). In contrast to solution NMR, the J-coupling (the interaction of the nuclear spins via the electrons) is usually neglible in solids.

The general form of the solid-state NMR Hamiltonian is a sum of the Hamiltonians of the various interactions of the nuclei:

$$\begin{aligned} \hat{H} &= \hat{H}_{\text{ext}} + \hat{H}_{\text{int}} && (2.8)\\ &= \hat{H}_{\text{Z}} + \hat{H}_{\text{RF}} + \hat{H}_{\text{Q}} + \hat{H}_{\text{CS}} + \hat{H}_{\text{D}} && (2.9)\\ &= \sum_i \hat{H}_{\text{Z}}^{(i)} + \sum_i \hat{H}_{\text{RF}}^{(i)} + \sum_{i,I^{(i)}\geq 1} \hat{H}_{\text{Q}}^{(i)} + \sum_i \hat{H}_{\text{CS}}^{(i)} + \sum_{i\neq j} \hat{H}_{\text{D}}^{(i,j)} && (2.10) \end{aligned}$$

To simplify the notation, in the following the spin system will be restricted to the number of nuclei necessary to describe the interaction of interest.

The internal spin interactions are usually anisotropic, i.e. they exhibit a dependence on spatial orientation of the crystallites/molecules with respect to the laboratory frame. Hence, their space part can be represented by second-rank Cartesian tensors. The Hamiltonian then takes the form [Mehring 83]

$$\hat{H} = \underline{\hat{I}} \cdot \underline{\underline{A}} \cdot \underline{L} = \begin{pmatrix} \hat{I}_1 & \hat{I}_2 & \hat{I}_3 \end{pmatrix} \begin{pmatrix} a_{11} & a_{12} & a_{13} \\ a_{21} & a_{22} & a_{23} \\ a_{31} & a_{32} & a_{33} \end{pmatrix} \begin{pmatrix} L_1 \\ L_2 \\ L_3 \end{pmatrix} \qquad (2.11)$$

where $\underline{\hat{I}}$ is the spin angular-momentum operator of a nucleus, and $\underline{L}$ can be the spin angular-momentum operator of the same nucleus (quadrupole interaction), of a second nucleus (dipole-dipole interaction), or it can be the magnetic field vector $\underline{B}_0$ (chemical shielding).

A second-rank tensor can be decomposed into three components.

$$\underline{\underline{A}} = a \cdot \underline{\underline{1}} + \begin{pmatrix} 0 & b & c \\ -b & 0 & d \\ -c & -d & 0 \end{pmatrix} + \begin{pmatrix} e & g & h \\ g & f & i \\ h & i & -e-f \end{pmatrix} \tag{2.12}$$

The first part denotes the isotropic (i.e. orientation independent) contribution $a = \frac{1}{3}\mathsf{Tr}[\underline{\underline{A}}]$. The second term is a traceless and antisymmetric matrix, and the third term is a traceless and symmetric matrix.

Though the Cartesian tensor representation is quite comprehensive, it is not very convenient to work with. First, it is not irreducible and, second, the transformations that usually need to be performed are rotations, which in the case of Cartesian tensors involve costly matrix multiplications. It is therefore advantageous to work with irreducible spherical tensors that transform identically to the spherical harmonics, i.e. a rotation is performed by a linear combination of the components.

As a further simplification, the space part of the interaction $\underline{\underline{A}}$ and the spin part of the interaction are separately transformed into spherical tensors. This is done since most transformations only affect either the spin part (e.g. transformations due to r.f. pulses) or the space part (e.g. transformations due to a mechanical rotation of the sample) of the interaction. The Hamiltonian can then be written as

$$\hat{H} = \sum_{l=0}^{2} \sum_{m=-l}^{m=l} (-1)^m A_{l,m} \hat{T}_{l,-m} \tag{2.13}$$

where $\hat{T}$ is the spherical tensor operator representation of the spin part. A description of irreducible spherical tensors and their transformations is given in Appendix C.

2.2.1 ZEEMAN Interaction and Secular Approximation

In the presence of an external magnetic field the otherwise degenerate $(2I+1)$ energy levels of a nuclear spin split into $(2I+1)$ ZEEMAN energy levels. The Hamilton operator of the nuclear ZEEMAN interaction reads

$$\hat{H}_{\mathrm{Z}} = -\gamma\hbar \underline{B}_0 \cdot \underline{\hat{I}} \overset{\underline{B}_0 \| \underline{e}_z}{=\!=} -\gamma\hbar B_0 \hat{I}_z = -\omega_{\mathrm{L}} \hat{I}_z \tag{2.14}$$

where γ is the gyromagnetic ratio of the observed nucleus. It is common practice to use an axis system for which the z-axis is chosen to be parallel to the direction of the static

magnetic field. The angular frequency ω_L, the so-called LARMOR frequency, describes a precession of the spins around $\underline{B}_0$. The magnetic field strength of a NMR machine is usually given in terms of the LARMOR frequency for protons, e.g. 700 MHz corresponding to a magnetic field strength of 16.4 T.

For high magnetic fields, as they are used in NMR today, the ZEEMAN interaction by far exceeds the internal interactions. An exception are strong quadrupole couplings that can be of the same order as the ZEEMAN interaction. However, the quadrupolar nuclei dealt with in this thesis (^{2}H , ^{7}Li) only exhibit small quadrupolar couplings. The dominance of the ZEEMANN interaction suggests that the interaction picture should be used for the formal treatment:

$$\hat{\rho}^*(t) = e^{i\hat{H}_Z}\hat{\rho}(t)e^{-i\hat{H}_Z} \quad (2.15)$$

$$\hat{H}^*(t) = e^{i\hat{H}_Z}\hat{H}'(t)e^{-i\hat{H}_Z} \quad (2.16)$$

$$\dot{\hat{\rho}}^*(t) = -i[\hat{H}^*(t), \hat{\rho}^*(t)] \quad (2.17)$$

with $\hat{H}'(t) = \hat{H}_{RF}(t) + \hat{H}_{int(t)}$. This is equivalent to going from the laboratory frame to a coordinate system rotating with the LARMOR frequency of the spins, the so-called *rotating frame*. This especially simplifies the theoretical treatment of r.f pulses, as will be shown later.

Since $\hat{H}_Z >> \hat{H}_{int}(t)$, perturbation theory can be applied. In first order, this leads to the so-called *secular approximation*, where off-diagonal matrix elements of H may be dropped if their magnitude is small compared to the difference in eigenvalues of $\hat{H}_Z$ [Levitt 01]. Practically, this means that all components of H' that do not commute with $\hat{H}_Z$ can be dropped, since in the rotating frame these components undergo fast oscillations. The secular part of the Hamiltonian in spherical tensor representation reads:

$$\hat{H} = A_{00}\hat{T}_{00} + A_{10}\hat{T}_{10} + A_{20}\hat{T}_{20} \quad (2.18)$$

This is even further simplified by the fact that for all NMR interactions of interest the antisymmetric part of the space part can be neglected, and the symmetric part can be diagonalised in the principal axis system (PAS) of the interaction. Therefore, A_{10} vanishes and one is only left with

$$\hat{H} = A_{00}\hat{T}_{00} + A_{20}\hat{T}_{20} \quad (2.19)$$

Initial State

As mentioned earlier, the initial state of a spin system is given by a BOLTZMANN distribution of the individual spins among the energy levels of the system. Taking only the

contribution of the ZEEMAN energy into account, the initial state density matrix is given by [Abragam 61]:

$$\hat{\rho}_0 = \frac{exp(-\frac{\hbar \hat{H}_Z}{kT})}{\mathsf{Tr}[exp(-\frac{\hbar \hat{H}_Z}{kT})]}. \tag{2.20}$$

As the ZEEMAN interaction is a one particle interaction, ρ_0 is the direct product of the density matrices of the single nuclear spins

$$\hat{\rho}_0^{(i)} = \frac{exp(-\frac{\gamma \hbar B_0 \hat{I}_z}{kT})}{\mathsf{Tr}[exp(-\frac{\gamma \hbar B_0 \hat{I}_z}{kT})]}. \tag{2.21}$$

For temperatures $T > 1K$ and constant energy $E = \mathsf{Tr}[\hat{\rho}\hat{H}]$, the exponential functions can be expanded into a power series which can be truncated after the first order. The equilibrium density matrix is finally obtained as

$$\hat{\rho}_{eq} \sim \hat{\mathbb{1}} + \frac{\gamma \hbar B_0}{kT} \hat{I}_z = \hat{\mathbb{1}} + \frac{\omega_\mathrm{L}}{kT} \hat{I}_z. \tag{2.22}$$

The unity operator, $\hat{\mathbb{1}}$, does not evolve in time, since it commutes with any other operator and can therefore be neglected. Thus, the equilibrium state in a static magnetic field oriented along the z-axis is given by the sum of the individual z-angular momentum operators, with relative weights determined by the LARMOR frequencies. Since only the ZEEMAN interaction was taken into account for calculating the initial state, ρ_0 is invariant under the transformation to the rotating frame.

2.2.2 Chemical Shielding

The actual magnetic field as experienced by a nuclear spin deviates from the external magnetic field due to the diamagnetic shielding by the surrounding electrons. This results in a correction to the ZEEMAN energy which provides information on the electronic structure of the sample. This correction is usually referred to as *chemical shielding* or *chemical shift* (CS). In a classical description, the magnetic field induces currents in the electron clouds, which in turn generate a magnetic field $\underline{B}_\mathrm{ind}$. This induced magnetic field scales, in a good approximation, linearly with the external magnetic field $\underline{B}_\mathrm{ind} = \underline{\underline{\sigma}}\,\underline{B}_0$, where $\underline{\underline{\sigma}}$ is the chemical shielding tensor. The nuclear spin senses an effective magnetic field $\underline{B}_\mathrm{eff} = \underline{B}_0 - \underline{B}_\mathrm{ind} = \underline{B}_0 - \underline{\underline{\sigma}} \cdot \underline{B}_0$, and the chemical shift Hamiltonian is given by

$$\hat{H}_\mathrm{CS} = \gamma \underline{\hat{I}} \cdot \underline{\underline{\sigma}} \cdot \underline{B}_0 \overset{\underline{B}_0 \| \underline{e}_z}{=} \gamma(\hat{I}_x \sigma_{xz} + \hat{I}_y \sigma_{yz} + \hat{I}_z \sigma_{zz}) B_0 \tag{2.23}$$

Only the last term is retained in the secular approximation.
Neglecting the antisymmetric part of the chemical shielding tensor and transforming to its principal axis system (PAS) yields

$$\underline{\underline{\sigma}} = \sigma_{\mathrm{iso}} + \delta_{\mathrm{CS}} \begin{pmatrix} -\frac{1+\eta_{\mathrm{CS}}}{2} & 0 & 0 \\ 0 & -\frac{1-\eta_{\mathrm{CS}}}{2} & 0 \\ 0 & 0 & 1 \end{pmatrix} \tag{2.24}$$

with the anisotropy parameter $\delta_{\mathrm{CS}} = \omega_{\mathrm{L}}(\sigma_{zz}^{\mathrm{PAS}} - \sigma_{\mathrm{iso}})$ and the so-called asymmetry parameter

$$\eta_{\mathrm{CS}} = \frac{\sigma_{yy}^{\mathrm{PAS}} - \sigma_{xx}^{\mathrm{PAS}}}{\sigma_{zz}^{\mathrm{PAS}} - \sigma_{\mathrm{iso}}} \tag{2.25}$$

The chemical shift anisotropy (CSA) depends on the orientation of the PAS with respect to the laboratory frame. Since no CSA measurements were done in this thesis it will not be discussed further.

The isotropic part σ_{iso} is orientation independent and hence does not change with motion or orientation of the molecules or the sample. It leads to a site specific correction of the Larmor frequency for each nucleus in a molecule, which is called the chemical shift δ and commonly given in ppm of the Larmor frequency of the observed nucleus (ν) relative to the Larmor frequency of a suitable reference compound (ν_{ref}):

$$\delta\,[\mathrm{ppm}] = \frac{\nu - \nu_{ref}}{\nu_{ref}} \cdot 10^6. \tag{2.26}$$

The great advantage of the ppm-scale is its independence of the strength of the external magnetic field B_0, which greatly simplifies the comparison between spectra measured at different spectrometers.

The CS interaction is predominantly intramolecular and allows for the spectral resolution of nuclei of the same isotope at different sites in a molecule. However, it has significant intermolecular components, especially in solids: The electrons of benzene rings, for example, can shield nuclear spins even in neighbouring molecules, and for hydrogen-bonded protons the chemical shift is extremely sensitive to the strength of the hydrogen bond. Thus, information on molecular packing effects (such as π-π stacking and hydrogen bonding) can be gained by comparing liquid and solid-state NMR spectra.

2.2.3 Dipole-Dipole Interaction

Since the overlap of the nuclear wave functions is neglible, the through space interaction of two nuclei with nonvanishing spin quantum number is restricted to the magnetic dipole-

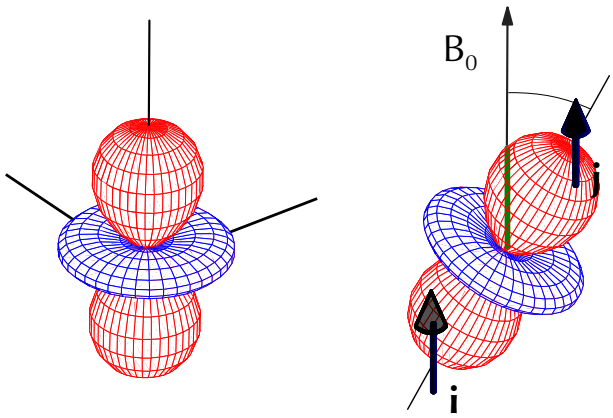

Figure 2.1: *Angular dependence of the dipole-dipole interaction tensor.*

dipole interaction. The Hamiltonian of this interaction for two nuclei with internuclear vector $\underline{r}_{ij}$ can be derived by the correspondence principle:

$$\hat{H}_{\mathrm{D}}^{(ij)} = -\frac{\mu_0 \hbar \gamma_i \gamma_j}{4\pi} \frac{3(\hat{\underline{I}}^{(i)} \cdot \underline{e}_{r_{ij}})(\hat{\underline{I}}^{(j)} \cdot \underline{e}_{r_{ij}}) - \hat{\underline{I}}^{(i)} \cdot \hat{\underline{I}}^{(j)})}{r_{ij}^3}. \tag{2.27}$$

According to Eq. (2.11), the Hamiltonian can be expressed as a bilinear product

$$\hat{H}_{\mathrm{D}}^{(ij)} = \hat{\underline{I}}^{(i)} \cdot \underline{\underline{D}}^{(ij)} \cdot \hat{\underline{I}}^{(j)} \tag{2.28}$$

with the dipolar coupling tensor $\underline{\underline{D}}^{(ij)}$, which after neglecting the antisymmetric part and transforming to the principal axis system (PAS) is obtained as

$$\underline{\underline{D}}^{(ij)} = -2D^{(ij)} \begin{pmatrix} -\frac{1}{2} & 0 & 0 \\ 0 & -\frac{1}{2} & 0 \\ 0 & 0 & 1 \end{pmatrix} \tag{2.29}$$

with the dipole-dipole coupling constant

$$D^{(ij)} = \frac{\mu_0 \hbar \gamma_i \gamma_j}{4\pi r_{ij}^3} \tag{2.30}$$

Since $\underline{\underline{D}}^{(ij)}$ is traceless, the isotropic component A_{00} vanishes when transforming to the spherical tensor representation. Applying the secular approximation, we are only left with the term $A_{20}\hat{T}_{20}$ (see Eq. (2.19)). After a rotational transformation of A_{20} from the principal axis frame to the laboratory frame, the Hamiltonian of the dipole-dipole interaction reads as

$$\hat{H}_{\mathrm{D}}^{(ij)} = D^{(ij)} \frac{1}{2}(3\cos^2(\theta) - 1)(3\hat{I}_z^{(i)}\hat{I}_z^{(i)} - \hat{\underline{I}}^{(i)} \cdot \hat{\underline{I}}^{(j)}) \tag{2.31}$$

$$= D^{(ij)} \frac{1}{2}(3\cos^2(\theta) - 1)(2\hat{I}_z^{(i)}\hat{I}_z^{(i)} - (\hat{I}_+^{(i)}\hat{I}_-^{(j)} + \hat{I}_+^{(j)}\hat{I}_-^{(i)})) \tag{2.32}$$

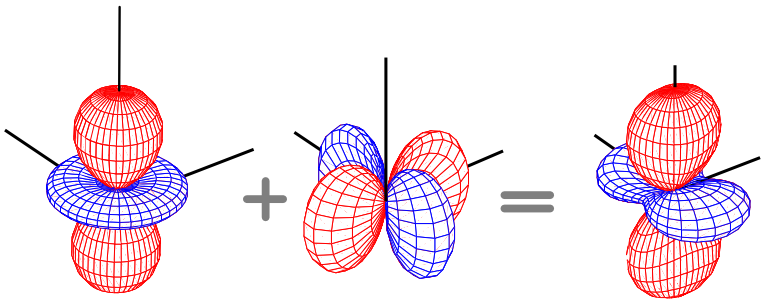

Figure 2.2: *Angular dependence of the quadrupolar coupling tensor for* $\eta = 0.4$.

with θ denoting the angle between the magnetic field $\underline{B}_0$ and the internuclear vector (see Fig. 2.1). The term $\hat{I}_+^{(i)}\hat{I}_-^{(j)} + \hat{I}_+^{(j)}\hat{I}_-^{(i)}$ is the flip-flop term describing polarisation exchange of two spins under conservation of energy. It becomes non-secular as the difference of the ZEEMAN energy levels of the two interacting nuclei increases and can therefore usually be neglected for heteronuclear dipole-dipole couplings. To discriminate the two different spins, one usually writes $\hat{\underline{I}}^{(i)} = \hat{\underline{I}}$ and $\hat{\underline{I}}^{(j)} = \hat{\underline{S}}$ for heteronuclear spin systems:

$$\hat{H}_{\mathrm{D,het}}^{(ij)} = D^{(ij)}(3\cos^2(\theta) - 1)(\hat{I}_z\hat{S}_z). \tag{2.33}$$

For homonuclear spin systems, the ZEEMANN energy levels are near-degenerate and the flip-flop term cannot be neglected

$$\hat{H}_{\mathrm{D,hom}}^{(ij)} = D^{(ij)}\frac{1}{2}(3\cos^2(\theta) - 1)(3\hat{I}_z^{(i)}\hat{I}_z^{(i)} - \hat{\underline{I}}^{(i)} \cdot \hat{\underline{I}}^{(j)}). \tag{2.34}$$

The dipole-dipole coupling tensor is symmetric (which can be seen from the fact that two of its components in the PAS are equal), and the coupling therefore only depends on the polar angle θ. The angular dependence of the tensor (shown in Fig. 2.1) is given by the second Legendre polynomial that vanishes for $\theta = 54.7°$, i.e. at the so-called *magic angle*.

Dipole-dipole coupling constants are routinely exploited as a source of structural information. Due to the r_{ij}^{-3} dependence (see Eq. (2.30)) the distance of nuclei can be determined and moreover the sensitivity of the coupling on the orientation of the internuclear vector can be used to investigate oriented samples as well as anisotropic molecular motions.

2.2.4 Quadrupole Interaction

Nuclei with spin $I > \frac{1}{2}$ carry an electric quadrupole moment eQ, that interacts with the electric field gradient (EFG) tensor $\underline{\underline{V}}$ generated by the surrounding electrons and nuclei:

$$V_{\alpha\beta} = \frac{\partial^2 \Phi}{\partial\alpha\partial\beta}; \qquad \alpha, \beta \in \{x, y, z\} \tag{2.35}$$

The secular part of the Hamiltonian of the quadrupole interaction is [Slichter 96]:

$$\hat{H}_{\mathrm{Q}} = \frac{eQ}{2I(2I-1)\hbar} \hat{I} \underline{\underline{V}} \hat{I} \tag{2.36}$$

Defining the quadrupole interaction tensor as

$$\underline{\underline{Q}} = \frac{eQ}{2I(2I-1)\hbar} \underline{\underline{V}} \tag{2.37}$$

yields

$$\hat{H}_{\mathrm{Q}} = \underline{\hat{I}} \cdot \underline{\underline{Q}} \cdot \underline{\hat{I}}. \tag{2.38}$$

In its principal axis system, the symmetric part of $\underline{\underline{Q}}$ takes the form:

$$\underline{\underline{Q}} = \delta_{\mathrm{Q}} \begin{pmatrix} -\frac{1+\eta}{2} & 0 & 0 \\ 0 & -\frac{1-\eta}{2} & 0 \\ 0 & 0 & 1 \end{pmatrix} \tag{2.39}$$

with the asymmetry parameter

$$\eta = \frac{V_{xx}^{\mathrm{PAS}} - V_{yy}^{\mathrm{PAS}}}{V_{zz}^{\mathrm{PAS}}} \tag{2.40}$$

and the anisotropy

$$\delta = \frac{3}{2} \frac{V_{zz}^{\mathrm{PAS}} eQ}{2I(2I-1)\hbar} = \frac{3}{2} \frac{e^2 qQ}{2I(2I-1)\hbar} \tag{2.41}$$

Due to the Laplace equation, the trace of the EFG tensor $\underline{\underline{V}}$ vanishes and, in analogy to the dipole-dipole interaction, we are only left with the term $A_{20}\hat{T}_{20}$ (see Eq. (2.19)). Rotational transformation of A_{20} from the PAS to the laboratory frame yields

$$\hat{H}_{\mathrm{Q}} = \frac{\delta}{2}(3\cos^2(\theta) - 1 + \eta \sin^2(\theta) cos(2\phi)(3\hat{I}_z\hat{I}_z - \underline{\hat{I}}\hat{I}). \tag{2.42}$$

In contrast to the dipole-dipole interaction tensor, the quadrupole interaction is usually not symmetric and therefore depends on the polar angle θ as well as on the azimuthal angle ϕ. The angular dependence for $\eta = 0.4$ is shown in Fig. 2.2.

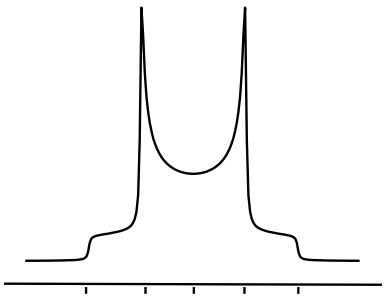

Figure 2.3: *Static* Pake*-pattern for a symmetric* ^2H *quadrupolar coupling.*

In symmetry considerations, care has to be taken not to mix up the symmetry of the tensor with the symmetry of the matrix representing the tensor. Since the antisymmetric part has been neglected, the matrix representing the quadrupole coupling tensor is clearly symmetric (even diagonal). Still the tensor itself is asymmetric, meaning it has no rotational symmetry along all of its principal axes. This can be seen from the fact that all three eigenvalues of the matrix are different. A tensor having two matching eigenvalues (e.g., the dipole-dipole coupling tensor) is symmetric but anisotropic, a tensor with three matching eigenvalues is isotropic (but naturally cannot be traceless). An example for a purely isotropic interaction tensor is the Zeeman interaction.

The quadrupole interaction senses the electronic environment of the nucleus and is therefore of great help when it comes to comparison with electronic structure calculations. In powdered samples, the superposition of lines corresponding to different orientations of the molecules leads to broad lines with characteristic lineshapes. In the case of spin-1 nuclei, such as ^{2}H , these lines are called Pake-patterns (see Fig. 2.3). The orientation dependence of the ^{2}H quadrupole coupling is routinely used in NMR experiments to investigate oriented samples and anisotropic motions of molecules [Macho 01]. For these experiments the asymmetry of the quadrupole interaction is advantageous in that it leads to a dependence of the coupling on two Euler angles. For most quadrupolar nuclei the quadrupole coupling is in the range of MHz and, thus too large to be treated within the secular approximation. In this work, however, only quadrupolar nuclei with rather small quadrupole moments, such as ^{2}H and ^{7}Li , were investigated that exhibit quadrupole couplings in the range of 100 kHz.

2.2.5 The Effect of Radio Frequency Pulses

In a standard NMR experiment, the sample is surrounded by a coil that produces a small horizontal (i.e. $\perp B_0$) oscillating magnetic field $\underline{B}_1 \sim \cos(\omega_{\mathrm{RF}})$. If this field oscillates at the LARMOR frequency of the spins, it will introduce transitions between the ZEEMAN levels. This can be illustrated by decomposing a magnetic field oscillating in x-direction $\underline{B}_1 = B_1 \cos(\omega_{\mathrm{RF}} t)\underline{e}_x$ into a sum of two counter-rotating magnetic fields (see Fig.2.4a)

$$\underline{B}_1 = \left[\frac{B_1}{2}\cos(\omega_{\mathrm{RF}}t)\underline{e}_x + \frac{A}{2}\sin(\omega_{\mathrm{RF}}t)\underline{e}_y\right] + \left[\frac{B_1}{2}\cos(\omega_{\mathrm{RF}}t)\underline{e}_x - \frac{A}{2}\sin(\omega_{\mathrm{RF}}t)\underline{e}_y\right] \quad (2.43)$$

in the x-y-plane.

For nuclei with $\gamma > 0$ the first component rotates in the same sense as the spin precession and is therefore resonant for $\omega_{\mathrm{RF}} = \omega_{\mathrm{L}}$. Thus, in the rotating frame this component is static. The second component rotates in the opposite sense of the Larmor frequency, and in the rotating frame, with twice the LARMOR frequency (see Fig.2.4b). This component has generally almost no influence on the spins and can therefore be neglected. The Hamiltonian of the r.f. pulse is then

$$\hat{H}_{\mathrm{RF}} = \frac{1}{2}\gamma B_1 \cos(\omega_{\mathrm{RF}}t)\hat{I}_x + \frac{A}{2}\sin(\omega_{\mathrm{RF}}t)\hat{I}_y \quad (2.44)$$

$$= \frac{1}{2}\gamma B_1 e^{-i\omega_{\mathrm{RF}}t\hat{I}_z}\hat{I}_x e^{i\omega_{\mathrm{RF}}t\hat{I}_z} \quad (2.45)$$

Transformation to the rotating frame yields

$$\hat{H} = \frac{1}{2}\gamma B_1 \hat{I}_x \quad (2.46)$$

which equals the Hamiltonian of a static magnetic field with field strength $\frac{1}{2}B_1$, as already discussed above. When such a field is applied, the net magnetisation will start precessing around the $\underline{e}_x$ direction with the frequency $\omega_{\mathrm{RF}} = \frac{1}{2}\gamma B_1$ (see Fig.2.4c). During a pulse of duration t, the net magnetisation will rotate by an angle $\alpha = \omega_{\mathrm{RF}}t$, the so-called flip-angle. The propagator of such a pulse reads as

$$\hat{U} = e^{\hat{H}_{\mathrm{RF}}} = e^{-i\omega_{\mathrm{RF}}t\hat{I}_x} = e^{-i\alpha\hat{I}_x} \quad (2.47)$$

If the pulse duration and field strength are chosen such that $\alpha = 90°$, a state with pure transverse magnetisation can be prepared. Generally the flip angle α can be adjusted by either changing the duration or the power level of the pulse. Since in multi-pulse sequences the pulse length can influence the result of an experiment, pulses are in practice usually

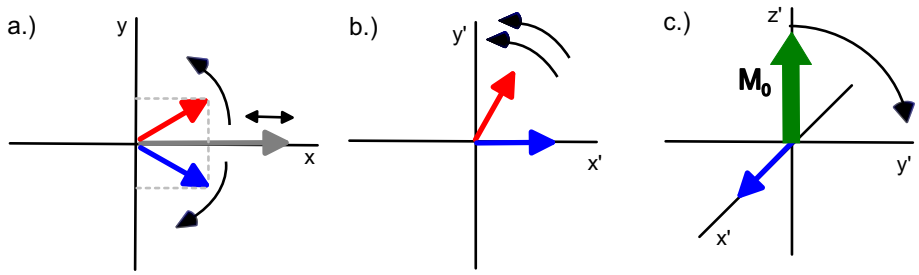

Figure 2.4: *Decomposition of an oscillating magentic field in x-direction into two counter-rotating magnetic fields (a), the two components in the rotating frame (b), and the effect of the static component on the net magnetisation in the rotating frame (c).*

set by adjusting the pulse power level while choosing the length according to experimental needs.

A very popular notation of the effect of r.f. pulses is the so-called *product operator formalism*, which was introduced by Ernst and co-workers [Sørensen 83]. The effect of a radio frequency pulse is simply denoted by

$$\hat{I}_z \xrightarrow{\alpha \hat{I}_y} \hat{I}_z \cos(\alpha) + \hat{I}_x \sin(\alpha) \tag{2.48}$$

The effects of the most common rotations on the three spin operators are listed in Table 2.1. This formalism is not restricted to the description of the effect of RF-pulses. Rather, the time evolution under most NMR interactions can conveniently be described provided that the corresponding Hamiltonian is time independent or time averaged.

Table 2.1: *The effect of* $e^{-i\alpha\hat{I}_l}\hat{I}_k e^{-i\alpha\hat{I}_l}$ *for* $k, l \in \{x, y, z\}$

	$\hat{I}_x$	$\hat{I}_y$	$\hat{I}_z$
$e^{-i\alpha\hat{I}_x}$	$\hat{I}_x$	$\hat{I}_y \cos(\alpha) + \hat{I}_z \sin(\alpha)$	$\hat{I}_z \cos(\alpha) - \hat{I}_y \sin(\alpha)$
$e^{-i\alpha\hat{I}_y}$	$\hat{I}_x \cos(\alpha) - \hat{I}_z \sin(\alpha)$	$\hat{I}_z$	$\hat{I}_y \cos(\alpha) + \hat{I}_x \sin(\alpha)$
$e^{-i\alpha\hat{I}_z}$	$\hat{I}_x \cos(\alpha) + \hat{I}_y \sin(\alpha)$	$\hat{I}_y \cos(\alpha) - \hat{I}_x \sin(\alpha)$	$\hat{I}_z$

2.3 Magic Angle Spinning (MAS)

In powdered solids, the presence of anisotropic interactions leads to broad lines, as the different molecular orientations give rise to different resonance frequencies. If the anisotropy of the coupling exceeds the chemical shift the lines will overlap and the chemical shift resolution is lost. In addition to this, dipolar couplings among and to abundant nuclei (e.g. protons) broaden the lines. In proton spectra, homonuclear dipole-dipole couplings broaden the lines dramatically and lead to spectra that basically consist of one large 'hump'. In liquids, the fast isotropic tumbling of the molecules averages the anisotropic interactions to zero and no such substantial line broadening is observed. It would therefore be desirable to mimic this motion to get spectral resolution in solid samples as well.

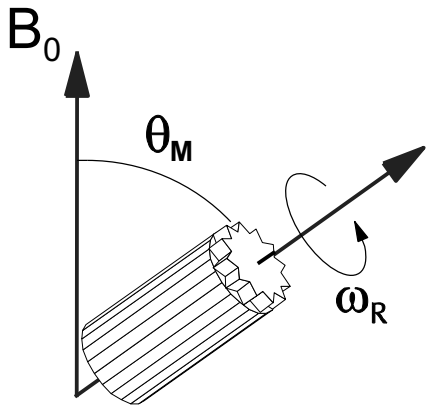

Figure 2.5: *MAS rotor spinning with frequency ω_R at angle Θ_M.*

In the 1950s Andrew [Andrew 58] and Lowe [Lowe 59] introduced a technique where the sample is rapidly spun about an axis tilted with respect to the static magnetic field $\underline{B}_0$ by an angle $\theta_{\mathrm{M}} = 54.7°$ as shown in Fig. 2.5. No matter which orientation the interaction tensor has, the averaged interaction tensor clearly has rotational symmetry about the spinning axis (see Fig. 2.6) and its angular dependence is given by the second Legendre polynomial $P(\theta_{\mathrm{M}}) = \frac{1}{2}(3\cos^2(\theta_{\mathrm{M}}) - 1)$. The angle θ_{M} is now defined by the rotor axis and can therefore be chosen freely. Since the second Legendre polynomial vanishes for $\theta_{\mathrm{M}} = 54.7°$ (the so-called *magic angle*), anisotropic interactions can be averaged out by setting the angle of the rotor axis accordingly.

However, to completely average an interaction, the spinning has, in general, to be rapid enough. Since the interactions of interest can reach up to a few hundred kHz, this is mechanically quite demanding. Today rotors with diameter 2.5 mm capable of spinning up to 35 kHz are commercially available. In the literature up to 70 kHz spinning speed is reported [Samoson 04].

Nevertheless, even at lower spinning speeds, resolved spectra can be obtained. According to Maricq and Waugh [Maricq 79] line broadening effects can be divided into homogeneous and inhomogeneous line broadening. Inhomogeneous line broadening is caused by the

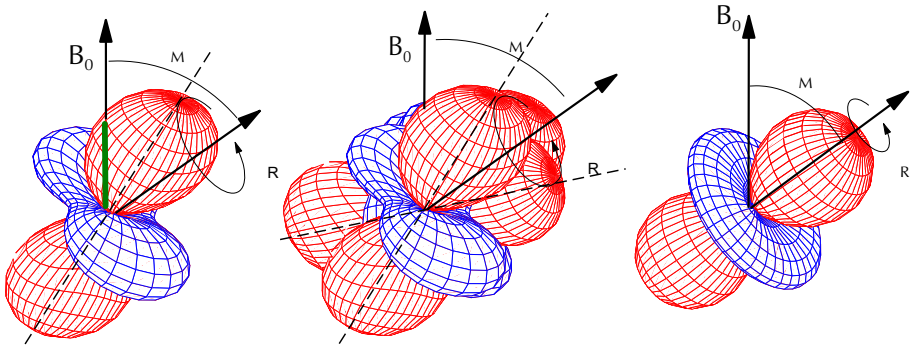

Figure 2.6: *Illustration of the averaging of a second-rank tensor under magic-angle spinning.*

orientation dependence of the anisotropic interactions, and is simply a superposition of resonance lines originating from different orientations of the molecules. This is the case for CSA, first order quadrupolar couplings and dipole-dipole couplings of isolated spin pairs. As shown later in this section, these interactions are averaged over one rotor period and the initial signal is fully refocused. As a consequence of this, the spectrum splits into a sum of narrow sidebands under MAS. Homogeneous line broadening arises from dipole-dipole couplings between multiple spins. It occurs in particular for protons, as they have high natural abundance and a high gyromagnetic ratio. In those systems the flip-flop term mixes the near-degenerate ZEEMAN levels, leading to a continual exchange of longitudinal magnetisation between the spins that prevents the complete refocussing of the signal after one rotor period and, in this way, reduces the echo amplitude . Thus, the lines no longer split into a pattern of narrow lines, but are rather narrowed in a gradual manner with increasing spinning speed. To obtain sharp lines the spinning has to be faster than the exchange rate ($\omega_{\mathrm{R}} >> \omega_{\mathrm{D}}$). Since the homonuclear dipole-dipole coupling among protons can reach up to 30 kHz in solids, resolution in proton spectra usually suffers from homogeneous line broadening even under fast MAS.

2.3.1 Average Hamiltonian Theory (AHT)

Under MAS, the Hamiltonian becomes explicitly time dependent and the calculation of the propagator $\hat{U}$ is no longer straightforward. Still, the Hamiltonian is periodic with the cycle time τ_{R}. For cyclic systems it is convenient to calculate an averaged (time independent) Hamiltonian $\hat{\bar{H}}$ for one rotor period, such that

$$\hat{H}(\tau_{\mathrm{R}}) = e^{-i\hat{\bar{H}}\tau_{\mathrm{R}}} \tag{2.49}$$

The Hamiltonian for N rotor periods can then be written as

$$\hat{H}(N\tau_{\mathrm{R}}) = e^{-i\hat{\bar{H}}N\tau_{\mathrm{R}}} \tag{2.50}$$

The problem is now reduced to calculating the averaged Hamiltonian for one rotor period. This is done, first, by assuming the Hamiltonian to be stepwise time independent for N time intervals, where, without loss of generality, the time steps are assumed to be equidistant $\Delta t = \frac{\tau_{\mathrm{R}}}{N}$:

$$\hat{H}(t) = \hat{H}_n \text{ for } (n-1)\Delta t < t < n\Delta t \tag{2.51}$$

and later performing the limit $\Delta t \to 0$ ($n \to \infty$) to get back to a continuous time dependence. This is possible since the Hamiltonian is a continuous function of time on $[0, \tau_{\mathrm{R}}]$ and can therefore always be assumed to be constant on infinite small time intervals ($\lim_{\Delta t\to 0}[\hat{H}(t), \hat{H}(t+\Delta t)] = 0$). Formally this means expressing the integral in Eq. (2.7) as the limit of a sum:

$$\hat{T}e^{-i\int_0^t dt'\hat{H}(t')} = \hat{T}\lim_{\Delta t\to 0}\prod_{n=0}^{N} e^{-i\hat{H}_n\Delta t} \tag{2.52}$$

Starting with N discrete time steps, time ordering means placing the earliest operator on the right hand side and the propagator for one rotor period is given by

$$\hat{U}(\tau_{\mathrm{R}}) = e^{-i\hat{H}_N\Delta t}\ldots e^{-i\hat{H}_2\Delta t}e^{-i\hat{H}_1\Delta t} \stackrel{!}{=} e^{-i\hat{\bar{H}}\tau_{\mathrm{R}}} \tag{2.53}$$

Unfortunately, $\hat{\bar{H}}$ cannot be written as a simple sum of the $\hat{H}_i$, since generally $[\hat{H}_i, \hat{H}_j] \neq 0$. However, according to the Baker-Campbell-Hausdorff relation

$$e^{\hat{B}}e^{\hat{A}} = exp\left\{\hat{B} + \hat{A} + \frac{1}{2}[\hat{A}, \hat{B}] + \frac{1}{12}([\hat{B}, [\hat{B}, \hat{A}]] + [[\hat{B}, \hat{A}], \hat{A}]) + \ldots\right\} \tag{2.54}$$

the product can be expanded and is then most clearly written as a sum of different orders

$$\hat{\bar{H}} = \hat{\bar{H}}^{(0)} + \hat{\bar{H}}^{(1)} + \hat{\bar{H}}^{(2)} + \ldots, \tag{2.55}$$

where the order i indicates the overall power of Δt, and the number of nested commutators involved. The first three terms read as

$$\hat{\bar{H}}^{(0)} = \frac{1}{\tau_{\mathrm{R}}}\sum_{i=1}^{N}\hat{H}_i\Delta t \tag{2.56}$$

$$\hat{\bar{H}}^{(1)} = -\frac{1}{2\tau_{\mathrm{R}}}\sum_{i=1}^{N}\sum_{j=1}^{i-1}[\hat{H}_i\Delta t, \hat{H}_j\Delta t] \tag{2.57}$$

$$\hat{\bar{H}}^{(2)} = -\frac{1}{2\tau_{\mathrm{R}}}\sum_{i=1}^{N}\sum_{j=1}^{i-1}\sum_{k=1}^{j-1}([\hat{H}_i\Delta t, [\hat{H}_j\Delta t, \hat{H}_k\Delta t]] + [\hat{H}_k\Delta t, [\hat{H}_j\Delta t, \hat{H}_i\Delta t]]) \tag{2.58}$$

We can now perform the limit $\Delta t \to 0$ for the Hamiltonians of each order separately, going back from sums to integrals. This is known as the MAGNUS expansion:

$$\hat{\bar{H}}^{(0)} = \frac{1}{\tau_{\mathrm{R}}} \int_0^{\tau_{\mathrm{R}}} \mathrm{d}t\, \hat{H}(t), \tag{2.59}$$

$$\hat{\bar{H}}^{(1)} = -\frac{i}{2\tau_{\mathrm{R}}} \int_0^{\tau_{\mathrm{R}}} \mathrm{d}t \int_0^{t} \mathrm{d}t' [\hat{H}(t), \hat{H}(t')], \tag{2.60}$$

$$\hat{\bar{H}}^{(2)} = -\frac{1}{6\tau_{\mathrm{R}}} \int_0^{\tau_{\mathrm{R}}} \mathrm{d}t \int_0^{t} \mathrm{d}t' \int_0^{t'} \mathrm{d}t'' \Big([\hat{H}(t), [\hat{H}(t'), \hat{H}(t'')]] + [\hat{H}(t''), [\hat{H}(t'), \hat{H}(t)]] \Big). \tag{2.61}$$

For inhomogeneous interactions, the commutator $[\hat{H}(t), \hat{H}(t')]$ vanishes [Maricq 79]. Correspondingly, for CSA, first order quadrupolar couplings and dipole-dipole couplings of isolated spin pairs, the higher-order terms in the MAGNUS expansion vanish for those interactions, and one is left with the zeroth-order average Hamiltonian

$$\hat{\bar{H}}_{\lambda}^{(0)} = \frac{1}{t} \int_0^{t} \hat{H}_{\lambda}(t) dt = \hat{T}_{00} A_{00}^{LAB} + \hat{T}_{20} \frac{1}{t} \int_0^{t} A_{20}^{LAB}(\omega_R t) dt \tag{2.62}$$

which describes the evolution under an interaction λ and sample rotation for arbitrary times.

2.3.2 Hamiltonians under MAS

The explicit calculation of the average Hamiltonian according to Eq. (2.62) requires the knowledge of the space part A_{20}^{LAB} in the laboratory frame. Since the interaction tensors were defined in their principal axis systems (PAS), it is necessary to transform them into the laboratory frame (LAB). This generally involves three subsequent rotations about Euler angles, first from the PAS to the molecular frame (MF), second from the molecular frame to the rotor frame (R) and finally from the rotor frame to the laboratory frame:

$$\text{PAS} \xrightarrow[\textit{tensor orientation}]{(\alpha_{\mathrm{PC}},\beta_{\mathrm{PC}},\gamma_{\mathrm{PC}})} \text{MF} \xrightarrow[\textit{powder average}]{(\alpha_{\mathrm{MF}},\beta_{\mathrm{MF}},\gamma_{\mathrm{MF}})} \text{Rotor} \xrightarrow[\textit{MAS}]{(\omega_{\mathrm{R}}t,\beta_{\mathrm{M}},0)} \text{LAB}$$

If only one interaction is considered the MF can be set to be the PAS of the interaction and one is only left with two rotations:

$$\text{PAS/MF} \xrightarrow[\textit{powder average}]{\Omega=(\alpha,\beta,\gamma)} \text{Rotor} \xrightarrow[\textit{MAS}]{\Omega_M=(\omega_R t,\beta_M,0)} \text{LAB},$$

where α, β and γ describe the orientation of the molecule with respect to the rotor frame. For these angles a proper powder average according to the orientation of the molecules in the sample has to be performed. The time dependence of MAS enters in the second step where the first Euler angle of the rotor frame with respect to the laboratory frame is given by $\omega_{\mathrm{R}}t$. For actually performing these rotations, the advantage of introducing spherical tensors becomes obvious:

$$A_{20}^{\lambda,LAB}(t) = \sum_{m=-2}^{2} A_{2-m}^{\lambda,R}\, e^{im\omega_R t}\, D_{-m0}^{(2)}(\Omega_M) \tag{2.63}$$

$$= \sum_{m=-2}^{2} A_{2-m}^{\lambda,R}\, e^{im\omega_R t}\, d_{-m0}^{(2)}(\beta_M) \tag{2.64}$$

$$= \sum_{m=-2}^{2} \left[\sum_{m'=-2}^{2} A_{2-m'}^{\lambda,PAS}\, \mathcal{D}_{-m'-m}^{(2)}(\Omega) \right] e^{im\omega_R t}\, d_{-m0}^{(2)}(\beta_M) \tag{2.65}$$

When spinning at the magic angle ($\beta_M = 54.7^\circ$) the reduced Wigner rotation matrix $d_{00}^{(2)} = 0$ vanishes and one is only left with rotor modulated terms. Inserting this expression in Eq. (2.62) and integration yields

$$\hat{\bar{H}}_{\lambda,MAS} = \hat{T}_{00} A_{00}^{\lambda,LAB} + \hat{T}_{20} \frac{1}{t} \int_0^t A_{20}^{LAB}(\omega_R t) dt = \hat{T}_{00} A_{00}^{\lambda,LAB} + \hat{T}_{20} \cdot \frac{1}{t} \cdot \sqrt{\frac{3}{2}} \cdot \Phi_\lambda \tag{2.66}$$

The first term is zero for purely anisotropic interactions, such as the dipole-dipole interaction and first order quadrupolar interactions, since $A_{00}^{quad,LAB} = A_{00}^{dip,LAB} = 0$. The

integrated phase Φ_λ is given by

$$\begin{aligned}\Phi_\lambda(t) &= \frac{C_1}{\omega_R}\left\{\sin(\gamma+\omega_R t)-\sin\gamma\right\}+\frac{C_2}{2\omega_R}\left\{\sin(2\gamma+2\omega_R t)-\sin 2\gamma\right\} \qquad (2.67)\\ &\quad -\frac{S_1}{\omega_R}\left\{\cos(\gamma+\omega_R t)-\cos\gamma\right\}-\frac{S_2}{2\omega_R}\left\{\cos(2\gamma+2\omega_R t)-\cos 2\gamma\right\},\end{aligned}$$

and

$$C_1 = -\frac{\delta_\lambda}{\sqrt{2}}\sin 2\beta(1+\frac{\eta_\lambda}{3}\cos 2\alpha), \qquad (2.68)$$

$$C_2 = \frac{\delta_\lambda}{2}\sin^2\beta-\frac{\delta_\lambda\eta_\lambda}{6}(1+\cos^2\beta)\cos 2\alpha, \qquad (2.69)$$

$$S_1 = \frac{\sqrt{2}\delta_\lambda\eta_\lambda}{3}\sin\beta\sin 2\alpha, \qquad (2.70)$$

$$S_2 = \frac{\delta_\lambda\eta_\lambda}{3}\cos\beta\sin 2\alpha. \qquad (2.71)$$

For the dipole-dipole interaction, these expressions are further simplified by the fact that $\eta = 0$ and, thus, the integrated phase does not depend on the azimuthal angle α.

When pulse sequence Hamiltonians are to be calculated, the lower limit for the integration in Eq. (2.66), i.e. the initial rotor phase, often needs to be different from zero. For an arbitrary initial rotor phase (i.e., arbitrary lower limit of the integration in Eq. (2.66)) the acquired MAS phase for an interaction λ is obtained as

$$\Phi_\lambda\,|_{t_1}^{t_2} = \Phi_\lambda(t_2)-\Phi_\lambda(t_1) \qquad (2.72)$$

With the expression for the averaged Hamiltonian under MAS (Eq. (2.66)) the evolution of a transverse state $\hat{\rho}(0)=\hat{I}_x$ under an interaction under MAS is given by

$$\hat{I}_x \xrightarrow{\bar{H}_{\lambda,MAS}(t)\,t} \hat{I}_x\cos\Omega_\Lambda + \hat{W}\sin\Omega_\Lambda, \text{ where} \qquad (2.73)$$

$$\begin{aligned}\Omega_{CS} &= \omega_{iso}t+\Phi_{CS},\ \ \hat{W}=\hat{I}_y,\\ \Omega_Q &= \sqrt{\frac{3}{2}}\Phi_Q,\ \ \hat{W}=i(\hat{T}_{21}+\hat{T}_{2-1}),\\ \Omega_{D_{ij}} &= \sqrt{\frac{3}{2}}\Phi_{D,hom},\ \ \hat{I}_x=\hat{I}_x^{(i)}+\hat{I}_x^{(j)},\ \ \hat{W}=2\hat{I}_y^{(i)}\hat{I}_z^{(j)}+2\hat{I}_y^{(j)}\hat{I}_z^{(i)},\\ \Omega_{D_{is}} &= \frac{1}{2}\Phi_{D,het},\ \ \hat{W}=2\hat{I}_y\hat{S}_z.\end{aligned}$$

2.3.3 Rotor Synchronised Acquisition and Spinning sidebands

From Eq. (2.72) it can bee seen that, for inhomogeneous interactions, the integrated phase vanishes after a full rotor period: $\Phi_\lambda\,|_0^{\tau_R} = 0$. This is due to the fact that the Hamiltonian

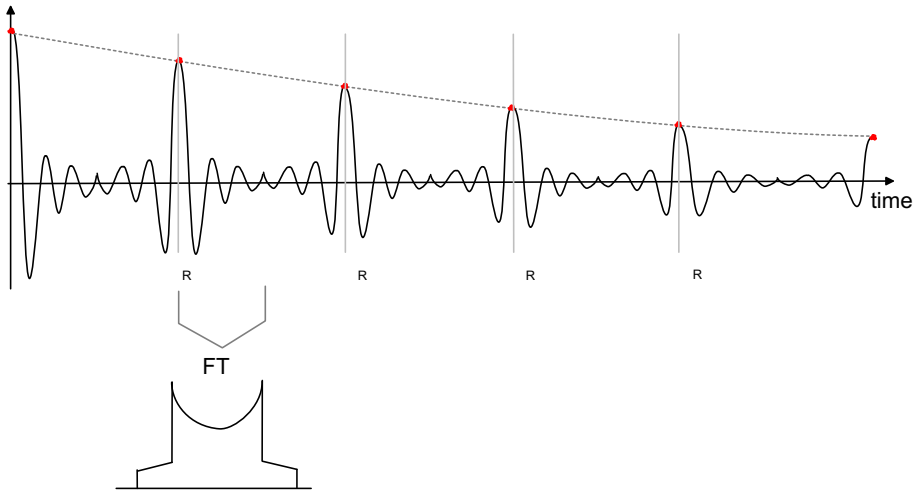

Figure 2.7: *Time domain signal under MAS.*

only contains rotor modulated parts. As a consequence of this, the initial signal is fully refocused after each rotor period (besides additional relaxation effects) and the signal is a series of rotational echoes (see Fig. 2.7). For faster MAS, resp. weaker interactions, the echoes flatten since the signal is refocused already at the beginning of the evolution and, for $\omega_R >> \omega_\lambda$, the interaction is completely averaged and the echoes vanish.

If data points are only acquired at the echo maxima (i.e., rotor-synchronised acquisition) the resulting spectrum consists of a single line that is only broadened by additional relaxation effects. In this way, the effects of purely anisotropic interactions are totally removed from the spectrum. For moderate spinning speeds, the Fourier transform of the first half of each rotor period resembles the principal features of a static spectrum, containing the full information of the interaction since the averaging effect of MAS has not yet set in. Acquisition of data points over several rotor periods spaced by less than one rotor period leads to spinning sidebands in the spectrum. From the intensities of the sidebands the information on the anisotropic interactions can be inferred, provided that the spinning is slow enough to let the interaction take effect before being refocused. For fast MAS the signal intensity is mainly contained in the centre band and the number of sidebands is too small to extract informations. In general, however, MAS has to be fast enough to remove homogeneous line broadening that is usually present in samples due to homonuclear dipole-dipole couplings.

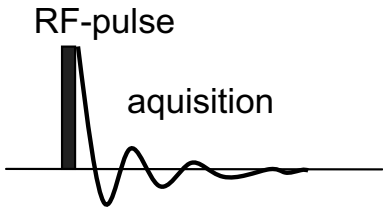

Figure 2.8: *The one-pulse experiment.*

2.4 Basic NMR Experiments

In the following section some basic experiments used in solid state NMR will be described. As conventional in NMR, the pulse sequences are depicted in diagrams with time plotted on the abscissa and the power of the RF pulse as well as an illustration of the signal (with different scaling) plotted on the ordinate. For clarity, 90° pulses are filled black and 180° pulses are filled grey.

2.4.1 The One-Pulse Experiment

The most simple experiment that can be performed in FT NMR consists of a single 90° pulse (see Fig. 2.8).

Starting from thermal equilibrium, after applying a 90°_x pulse (i.e., a 90° pulse with $\underline{B}_1$ parallel to the x-axis) the net magnetisation is flipped to the y-axis and precesses in the x-y-plane with its resonance frequency. This induces an oscillating voltage in the coil, which is amplified and later converted into a digital signal that can be handled by a computer. As ADCs are usually not fast enough and one is anyhow only interested in the response in the rotating frame, the signal is mixed with a reference frequency (Larmor frequency) before being digitised. To obtain the sign of the rotation it is necessary to also record the phase of the induced signal. In modern NMR spectrometers this is done by mixing the signal with two reference signals having the same frequency but a phase shift of 90° (so-called quadrature detection). The data points are then collected in complex form.

The transverse magnetisation originates from a coherent Larmor precession of the spins, a so-called *single-quantum coherence*. This coherence, and with it the detected signal, decays with relaxation time T_2, due to slight differences in the resonance frequencies of

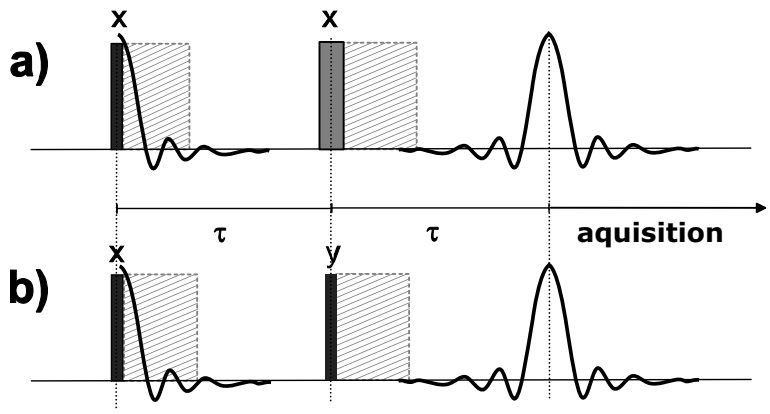

Figure 2.9: *Hahn spin echo (a) and solid echo (b) pulse sequence. Shaded periods indicate the "dead time" after application of a r.f. pulse.*

the spins. The acquired signal decaying with the transverse relaxation constant T_2 is called *free induction decay* (FID).

The system will relax to the thermal equilibrium state of longitudinal magnetisation with the relaxation time constant T_1. This constant determines the time after which the next scan of an experiment can be performed. T_1 and can be up to several seconds and even minutes in solids, while the transverse relaxation is usually much faster.

To compensate receiver offsets and inhomogeneities, the phase of the pulse and the receiver are usually cycled in four steps of 90° each.

2.4.2 Echo Experiments

Broad lines, like those arising from strong quadrupolar couplings, dipole-dipole couplings and chemical shift anisotropy in static spectra have rapidly decaying FIDs. At the same time the power of strong r.f. pulses is orders of magnitude higher than the weak induced signal of the FID. Thus 'ringing' of the coil after a pulse has been applied, prevents measurement of the signal a short time after the pulse, the so-called *dead time*. This means a significant part of a short FID cannot be recorded, leading to severe phase distortions and loss of signal.

This problem can be overcome by echo pulse sequences, where after an initial 90° pulse the spins evolve for a time τ at which a suitable echo pulse is applied that refocuses the FID after a time 2τ. Formally, this is achieved by an inversion of the sign of the

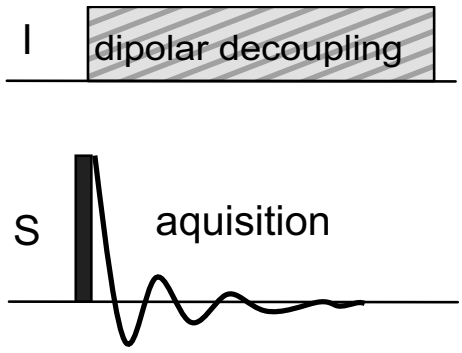

Figure 2.10: *Heteronuclear dipolar decoupling during acquisition.*

Hamiltonian after a time τ, in which way the initial state is recovered after a time 2τ and an echo is formed, provided that the system has not changed during that time.

For interactions linear in $\hat{I}_z$ (chemical shift, resonance offset and heteronuclear dipole-dipole coupling) a 180° pulse generates an echo. This pulse sequence (see Fig.2.9) is known as Hahn spin echo [Hahn 50].

Interactions bilinear in the observed spin's operator (like the quadrupole interaction and the homonuclear dipole-dipole interaction) are refocused by a 90° echo pulse, which is phase shifted by 90° from the initial pulse [Schmidt-Rohr 94]. This sequence, referred to as the solid echo, is depicted in Fig.2.9b. In deuteron NMR molecular reorientation during the solid echo sequence cause frequency changes and lead to characteristic line shapes from which information on the geometry and correlation time of the motion can be extracted [Macho 01].

2.4.3 Heteronuclear Dipole-Dipole Decoupling

For dilute nuclear spins S (e.g. ^{13}C with about 1% natural abundance) homonuclear dipole-dipole couplings do not need to be taken into account, since the probability of finding two neighbouring spins is fairly low. However the heteronuclear dipole-dipole coupling of the S spins and high abundance nuclear spins I (usually ^{1}H) is of the order of tens of kHz and leads to significant line broadening even under fast MAS.

Spins of different nuclear isotopes usually possess gyromagnetic ratios that are sufficiently different to separately manipulate them by r.f. pulses, due to the finite excitation bandwidth of the pulse. For this purpose, a double-resonance probehead is needed, where one

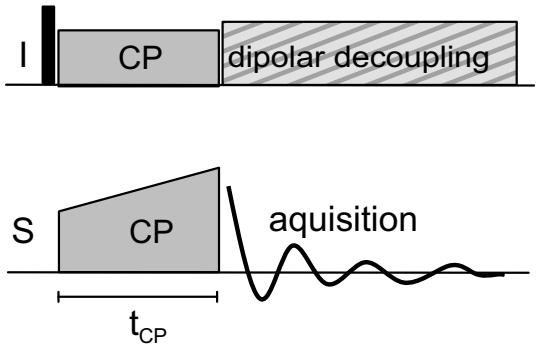

Figure 2.11: *The pulse sequence of the cross polarisation experiment.*

coil is addressed via two resonance circuits operating at the respective resonance frequencies. A continuous r.f. irradiation of field strength B_1 on the I spins leads to repeated transitions ($\uparrow \longleftrightarrow \downarrow$) at a rate determined by the amplitude of the r.f irradiation and hence to an oscillation of the heteronuclear dipole-dipole interaction with period $T = 2\pi/\gamma_I B_1$. Thus the Hamiltonian vanishes when averaged over a period T.

In this way, the line broadening can be suppressed by a continuous high power irradiation on the I spins during acquisition of the S spin, the so-called continuous wave (CW) decoupling (see Fig. 2.10). In order to achieve sufficient decoupling efficiencies strong r.f fields of 50-150 kHz need to be applied.

An intuitive way of understanding the decoupling effect is that the irradiation leads to a precession of the I spins around $\underline{B}_1$ and the S spin cannot 'see' its orientation anymore and is therefore not influenced, in other words, the I-S coupling is averaged to zero.

By CW decoupling the dipole-dipole coupling is only removed in first order. In the last years multi pulse decoupling schemes have been developed to achieve more efficient decoupling, especially for solids under fast MAS. In this thesis two-pulse phase-modulated (TPPM) decoupling was used [Bennett 95], that consist of the repeated sequence of two pulses with flip angles of approximately 170° and a phase difference in the order of 10° - 50° . This sequence has proven to be robust and more efficient than CW decoupling, since it also suppresses higher-order effects of the couplings.

2.4.4 Cross-Polarisation

While being unwanted during the acquisition, heteronuclear dipole-dipole couplings can also be useful in NMR experiments. From Eq. (2.22) it is clear that for a given tem-

perature and a static magnetic field, the observable magnetisation is proportional to the gyromagnetic ratio of the observed nucleus. This leads to a sensitivity problem for dilute spins with low gyromagnetic ratio (e.g. ^{13}C), which is even further aggravated by the fact that these nuclei usually have long T_1 relaxation times.

In the cross polarisation (CP) experiment [Pines 72, Pines 73] spin polarisation is transferred from high γ, high natural abundance nuclei (usually ^{1}H) to the nuclei of interest. The mediating coupling for this transfer is the dipole-dipole interaction. As described in Sec. 2.2.3 the flip-flop term is usually suppressed for heteronuclear dipole-dipole interactions. In CP experiments it is reintroduced for a certain time (called contact time), by application of r.f. pulses on I and S spins at the same time leading to near-degenerate Zeeman levels for

$$\gamma_S B_{1,S} = \gamma_I B_{1,I} \tag{2.74}$$

Under MAS this matching condition, called Hartmann-Hahn condition, changes to

$$\gamma_S B_{1,S} = \gamma_I B_{1,I} + n\omega_R \text{ with } n \in \mathrm{N} \tag{2.75}$$

with maximum signal for $n = \pm 1$. As the matching condition depends very sensitively on the $B_{1,S}/B_{1,J}$-ratio, it is preferable to use a ramped r.f. pulse amplitude on either channel as shown in Fig. 2.11, a technique introduced by Metz et al. [Metz 94]. For ^{1}H -^{13}C CP experiments the carbon signal can be enhanced up to a factor of four. Moreover, the repetition time of the experiment is then determined by the proton T_1 and no longer by the carbon T_1. It should be noted that the efficiency of the polarisation transfer depends on the local environment of the S spins (e.g. how many I spins they can couple to), and the spectra can, in principle, no longer be analysed quantitatively.

2.4.5 Two-Dimensional Experiments

In this section, the general principle of two-dimensional experiments will be described. A two-dimensional NMR data set is generated by introducing a second time variable t_1 in the experiment before the detection period (with time t_2). A set of FIDs is recorded with incremented t_1 and, after Fourier transformation in both dimensions, the two-dimensional NMR spectrum is obtained . As shown in Fig. 2.12, the state prepared in the first part of the experiment evolves during t_1, and the signal acquired in t_2 is amplitude modulated according to this evolution.

If phase sensitive detection in the indirect (t_1) dimension is needed, a suitable phase cycling scheme, incrementing the phase of all excitation pulses, has to be applied. A

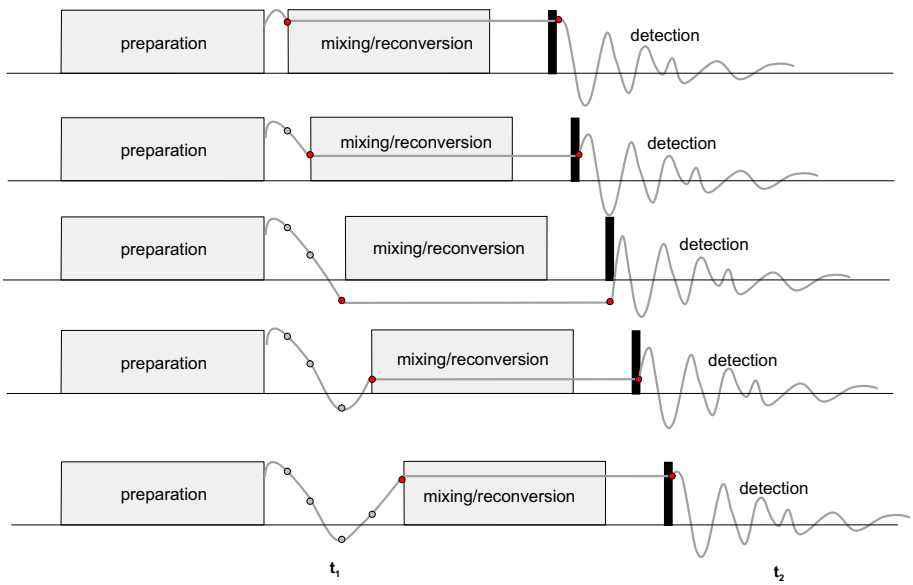

Figure 2.12: *Schematic illusration of a two-dimensional experiment.*

common method is time proportional phase incrementation (TPPI) [Marion 83] where the phase is incremented in steps of 90° with every t_1 increment Δt_1. Since real and imaginary parts are recorded sequentially, the effective t_1 increment is $2\Delta t_1$ and hence only half the spectral width is obtained in the indirect dimension. To record real and imaginary parts simultaneously, the phase is only incremented with every second t_1 increment, this method is referred to as States-TPPI [Marion 89] which is, effectively, a combination of the States method and TPPI. The required phase increment depends on the state of the system during t_1. For a single-quantum coherence evolving during t_1 the phase is changed by 90° . Under MAS t_1 can either be incremented in steps of full rotor period, yielding rotor synchronised spectra or in fractions of a rotor period to generate spinning sidebands in the indirect dimension.

Two dimensional NMR opens up the possibility of investigating coherences that cannot be detected directly by preparing them in a first step and, after evolution during t_1, reconvert them to a single-quantum coherence that can finally be detected during t_2.

2.5 Recoupling Methods

2.5.1 Basic Principles of Recoupling

As shown in section 2.3 anisotropic interactions can be averaged out by fast MAS. In solids this is usually essential to achieve spectral resolution. However, this gain of resolution comes at the cost of information on the geometry of the spin system that are inherent to the anisotropic interactions.

One way to regain the information on anisotropic interactions is slow magic angle spinning. The spectra then exhibit sideband patterns from which the information on anisotropic interaction tensors can be extracted as described in Section 2.3.3. Another possibility is slightly tilting the rotor axis away from the magic angle, so-called off magic angle spinning (OMAS) [Stejskal 77, Blümich 90, Schmidt-Rohr 94]. The interactions are then scaled by the second Legendre polynomial, and therefore drastically reduced, but nevertheless not completely averaged to zero. Both these techniques basically reduce the effect of magic angle spinning and therefore usually lead to line broadening and thus to reduced spectral resolution. Especially in the case of OMAS the scaled tensors tend to overlap for neighbouring lines. Another disadvantage is the fact that the interactions are recoupled during the entire experiment time. An exception to that is switched-angle sample-spinning (SASS) [Terao 86, Kolbert 90] where the angle of the rotor axis is changed during the experiment. This again is technically demanding and requires probes specially designed for this purpose. As a last point the reduction of the averaging effect of MAS is not at all selective with respect to the interactions that are recoupled, rather all interactions are affected equally.

A way to obtain information on anisotropic interactions without permanent reduction of the effect of MAS, is to make use of r.f. pulses to recouple the interactions. Since MAS only affects the space part of the interactions, and r.f. pulses only act on the spin part, the interactions can be manipulated without interfering with the MAS. The aim is to develop pulse sequences that recouple the interaction of interest temporarily and selectively, while the other interactions stay unaffected and are still averaged by MAS. This is especially advantageous when relatively small interactions in presence of larger interactions are investigated. The basic principle is to introduce a counter rotation in spin space that compensates the effect of MAS.

In the past decade a whole variety of methods have been developed for recoupling various interactions [Gullion 97, Lee 95, deAzevedo 99, Dusold 00, Schnell 01a, Saalwächter 02].

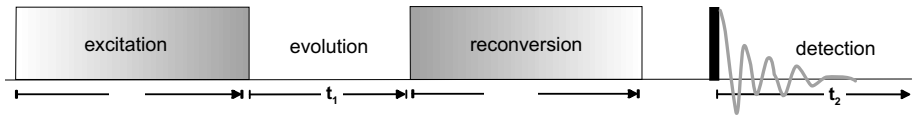

Figure 2.13: *Basic structure of a multiple-quantum experiment.*

Generally these experiments can be divided into two classes. The first class (so-called laboratory pulse sequences) makes use of short, high power pulses applied in a rotor synchronised fashion. According to Eq. (2.67) the Hamiltonian under MAS contains only terms modulated with ω_R and $2\omega_R$. Application of pulses that invert the sign of the spin part of the interaction, spaced by $\frac{\tau_R}{2}$ resp. $\frac{\tau_R}{4}$ compensates the averaging effect of MAS. For calculating the average Hamiltonian δ pulses are assumed. The second class of experiments (so-called rotating frame pulse sequences) employs relatively weak continuous r.f. irradiation, that lead to a continuous counter rotation of the spin part.

In the following sections the recoupling methods used in this thesis will be introduced, all of them belong to the first class of recoupling experiments.

2.5.2 Multiple Quantum NMR

Recoupling methods are frequently used for the generation of multiple-quantum coherences. An m-quantum coherence is a coherent superposition of two states, in which the order m is defined by the change of the overall quantum number, i.e the difference in z-angular moment of the connected states. The term multiple-quantum coherence is used for coherences with order $m \neq \pm 1$ (including zero-quantum coherences). An isolated spin-$\frac{1}{2}$ has two ZEEMAN energy levels and can therefore only exhibit single-quantum coherences. For a pair of two dipolar coupled spin-$\frac{1}{2}$ nuclei of the same kind as well as a single spin-1 nucleus, the energy diagram consists of three levels. These system can therefore exhibit double-quantum coherences.

As already described earlier, the signal induced in the NMR coil corresponds to a single quantum coherence. All other coherences do not lead to the induction of a signal in the NMR coil and can therefore not be detected directly. Hence, multi-quantum coherence experiments are inherently at least two dimensional and usually consist of four stages, as depicted in Fig. 2.13. In the first stage the m-quantum coherence is prepared and then evolves during t_1 under some internal interaction. During the reconversion period, the m-quantum coherence is reconverted into an observable single-quantum coherence that is finally detected during t_2

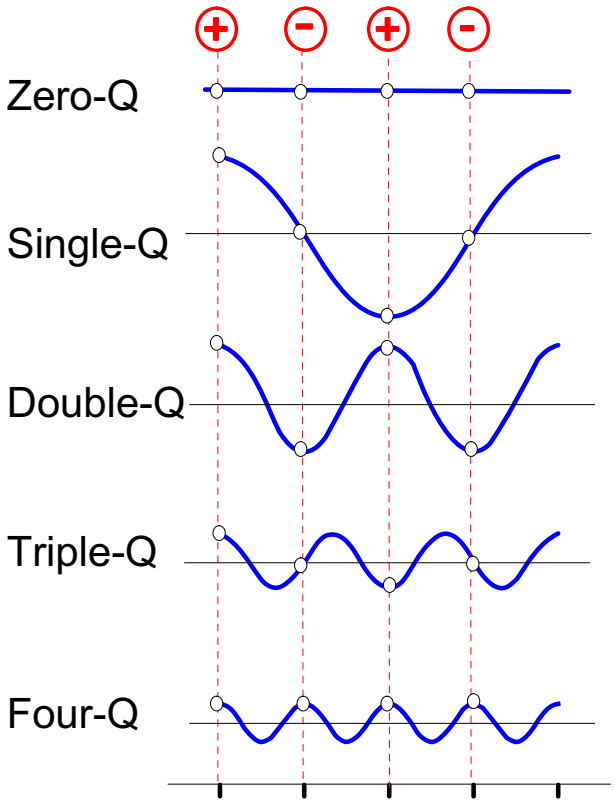

Figure 2.14: *Reaction of m-quantum coherences on a phase shift of the excitation pulses (ϕ). In red: phase cycle for the selection of double-quantum coherences*

To select the order of coherence an appropriate phase cycling scheme has to be applied. For a m-quantum coherence a phase shift $\Delta\Phi$ between the excitation and reconversion pulses leads to a phase shift of $m\Delta\Phi$. In Fig. 2.14 this is shown for the selection of a double quantum coherence. Summation over four experiments with $\Delta\Phi = 0, \frac{\pi}{2}, \pi, \frac{3\pi}{2}$ with alternating signs, leads to a cancellation of the signals of the zero-, single-, triple- and four-quantum coherence, while the signal of the double-quantum coherence is added up. In general, a phase cycle of N steps $\Delta\Phi = \frac{2\pi}{N}$, selects coherences of order $m \pm nN$ where n is an integer number.

It should be noted that also one-dimensional experiments using m-quantum excitation/reconversion exist, namely experiments where t_1 is not incremented. These experiments do not monitor the evolution of the m-quantum coherence, but rather act as m-quantum filters. In the obtained spectra the intensities of the lines are scaled according to the ability of the nuclei to form m-quantum coherences.

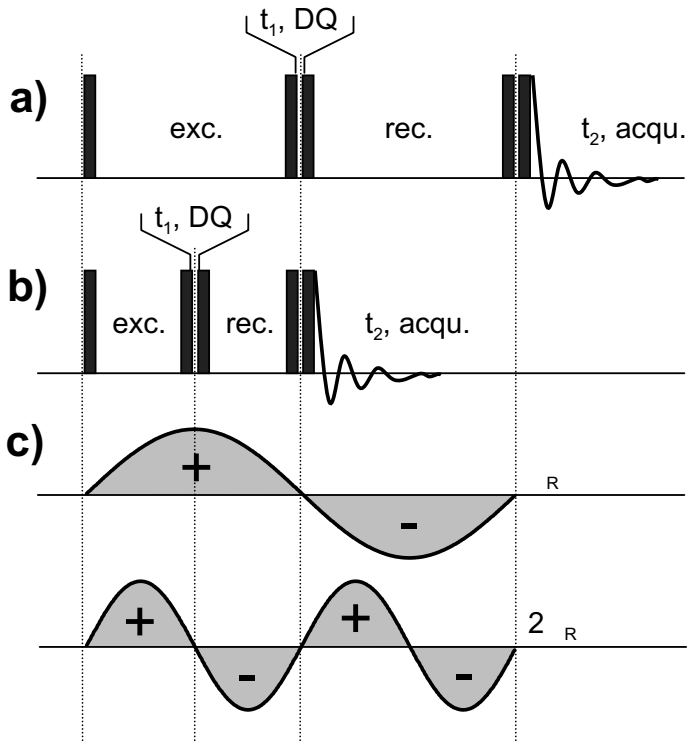

Figure 2.15: *Pulse sequence of the five-pulse experiment.*

2.5.3 The Five-Pulse Sequence

The five-pulse sequence is a simple pulse sequence suitable for the excitation of multi-quantum coherences, which can be used when only short excitation/reconversion times are required. It has been applied for the generation of multiple-quantum coherences in spin-$\frac{3}{2}$ and spin-$\frac{5}{2}$ systems [Friedrich 98], as well as in dipolar coupled spin-$\frac{1}{2}$ systems [Schnell 01a]. In the following, the application of this sequence for the excitation of double-quantum coherences (DQCs) in quadrupolar spin-1 systems will be described.

The most simple pulse sequence for the generation of DQCs consists of two 90° pulses spaced by a time τ:

$$\hat{I}_z \xrightarrow{\frac{\pi}{2}\hat{I}_y} \hat{I}_x \tag{2.76}$$

$$\xrightarrow{\int_0^\tau \hat{H}_\mathrm{Q}\mathrm{d}t} \hat{I}_x \cos(\Omega_\mathrm{Q}|_0^\tau) + 2i(\hat{I}_z\hat{I}_y + \hat{I}_y\hat{I}_z)\sin(\Omega_\mathrm{Q}|_0^\tau) \tag{2.77}$$

$$\xrightarrow{-\frac{\pi}{2}\hat{I}_y} \hat{I}_z \cos(\Omega_\mathrm{Q}|_0^\tau) + (\hat{I}_x\hat{I}_y + \hat{I}_y\hat{I}_x)\sin(\Omega_\mathrm{Q}|_0^\tau) \tag{2.78}$$

As described in the last section, the double quantum coherence $(\hat{I}_x\hat{I}_y + \hat{I}_y\hat{I}_x)$ cannot be

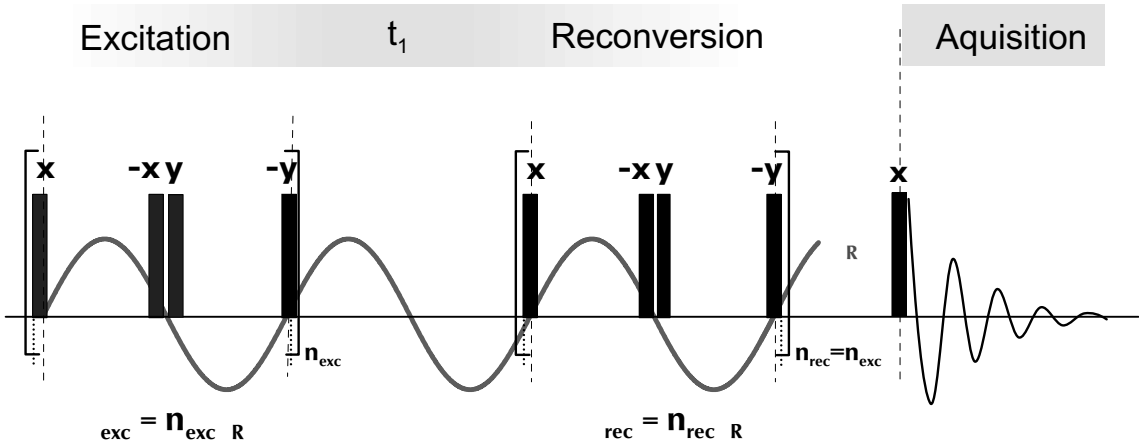

Figure 2.16: *Pulse sequence of the BABA experiment.*

detected directly and therefore needs to be converted back to observable magnetisation. This is done by applying the same pulse sequence again in order to make the system evolve back to longitudinal magnetisation $\hat{I}_z$, which is finally detected after applying a 90° pulse. By appropriate phase cycling of the excitation sequence with respect to the reconversion sequence the double quantum coherences are selected, and the experiment can schematically be represented by

$$\hat{I}_z \xrightarrow{\text{excitation}} (\hat{I}_x\hat{I}_y + \hat{I}_y\hat{I}_x)\sin(\Omega_Q|_0^\tau) \xrightarrow{\text{reconversion}} \hat{I}_z \sin(\Omega_Q|_0^\tau)\sin(\Omega_Q|_\tau^{2\tau}) \tag{2.79}$$

The pulse sequence is depicted in Fig. 2.15 for excitation times of $\tau = \frac{\tau_R}{2}$ and $\tau = \frac{\tau_R}{4}$. As can be seen by the schematic representation of the rotor modulations, the maximum excitation/reconversion time is $\tau = \frac{\tau_R}{2}$. For longer excitation/reconversion times the cancellation effects of MAS set in, as the Hamiltonian changes its sign after half a rotor period. Hence this pulse sequence is appropriate when relatively strong couplings are present, as they usually are found for quadrupolar nuclei, where short excitation times are in fact preferable to minimise relaxation effects. For weaker couplings, as for example weak dipole-dipole couplings, longer excitation times are required and the five-pulse sequence is not applicable. A recoupling technique designed for this purpose will be introduced in the following section.

2.5.4 The Back-to-Back Pulse Sequence

As described in the last section, excitation of DQCs over half a rotor period can simply be performed by applying two 90° pulses spaced by half a rotor period ($x - \frac{\tau_R}{2} - \bar{x}$). After half

a rotor period the Hamiltonian changes its sign. This can be compensated by a simple phase shift of the 90° pulses, using $(y-\frac{\tau_R}{2}-\bar{y})$ for the second half of the rotor period. The excitation scheme for one rotor period then takes the form $(x-\frac{\tau_R}{2}-\bar{x}y-\frac{\tau_R}{2}-\bar{y})$. This is the basic segment of the BABA sequence [Feike 96], that was introduced for the generation of homonuclear multiple-quantum coherences under MAS and, today, is routinely used for the determination of ^{1}H -^{1}H proximities and ^{1}H-^{1}H internuclear distances [Schnell 01a].

For the generation of double quantum coherences a proper phase cycling scheme has to be applied. The averaged Hamiltonian for one segment $(x-\frac{\tau_R}{2}-\bar{x}y-\frac{\tau_R}{2}-\bar{y})$ can be calculated as [Schnell 01b]

$$\hat{\bar{H}}_{BABA}=\frac{1}{\tau_R}\cdot 3\cdot\Phi_D\,|_0^{\frac{\tau_R}{2}}\left(\hat{T}^{ij}_{2,+2}+\hat{T}^{ij}_{2,-2}\right)=\frac{3}{\pi\sqrt{2}}D_{ij}sin(2\beta_{ij})cos(\gamma_{ij})\cdot\left(\hat{T}^{ij}_{2,+2}+\hat{T}^{ij}_{2,-2}\right). \tag{2.80}$$

For excitation/reconversion times of N rotor periods, the basic segment is applied N times.

The rotor synchronised version of the BABA experiment is frequently used to explore proximities among spin-$\frac{1}{2}$ nuclei. A schematic example is given in Fig. 2.17. Given a sample containing protons with two different chemical shifts ω_A and ω_B, double-quantum coherences of like spins give rise to single peaks in the spectrum, so-called "auto-peaks", at $(\omega_A, 2\omega_A)$ resp. $(\omega_B, 2\omega_B)$. Double-quantum coherences between spins of different chemical shift occur in the DQ dimension at the sum frequency $\omega_A+\omega_B$ and can be detected at both frequencies ω_A and ω_B in the single quantum dimension; hence, they are referred to as "cross peaks". Depending on the excitation/reconversion times and the strength of the dipole-dipole interaction spin-spin proximities in the range of several Å can be investigated.

2.5.5 Heteronuclear Dipole-Dipole Recoupling: REREDOR and REPT-HSQC

In this section two experiments designed for recoupling the heteronuclear dipole-dipole interaction will be presented. Both these experiments are based on REDOR-type [Gullion 89b, Gullion 89a, Gullion 90] π pulse trains,which will therefore be described before turning to the details of the two experiments. The REDOR recoupling is based on 180° pulses spaced by half a rotor period, which invert the sign of the Hamiltonian and thus recouple the heteronuclear dipole-dipole interaction that would otherwise be averaged by MAS.

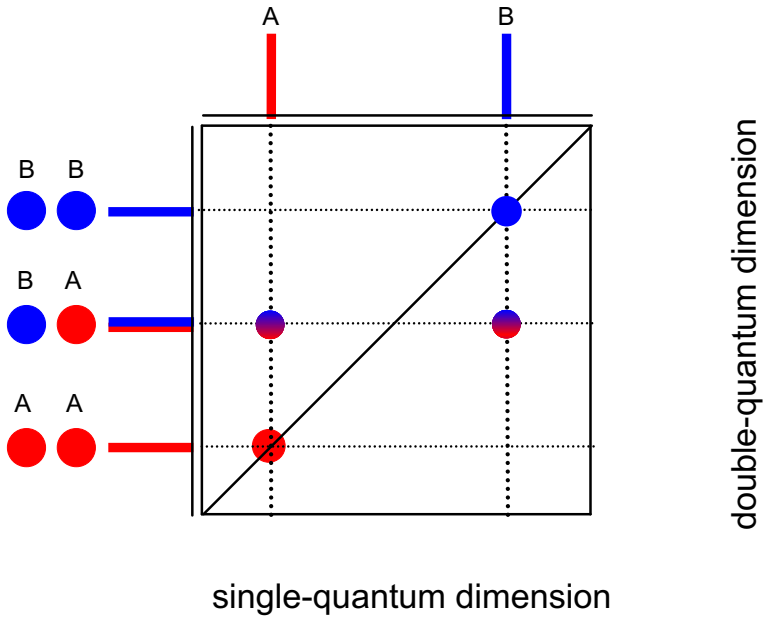

Figure 2.17: *Schematic representation of a two-dimensional rotor-synchronised BABA spectrum.*

Starting with transverse magnetisation on the I spins, and applying the pulses on the S spins, the evolution of the IS spin system during one REDOR segment is:

$$\hat{I}_x \xrightarrow{\Omega\, 2\hat{I}_z\hat{S}_z} \hat{I}_x \cos\Omega + 2\hat{I}_y\hat{S}_z \sin\Omega \tag{2.81}$$

$$\xrightarrow{\pi\hat{S}_x} \hat{I}_x \cos\Omega - 2\hat{I}_y\hat{S}_z \sin\Omega \tag{2.82}$$

$$\xrightarrow{\Omega'\, 2\hat{I}_z\hat{S}_z} \hat{I}_x\left(\cos\Omega\cos\Omega' + \sin\Omega\sin\Omega'\right) - 2\hat{I}_y\hat{S}_z\left(\sin\Omega\cos\Omega' - \cos\Omega\sin\Omega'\right)$$
$$\overset{\Omega=-\Omega'}{=} \hat{I}_x\cos 2\Omega - 2\hat{I}_y\hat{S}_z\sin 2\Omega \tag{2.83}$$

$$\xrightarrow{\pi\hat{S}_y} \hat{I}_x\cos 2\Omega + 2\hat{I}_y\hat{S}_z\sin 2\Omega \tag{2.84}$$

For clarity, the shorthand notations $\Omega = -\Omega_{D_{is}}|_0^{\frac{\tau_R}{2}}$ and $\Omega' = -\Omega_{D_{is}}|_{\frac{\tau_R}{2}}^{\tau_R}$ are used. Comparing Eq. (2.81) with Eq. (2.84) shows that the evolution over one rotor period of the recoupling π pulse train can conveniently be described by an average Hamiltonian,

$$\hat{\bar{H}}_{is} = \bar{\Omega}\, 2\hat{I}_z\hat{S}_z\frac{1}{\tau_R}, \quad \text{where} \tag{2.85}$$

$$\bar{\Omega} = 2\Omega = -2\Omega_{D_{is}}|_0^{\frac{\tau_R}{2}} = \frac{D_{is}}{\omega_R}2\sqrt{2}\sin 2\beta\sin\gamma. \tag{2.86}$$

Consequently, the evolution over a pulse train of N rotor periods length is given by

$$\hat{I}_x \xrightarrow{\hat{\bar{H}}_{is} N\tau_R} \hat{I}_x\cos\left(N\bar{\Omega}\right) + 2\hat{I}_y\hat{S}_z\sin\left(N\bar{\Omega}\right). \tag{2.87}$$

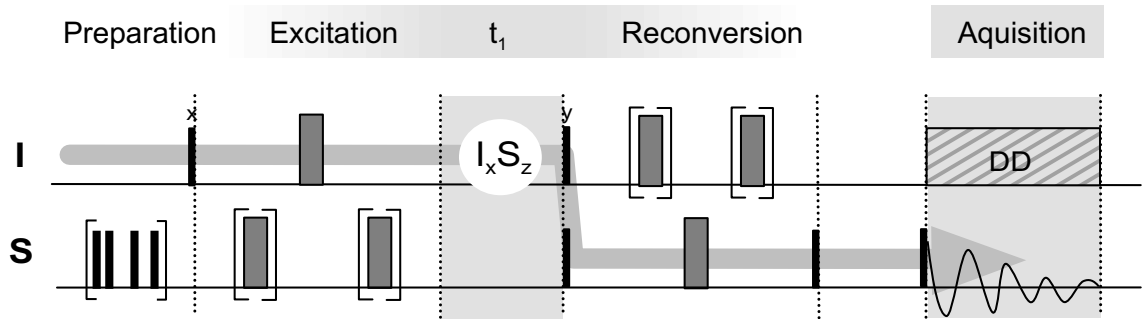

Figure 2.18: *Pulse sequence of the REPT-HSQC experiment.*

Since the 180° pulses only lead to an inversion of the sign, they can as well be applied on the I channel without changing the average Hamiltonian (see Eq. (2.82) and Eq. (2.84)). A whole variety of experiments were designed using the REDOR scheme that differ by the nucleus from which the recoupling process is started, the detected nucleus (either conventional X or inverse ^{1}H -detection), and the coherence state probed in the indirect dimension. In the following two of these will be described that were applied in this thesis.

REPT-HSQC

The REPT-HSQC (*re*coupled *p*olarization *t*ransfer - *h*eteronuclear *s*ingle *q*uantum *c*oherence) experiment is a two dimensional experiment correlating chemical shifts of two different nuclei I and S via the heteronuclear dipole-dipole coupling [Saalwächter 01]. The pulse sequence is depicted in Fig. 2.18. Starting from transverse I magnetisation the pulses in the first recoupling period are applied on the S spin with the exception of the central pulse that is applied on the I spin in order to refocus the CS evolution of the transverse I magnetisation during this period. In this way, a single-quantum coherence $\hat{I}_x\hat{S}_z$ is prepared that evolves during t_1 under the CS of the I spin and dipole-dipole couplings. At the end of t_1, two 90° pulses are applied on both channels to transfer the magnetisation to the S spin by interchanging transverse and longitudinal spin states between I and S spins. After the second recoupling period, where pulses now are applied on the S channel using again the central pulse on the I spin to refocus the CS evolution, the signal is acquired on the S channel.

When both dimensions are rotor synchronised, the t_1 evolution is only caused by the isotropic chemical shift of the I spins. After Fourier transformation in both dimensions a heteronuclear correlation spectrum is obtained, with I chemical shifts in the indirect and S chemical shifts in the direct dimension. The intensities of the peaks are determined by

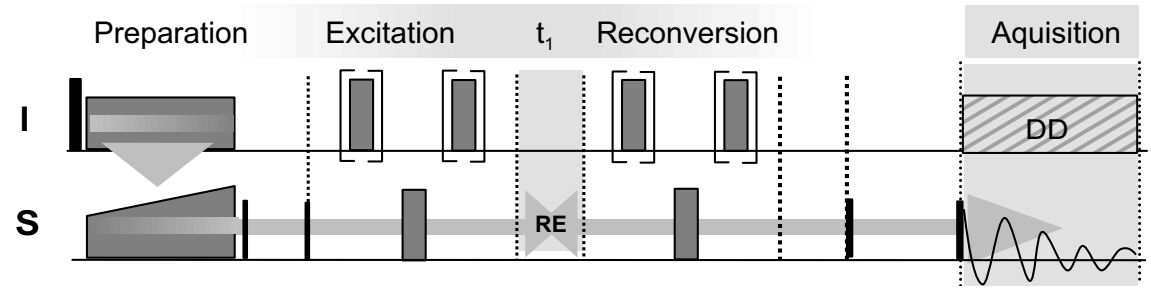

Figure 2.19: *Pulse sequence of the REREDOR experiment.*

the number of recoupling cycles and the strength of the ^{1}H -^{13}C dipole-dipole coupling. Heteronuclear correlation spectra are especially useful to assist proton assignment in samples with poor ^{1}H resolution.

REREDOR

The rotor encoded REDOR (REREDOR) pulse sequence is used to quantitatively determine heteronuclear dipole-dipole couplings in solids [Saalwächter 02]. It basically consists of two REDOR recoupling sequences with N_{exc} resp. N_{rec} π-pulse segments spaced by t_1. As depicted in Fig. 2.19, in an initial CP step transversal S magnetisation is prepared that is then exposed to the heteronuclear dipole-dipole coupling during two recoupling periods and finally detected during t_2. A second t_1 delay is inserted after the reconversion period to ensure the total refocussing of the CS evolution of the transverse S magnetisation by the central refocussing pulses. After Fourier transformation of the direct dimension, the signal intensity in dependence of t_1 for an S spin coupling to N spins $I^{(i)}$ is given by:

$$S \sim \langle \prod_{i=1}^{n} cos\left(N_{\mathrm{exc}} \bar{\Omega}_0^{(i)} - \Omega^{(i)} |_{0}^{t_1} - N_{\mathrm{rec}} \bar{\Omega}_{t_1}^{(i)} + \Omega^{(i)} |_{t_1}^{2t_1} \right) \rangle_{\beta,\gamma}. \tag{2.88}$$

If t_1 is incremented in fractions of a rotor period, the amplitude modulation of the signal in the indirect dimension monitors the heteronuclear dipole-dipole coupling strength. A Fourier transformation of this signal leads to sideband patterns (see Fig. 2.20) from which the dipole-dipole coupling constant can be deduced.

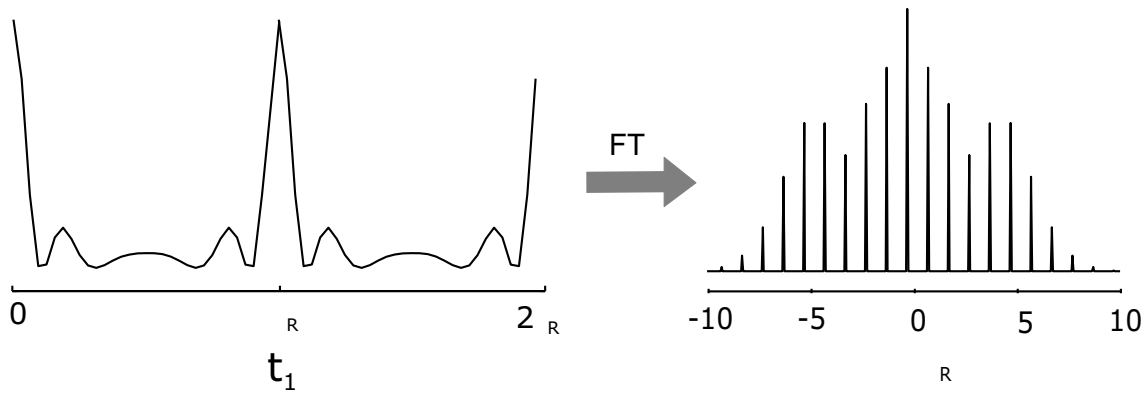

Figure 2.20: *Evolution of the REREDOR signal in the indirect dimension and the sideband pattern obtained after Fourier transformation.*

Chapter 3

Solid State NMR Methods

As described in the last chapter, anisotropic interactions, such as the dipole-dipole interaction, the chemical shift anisotropy, and the quadrupole interaction, contain information on molecular structure and dynamics. As these interactions are averaged under fast MAS numerous solid-state NMR techniques have been developed which enable the selective restoration of certain anisotropic properties [Gullion 97, Lee 95, deAzevedo 99, Dusold 00, Schnell 01a, Saalwächter 02, Stejskal 77, Blümich 90, Terao 86]. In this chapter NMR experiments recoupling the quadrupolar interaction and the dipole-dipole interaction are presented.

In general quadrupole couplings are very strong and can reach the same order as the Zeeman interaction. In these cases, solid state NMR experiments are technically demanding since short high power pulses are required to achieve a large excitation bandwidth and the achievable MAS spinning speeds do not sufficiently average the quadrupole interaction. A special case of quadrupolar nuclei are ^{2}H and ^{7}Li , because their typical quadrupole couplings hardly exceed 300 kHz and are thus only by a factor of $<$10 stronger than the strongest dipole-dipole couplings.

In the first part of this chapter a two-dimensional ^{2}H NMR experiment, performed under off-magic-angle spinning, is presented, which allows for site-selective determination of quadrupole coupling parameters in samples deuterated at multiple sites. In the second part the possibility to investigate the electronic environment and mobility on lithium ions with ^{7}Li single- and multiple-quantum NMR experiments is demonstrated. In the last part of this chapter the precision of proton-carbon distances, measured via the ^{1}H -^{13}C dipole-dipole interaction in REREDOR experiments will be discussed.

3.1 The OMAS Experiment

Solid-State ^{2}H NMR is a well-established method to study molecular orientation and dynamics. Its success is based on the detailed information on molecular orientation, reorientation and/or motional process provided by characteristic ^{2}H line shapes [Macho 01, Schmidt-Rohr 94]

As ^{2}H is a spin-1 nucleus, the ^{2}H resonance is governed by the quadrupolar interaction. However, compared to other quadrupolar nuclei the ^{2}H quadrupole moment is rather low, leading to typical couplings δ of $\frac{\delta}{2\pi} \approx 130$ kHz in solids. Due to its low natural abundance of only 0.0155%, ^{2}H virtually always needs to be isotopically enriched in the sample. This in turn provides perfect site selectivity as long as chemical synthesis allows the site of interest to be deuterated in a fully selective fashion. However, this synthetic effort may still form an undesirable obstacle that calls for simplification.

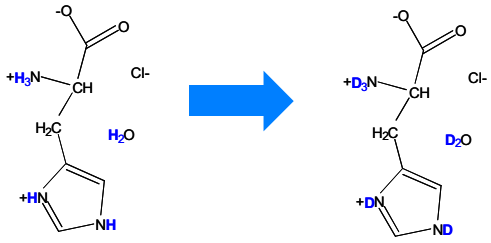

Figure 3.1: *Exchange of acidic protons in L-histidine hydrochloride monohydrate during recrystallisation from D_2O.*

Acidic protons, when found at multiple sites in a sample, generally cannot be deuterated selectively since they usually exchange all together. This in turn provides a relatively easy way to prepare samples deuterated at multiple sites, namely by simply exposing the material to a deuterated solvent capable of exchanging its deuterons with the solubilised material. Recrystallisation from D_2O, for example, places deuterons at all sites with sufficient acidity, that is, predominantly NH_n and OH in organic samples, as shown in Fig. 3.1 for L-histidine hydrochloride monohydrate recrystallised from D_2O. Deuteration of these sites is especially interesting for the investigation of hydrogen bonds, as the quadrupole coupling parameter is known to show a dependence on the bond strength [Hunt 74].

The major drawback of ^{2}H NMR spectra of samples deuterated at multiple sites is the fact that the quadrupole coupling for ^{2}H is in the range of 100 kHz, while the chemical shift covers only a range of about 130 Hz per Tesla of the static magnetic field B_0. Thus the resulting static spectra consist of a superposition of lines, as shown in Fig. 3.2 for D_7-L-histidine hydrochloride monohydrate , and it is usually difficult to decompose these line into the contributions arising from different sites. Under MAS the quadrupole coupling, being an inhomogeneous interaction, is refocused after one rotor period, and in spectra recorded in a rotor synchronised fashion only the evolution under the isotropic chemical

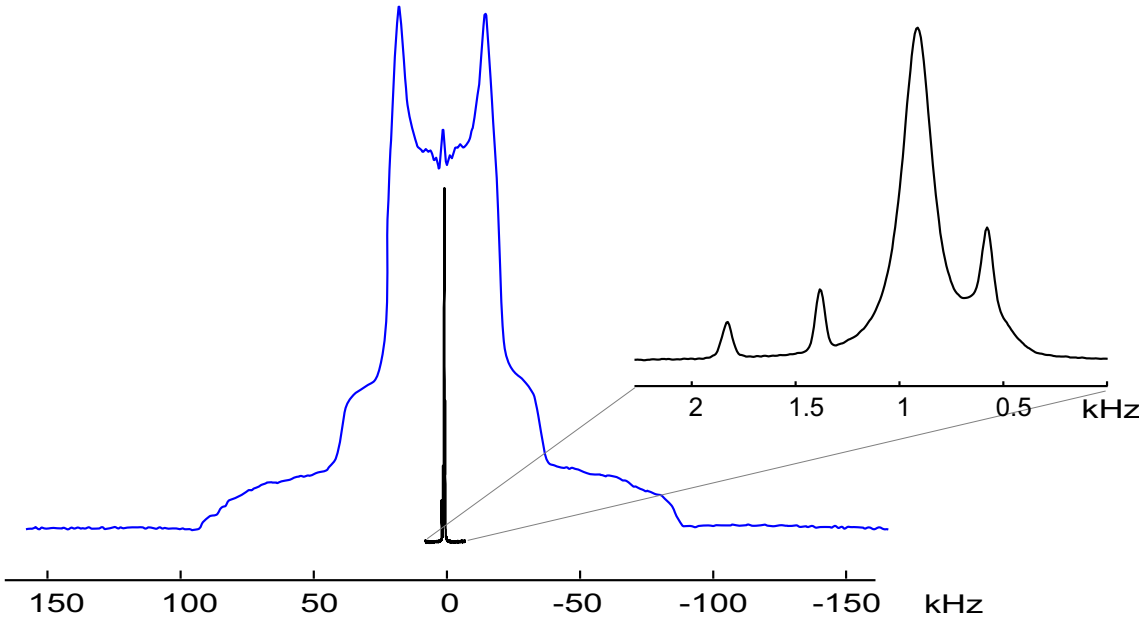

Figure 3.2: *Static ^2H NMR (blue) and 30 kHz MAS ^2H NMR spectrum (black) of L-histidine hydrochloride monohydrate recrystallised from D_2O.*

shift is observed (see Fig. 3.2). In this way, it is possible to obtain ^{2}H NMR spectra with chemical shift resolution; at the same time however, the information on the quadrupole interaction is completely lost.

In principle, this information can be extracted from the spinning sideband patterns observed when acquiring the rotor modulations. In practice, however, spinning sidebands have shown to be only little reliable for the determination of small asymmetry parameters [Hodgkinson 97], and the low spinning speeds required to obtain large numbers of sidebands mean a loss of spectral resolution. This will be discussed in detail later. An obvious strategy to solve this problem is the development of a two-dimensional experiment which correlates chemical shift resolution in one dimension with information on quadrupolar coupling parameters in the other dimension. To determine quadrupole couplings in MAS experiments, the information on the quadrupolar interaction must be restored in some way. In principle, numerous recoupling pulse sequences have been developed, which selectively re-introduce anisotropic interactions in MAS experiments [Dusold 00, Gullion 97, Gullion 89b, Saalwächter 01, Brinkmann 00]. Such recoupling approaches are established and perform well in the case of dipole-dipole couplings or CSAs of spin-$\frac{1}{2}$ nuclei. For nuclei with spin $> \frac{1}{2}$, however, recoupling pulse sequences are usually not applicable due to strong quadrupolar interactions which exceed the tech-

nical limits of MAS frequencies and give rise to fast relaxation processes. Moreover, an unrealistically broad excitation bandwidth of the pulse sequence would be required. An alternative means of (partially) restoring an anisotropic interaction under MAS conditions is a misadjustment of the magic angle, which can be realised either temporarily by switching the angle between the "magic" and another orientation during the experiment (so-called switched-angle sample spinning, SASS) [Terao 86, Kolbert 90] or permanently by slightly misadjusting the angle (usually referred to as off-MAS or OMAS) [Stejskal 77, Blümich 90, Schmidt-Rohr 94]. The SASS approach is technically more demanding, as it requires equipment capable of fast angle switching, while OMAS experiments can straightforwardly be performed on conventional MAS probes. In the following sections, ^{2}H NMR experiments performed under magic-angle spinning as well as the design of a two-dimensional ^{2}H experiment performed under off-magic-angle spinning will be presented.

3.1.1 ^{2}H NMR under Fast MAS

As described in Sec. 2.3.3, the quadrupolar interaction is averaged over a full rotor period under magic-angle spinning. By data acquisition in a rotor synchronised fashion, spinning sidebands are avoided, and the obtained spectra contain the pure chemical shift information.

Fig. 3.3 shows the spectrum of fully protonated L-histidine hydrochloride monohydrate. Two low-field NH resonances are observed at 12.7 ppm and 17.0 ppm, indicating a weaker and a stronger hydrogen-bond of the NH protons. The line arising from the crystal water is observed at 5.3 ppm, while the CH and CH_2 proton resonances cannot be resolved and give rise to a single line at 3 ppm. The assignment of the lines originating from the two aromatic protons as well as from the ammonium group is hampered by the overlap of these lines. The sample was then recrystallised from D_2O leading to a replacement of the acidic protons by deuterons, namely D_2O, ND_3, and ND. In the ^{1}H spectra of the sample, only the CH/CH_2 and aromatic potons give rise to lines with considerable intensities (small peaks originating from residual acidic protons are still observed), while in the ^{2}H spectrum resonances are only observed for the positions that were capable of proton-deuteron exchange. From this it is obvious that selective deuteration of acidic protons is a simple method to assist ^{1}H peak assignment.

This becomes even more apparent in the case of cytosine monohydrate. In the ^{1}H spectrum of fully protonated cytosine, only the NH signal at 12.7 ppm is clearly resolved,

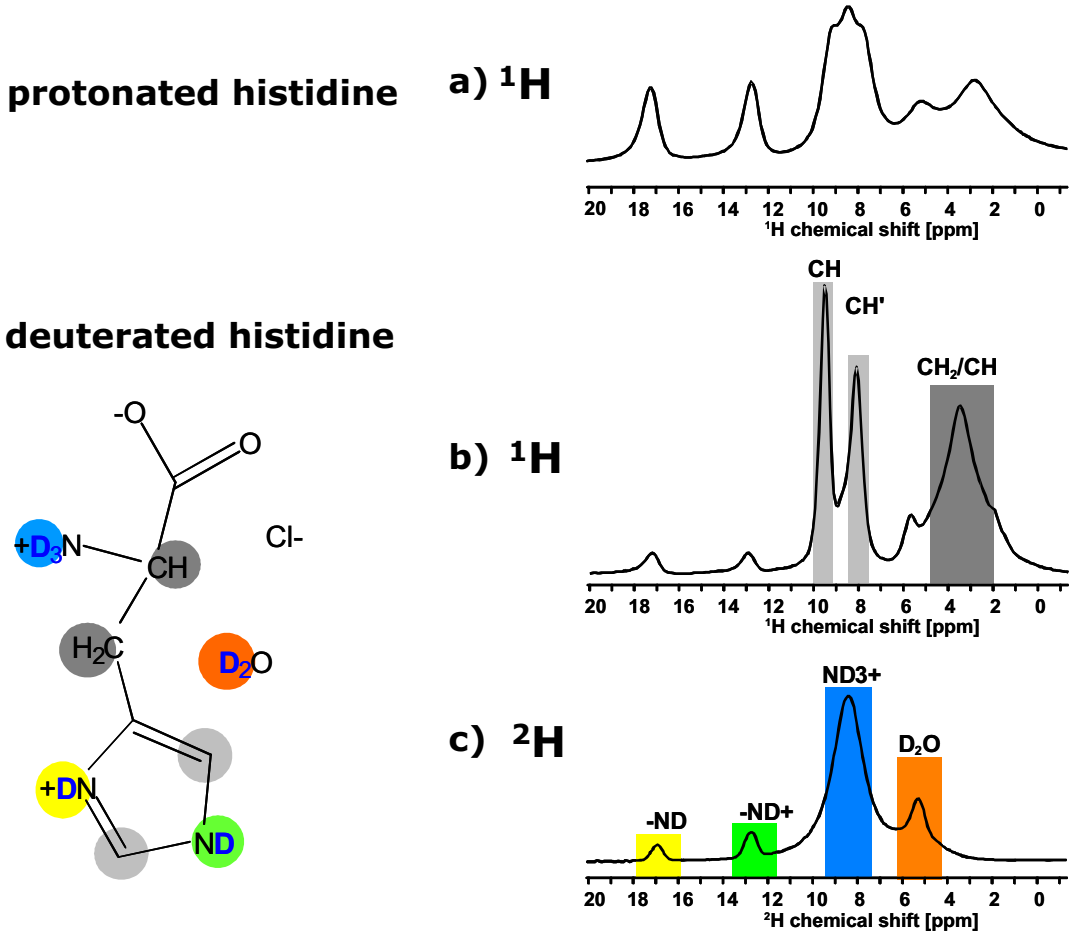

Figure 3.3: *(a) ^1H MAS spectrum of L-histidine hydrochloride monohydrate. (b) ^1H MAS NMR and (c) ^2H MAS NMR spectrum of the same compound after recrystallisation from D_2O.*

while all other lines overlap (see Fig. 3.4a). After recrystallisation from D_2O, both aromatic protons are clearly resolved in the ^1H NMR spectrum (Fig. 3.4b), while the ^2H spectrum allows all deuterated positions to be assigned.

It should be noted that the ^1H and ^2H NMR spectra are equally well resolved. Compared to protons, deuterons have a reduced chemical-shift dispersion due to their lower gyromagnetic ratio. At first sight, this seems to be a considerable disadvantage, but the lower dispersion is experimentally found to be compensated by the fact that ^2H resonance lines are broadened to a lesser extent than ^1H resonance lines, because deuterons experience weaker dipole-dipole couplings than protons. Furthermore, the ^1H and ^2H resonance lines are observed at practically the same positions. In principle, the chemical shift of

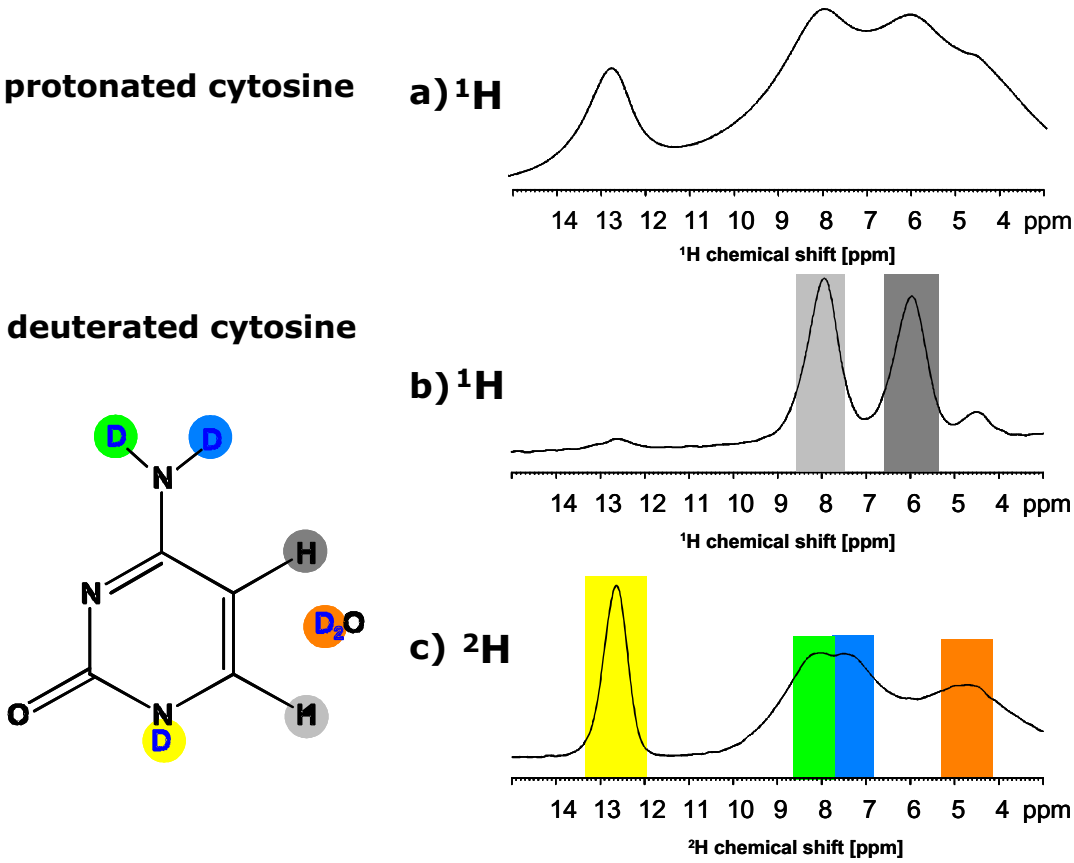

Figure 3.4: *(a) ^1H MAS spectrum of cytosine monohydrate. (b) ^1H MAS NMR and (c) ^2H MAS NMR spectrum of cytosine monohydrate recrystallised from D_2O.*

deuterons in hydrogen-bonds is expected to be somewhat smaller than that of protons, as the zero-point vibration energy of deuterium is smaller and the hydrogen-bond is weaker. Additionally, the vibrational averaging might cause shift differences, as the amplitudes of vibrations are smaller for deuterons. However, these effects are either too small to be resolved in solid-state NMR spectra or too small to clearly distinguish them from effects arising from slightly different crystallisation conditions.

3.1.2 Off-Magic-Angle Spinning and Double-Quantum Coherences

As shown in the previous section, magic-angle spinning facilitates the acquisition of chemical shift resolved ^{2}H NMR spectra. However, the information on quadrupole coupling parameters is entirely lost in these spectra, since the quadrupole interaction is averaged

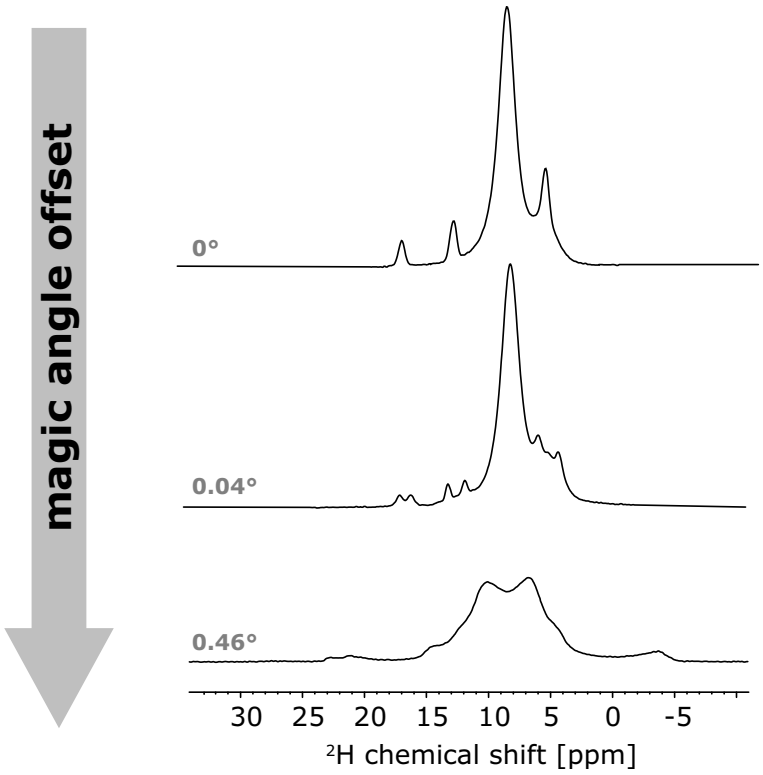

Figure 3.5: *^{2}H NMR spectra of L-histidine hydrochloride monohydrate recrystallised from D_2O recorded under spinning at 29762 Hz with increasing magic-angle offset.*

to zero. A method to regain this information is to slightly tilt the rotor axis away from the magic angle, whereby the quadrupole interaction is no longer completely averaged. Fig. 3.5 shows rotor-synchronised spectra of deuterated L-histidine hydrochloride monohydrate for increasing magic-angle offset. As the quadrupole coupling is relatively large, even a slight misadjustment of the magic angle leads to a splitting of the lines. While the anisotropy parameter might be extracted from these splittings, they are still too small to allow the asymmetry to be determined. The line originating from the ND_3 deuterons is not split, as the rotation of the ammonium group leads to a reduction of the quadrupole coupling by motional averaging. When further missetting the magic angle, the lines start resembling the typical line shapes observed in static ^{2}H NMR (and are therefore from now on referred to as *quasistatic* line shapes). However, the lines arising from different positions unfortunately start to overlap and the chemical shift resolution is again lost. It is therefore desirable to develop a two dimensional experiment that correlates this quasistatic line shapes, containing the information on quadrupolar coupling parameters, with the isotropic chemical-shift information.

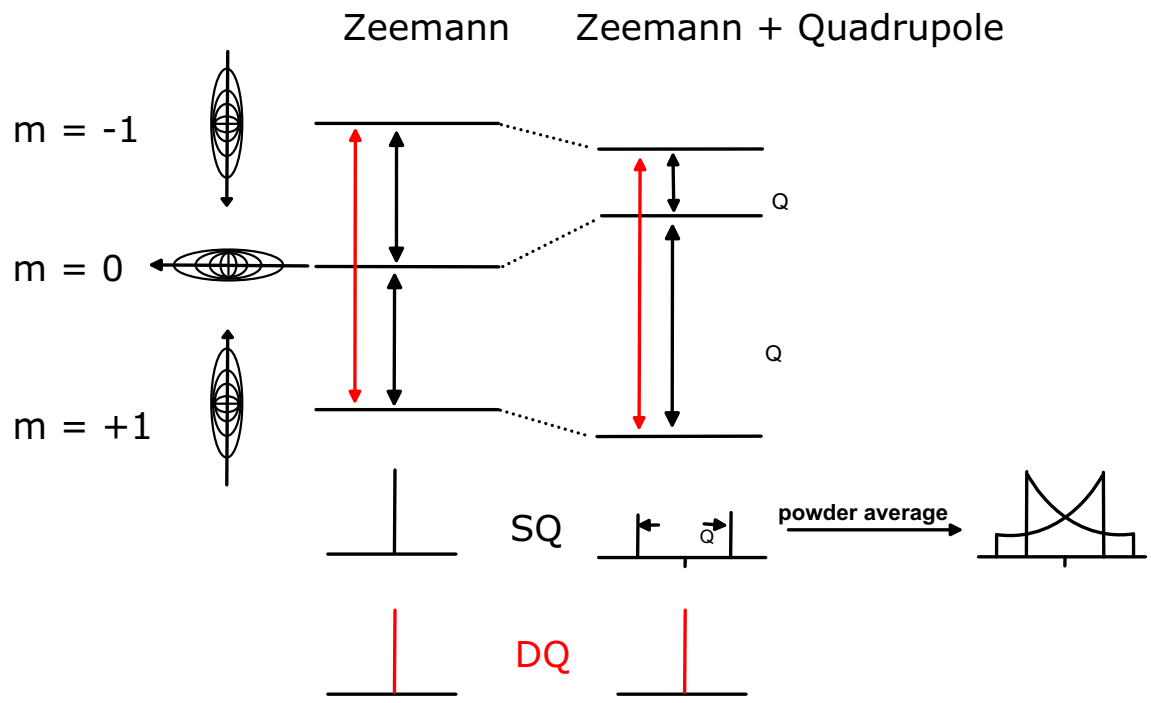

Figure 3.6: *Energy level diagram of a spin-1 nucleus. The DQ transition (red) is not affected by the quadrupole interaction.*

From an illustration of the energy level diagram (see Fig. 3.6) of a spin-1 nucleus, it can be seen that the double-quantum transition is not affected by first-order quadrupole interactions. In the presence of the quadrupole interaction, the three former equidistant energy levels are shifted, leading to different resonance frequencies for the two possible single-quantum transitions ($\pm 1 \leftrightarrow 0$). The shift of the energy levels and, thus, the resonance frequencies of these transitions depend on the orientation of the molecule with respect to the magnetic field ($\omega_Q = \frac{\delta}{2}[3\cos^2(\theta) - 1 + \eta \sin^2(\theta)\cos(2\phi)]$). For a powdered sample, the obtained spectra are the sum of the lines originating from all crystallite orientations, resulting in the classical static line shapes. The double-quantum transition ($+1 \leftrightarrow -1$), however, is not affected by first-order quadrupole interactions, since the +1 and -1 energy level experience the same shift. Thus, the DQ spectrum consists of a single line even in the presence of the quadrupole interaction, and DQ coherences should therefore not be affected by misseting the magic angle. Based on this, a ^{2}H DQ NMR experiment performed under OMAS conditions was designed, which correlates the isotropic chemical shift in the DQ dimension with DQ-filtered quasistatic line shapes in the single-quantum dimension. The five-pulse sequence introduced in Sec. 2.5.3 has proven to be a robust

sequence for DQ excitation in quadrupolar nuclei and was therefore chosen for this experiment. In the following, its application under off-magic-angle spinning conditions will be presented.

3.1.3 The Five-Pulse Sequence under OMAS Conditions

In Sec. 2.3.2, the expressions for the integrated phases were derived for spinning the sample at the magic angle, i.e. setting $\beta_{\mathrm{M}} = 54.7°$ when transforming $A_{2,0}$ from the principal axis system (PAS) to the laboratory frame (LAB) (Eq. (2.65)). To obtain the integrated phases for off-magic-angle spinning we now have to perform this transformation for arbitrary β_{M}, yielding:

$$A_{20}^{Q,LAB}(t) = \sum_{m=-2}^{2}\left[\sum_{m'=-2}^{2} A_{2-m'}^{\lambda,PAS}\,\mathcal{D}_{-m'-m}^{(2)}(\Omega)\right] e^{im\omega_R t}\, d_{-m0}^{(2)}(\beta_M) \tag{3.1}$$

$$\begin{aligned}
= \frac{\delta}{8}&[3\sin^2(\beta)\sin^2(\beta_{\mathrm{M}})\cos(2\omega_{\mathrm{R}}t+2\gamma)\\
&-3\sin(2\beta)\sin(2\beta_{\mathrm{M}})\cos(\omega_{\mathrm{R}}t+\gamma)\\
&+(3\cos^2(\beta)-1)(3\cos^2(\beta_{\mathrm{M}})-1)]\\
&+\sqrt{\tfrac{3}{8}}\delta\eta[\tfrac{1}{2}(1-\cos(\beta))^2\sin(\beta_{\mathrm{M}})\cos(2\omega_{\mathrm{R}}t+2\gamma-2\alpha)\\
&+\tfrac{1}{2}(1+\cos(\beta))^2\sin(\beta_{\mathrm{M}})\cos(2\omega_{\mathrm{R}}t+2\gamma+2\alpha)\\
&-(1-\cos(\beta))\sin(\beta)\sin(2\beta_{\mathrm{M}})\cos(\omega_{\mathrm{R}}t+\gamma-2\alpha)\\
&+(1+\cos(\beta))\sin(\beta)\sin(2\beta_{\mathrm{M}})\cos(\omega_{\mathrm{R}}t+\gamma+2\alpha)\\
&+\sin^2(\beta)(3\cos^2(\beta_{\mathrm{M}})-1)\cos(2\alpha)]
\end{aligned} \tag{3.2}$$

From this, the integrated quadrupolar phase can be calculated as

$$\Omega_{\mathrm{Q}}|_{t_1}^{t_2} = \int_{t_1}^{t_2} A_{20}^{Q,LAB}(t)dt. \tag{3.3}$$

The full expression is given in Appendix D. As shown in the last section, quasistatic line shapes can be reintroduced into MAS experiments by slightly misadjusting the magic angle and recording the spectra in a rotor-synchronised fashion. Formally, by means of rotor-synchronised acquisition, the signal $S(t)$ can be expressed as

$$S(t) \sim \cos(\Omega_{\mathrm{Q}}|_0^{\tau_{\mathrm{R}}}\, t) \tag{3.4}$$

with

$$\Omega_{\mathrm{Q}}|_0^{\tau_{\mathrm{R}}} = \frac{\delta\tau_{\mathrm{R}}}{4}[3\cos^2(\beta)-1+\eta\sin^2(\beta)\cos(2\phi)][3\cos^2(\beta_{\mathrm{M}})-1]. \tag{3.5}$$

This fully resembles the dependence of a signal observed in a static ^{2}H experiment apart from the scaling factor $\frac{1}{2}(3\cos^2(\beta_M)-1)$, which is a small number for β_M close to the magic angle. According to Eq. (2.79) the signal $S(t)$ of a DQ-filtered experiment recorded in rotor-synchronised fashion is

$$S(t) \sim \sin(\Omega_Q|_0^\tau)\sin(\Omega_Q|_\tau^{2\tau})\cos\left[\frac{\delta}{4}[3\cos^2(\beta)-1+\eta\sin^2(\beta)\cos(2\phi)][3\cos^2(\beta_M)-1]t\right]. \tag{3.6}$$

It contains two additional factors which arise from the excitation and reconversion period of the DQ experiment. They represent signal weighting factors that reflect the orientation dependence of the DQ filter. The experiment is usually performed with either $\tau = \frac{\tau_R}{4}$, which is the maximum DQ excitation time without partial cancellation of the interaction, or $\tau = \frac{\tau_R}{2}$, where the situation is simplified by the fact that the $2\omega_R$-modulated terms are averaged and, as a consequence of this, the orientation dependence of Ω_Q is drastically reduced.

To calculate theoretical line shapes, a suitable powder averaging has to be applied. Fig. 3.7 shows such patterns for a symmetric quadrupole coupling (i.e. $\eta = 0$) calculated with a magic-angle offset of 1° and an OMAS frequency of 29762 Hz. The patterns strongly depend on the quadrupole coupling and the time τ used for DQ excitation and reconversion. The patterns observed for $\tau = \frac{\tau_R}{2}$ are very similar to the conventional PAKE patterns, altough their width is drastically reduced (by a factor of $\approx 2.5 \times 10^{-2}$), whereas the patterns obtained with $\tau = \frac{\tau_R}{4}$ change more drastically with the coupling. The wavy line shape of the latter with strong negative contributions arises from the combination of ω_R- and $2\omega_R$-modulated terms in the integrated quadrupolar phase (see Appendix D). The patterns for $\tau = \frac{\tau_R}{2}$ appear cleaner, because only the ω_R modulated terms contribute to Ω_Q. Thus, by choosing τ and/or combining results obtained for different τ, the sensitivity of the measurement can be adjusted.

3.1.4 Experimental Implementation

Fig. 3.8 shows the dependence of the quasistatic ^{2}H line shapes observed in DQ-filtered experiments on the magic-angle offset. A comparison of these lines with the lines obtained for a fixed magic angle and various coupling strengths (Fig. 3.7) reveals that a change of the magic-angle offset has almost the same effect as changing the anisotropy parameter. This can also be seen in Eq. (3.6): Apart from the two amplitude modulating factors arising from the angular dependence of the DQ filter, the anisotropy is basically scaled

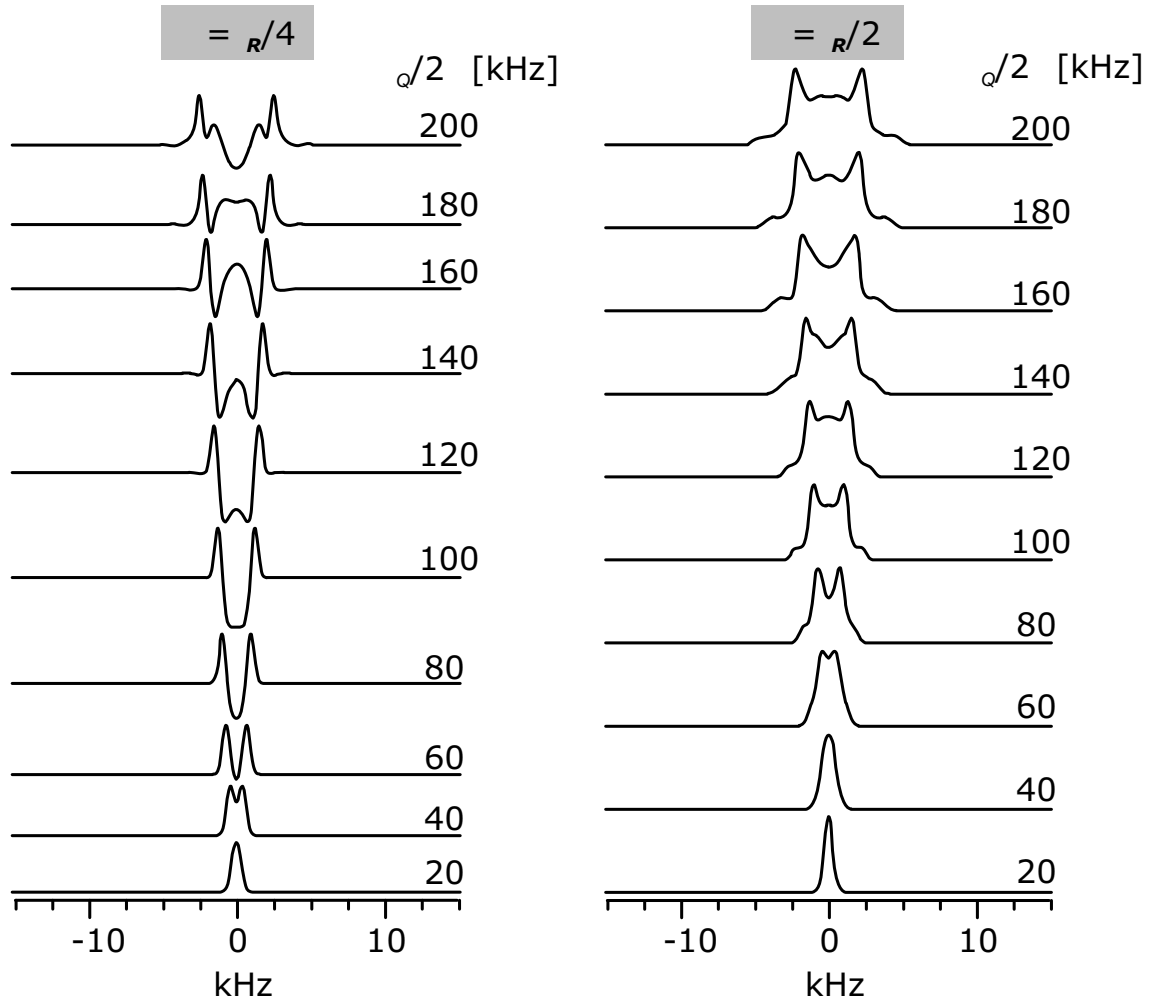

Figure 3.7: *DQ-filtered ^2H OMAS line shapes calculated using Eq. (3.6) with $\tau = \frac{\tau_R}{4}$ and $\tau = \frac{\tau_R}{2}$ for symmetric quadrupole couplings $\frac{\delta}{2\pi}$ and a magic angle offset of 1° .*

by the second Legendre polynomial. Thus, to extract the quadrupole coupling parameters from this line shape, it is inevitable to precisely determine the magic angle offset. A direct measurement of the angle to such a degree of precision is technically not possible.

As described earlier (see Eq. (3.5)), the line shape obtained in a single pulse MAS experiment using rotor synchronised acquisition resembles that of a static experiment scaled by the second Legendre polynomial. This provides the possibility of precisely determining the slight misadjustment of the magic angle by comparison of the static and MAS line shapes of a suitable substance. In this work methylene deuterated *p*-nitro-benzylalcohol (NBZOH) was used for magic-angle calibration. Firstly, it provides high enough signal intensity and short relaxation times to set the magic angle "on-line" by detecting the

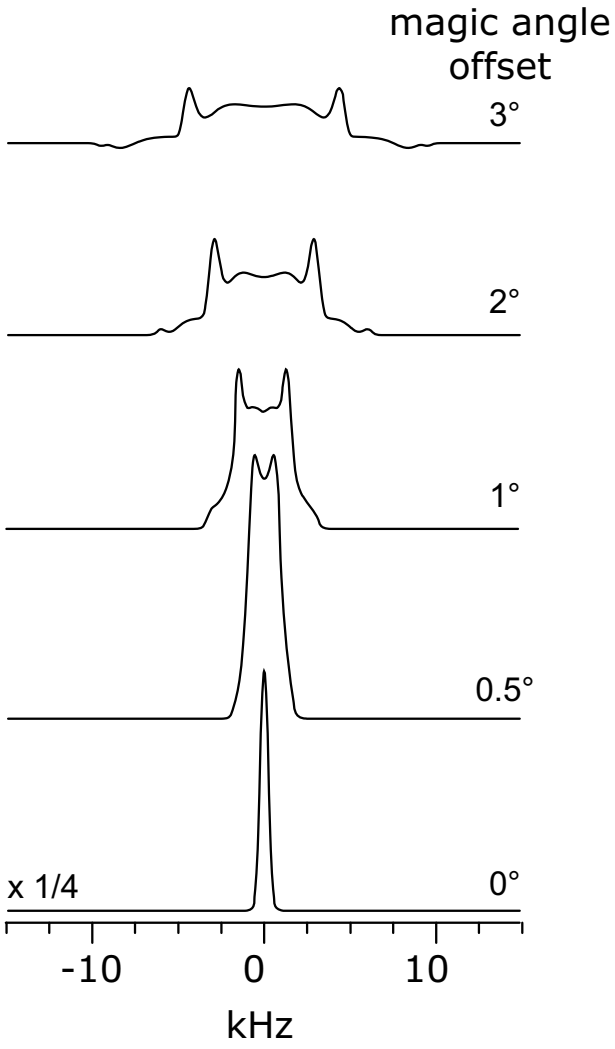

Figure 3.8: *DQ-filtered ^2H OMAS line shapes calculated using Eq. (3.6) with $\tau = \frac{\tau_R}{2}$, $\frac{\delta}{2\pi} = 128$ kHz and different magic angle offsets.*

signal of one scan every second. This is especially useful when it comes to resetting the magic angle. Secondly, the quadrupole coupling of the deuterons in this compound is large enough to allow even small magic-angle offsets to be determined precisely. A static ^{2}H NMR spectrum of NBZOH is shown in Fig. 3.9a. From this, the quadrupole coupling $\frac{\delta}{2\pi} = 101$ kHz and the asymmetry parameter $\eta = 0.16$ were obtained using standard ^{2}H line-shape analysis. From a single-pulse spectrum recorded under OMAS conditions, the angle between rotor axis and magnetic field β_M can be obtained by simply scaling the frequency axis of the static spectrum by the second Legendre polynomial $P_2(\beta_M) = \frac{1}{2}(\cos^2(\beta_M) - 1)$ until it fits the ^{2}H OMAS line (Fig. 3.9b). The difference

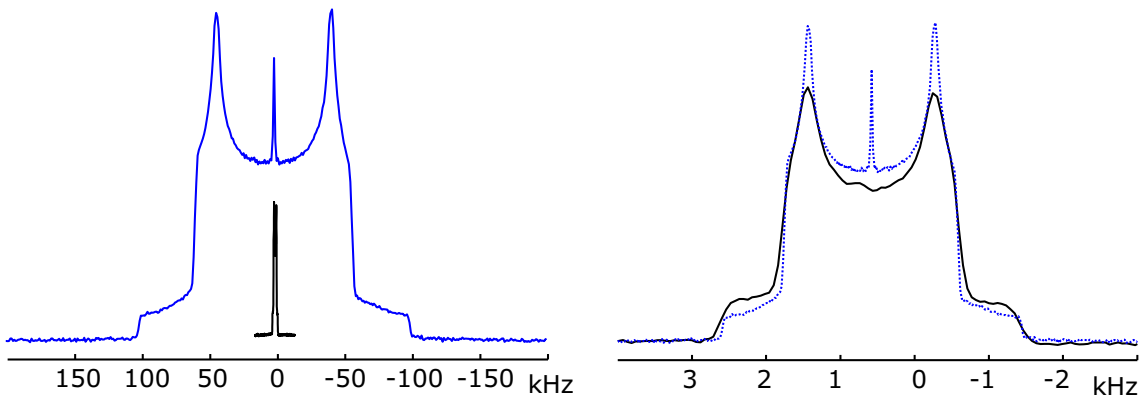

Figure 3.9: *Static ^2H NMR spectrum (blue line) of methylene-deuterated p-nitro-benzylalcohol and ^2H OMAS spectrum (black line) recorded under spinning at 29762 Hz. Both spectra are recorded at a sample temperature of 330 K. The magic-angle offset is determined by scaling the frequency axis of the static spectrum by $\frac{1}{2}(3\cos^2(\beta_M)-1)$ (dotted line) yielding a magic-angle offset of 0.78°.*

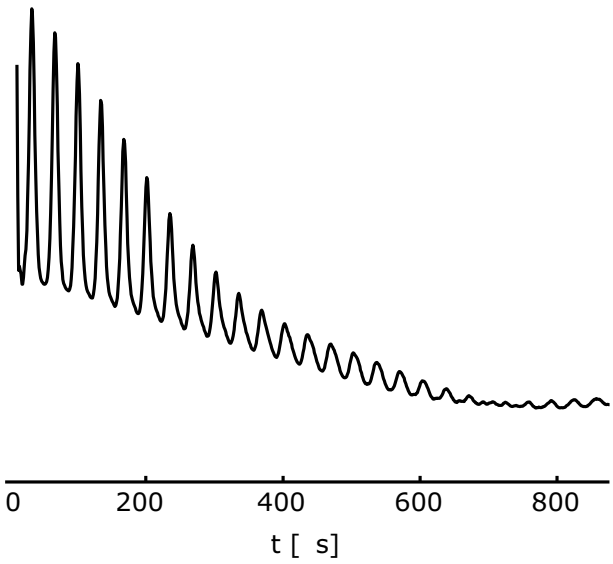

Figure 3.10: *Free induction decay of methylene-deuterated p-nitro-benzylalcohol recorded under 29762 Hz spinning at 0.78° magic-angle offset.*

observed in the two spectra are due to the finite excitation bandwidth that lowers the "shoulders" of the static spectrum.

As the quadrupole coupling parameters of NBZOH show a dependence on temperature, the static ^{2}H NMR experiment must be performed at the same sample temperature as

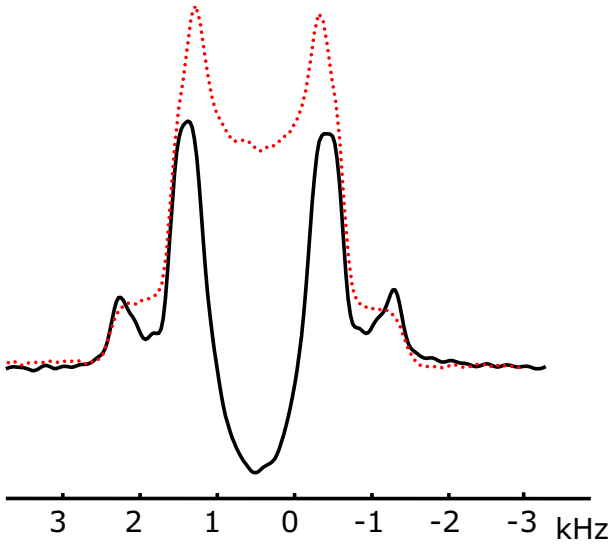

Figure 3.11: *^{2}H OMAS spectrum recorded under 29762 Hz spinning at 0.78° magic-angle offset with a misset of the dead time delay (for comparison the dotted line recorded with appropriate dead time delay is shown).*

the ^{2}H OMAS experiment, in which friction heats the sample as it is spun fast. A temperature calibration of the probe used for the presented experiments as well as the quadrupole coupling parameters of NBZOH for various sample temperatures can be found in Appendix A. It should be mentioned that heating or cooling the probe causes a change in the angle of the rotor axis. Thus, when performing temperature depended experiments, the calibration must be performed after the probe reached thermal equilibrium. To ensure that the rotor angle is not changed by the sample insertion/ejection mechanism of the probe, calibration was performed before and after the acquisition of OMAS experiments.

Fig. 3.10 shows the FID of a one-pulse experiment performed under OMAS conditions. Due to the steepness of the rotor echoes the first acquisition point and the time increment in the direct dimension (dwell time) must be set carefully to ensure that the data points are acquired precisely at the echo maxima. Due to the internal timing of the spectrometer, the dwell time cannot be set to arbitrary values, and it is therefore necessary to choose a proper spinning speed. For most experiments performed in this thesis the rotor was spun at 29762 Hz, corresponding to a dwell time of $\Delta t = \tau_R = 33.6\,\mu$s. Since the first point of the FID cannot be observed because it lies within the dead time after the read pulse, the dead time delay (the time after the pulse at which the first data point is acquired) has to be set to a multiple of a τ_R. As the spectrometer does not allow this time to be set directly, it was determined experimentally. Fig. 3.11 shows two spectra of NBZOH

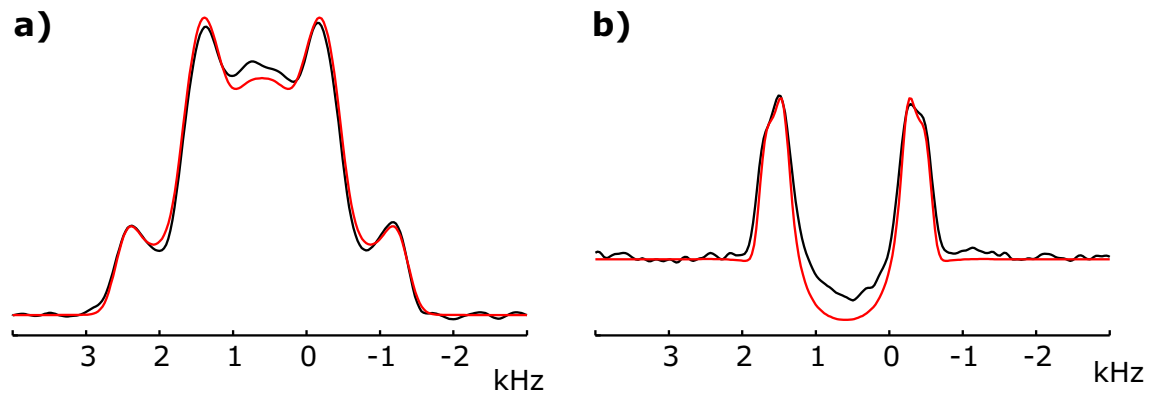

Figure 3.12: *DQ-filtered ^2H OMAS spectra with (a) $\tau = \frac{\tau_R}{2}$ and (b) $\tau = \frac{\tau_R}{4}$ recorded under 29762 Hz spinning at 0.46° angle offset (black). Calculated spectra for $\frac{\delta}{2\pi} = 101$ kHz and $\eta = 0.16$ are superimposed for comparison (red).*

recorded with different dead time delays. It is evident that misseting the dead time delay leads to severe phase distortions. However, it should be noted that, while the line shape is heavily distorted, the position of the characteristic features of the line does not change and fitting the line shape "by eye" would still yield reasonable values.

To test the applicability of the DQ-filtered experiment, a one-dimensional version was recorded on the magic angle calibration compound NBZOH at a spinning frequency of 29762 Hz using excitation/reconversion times of $\tau = \frac{\tau_R}{2}$ and $\tau = \frac{\tau_R}{4}$, respectively. The expected line shapes were then calculated using Eq. (3.6), and the quadrupole coupling parameters extracted from the static spectrum at 330 K. As shown in Fig. 3.12, the experimental spectra nicely match the calculated line shapes.

3.1.5 2D DQ OMAS Experiment

To demonstrate the capability of the two-dimensional DQ OMAS experiment to separate quasistatic line shapes of samples deuterated at multiple sites, spectra of L-histidine hydrochloride monohydrate recrystallised from D_2O were recorded, which is deuterated at four sites. Fig. 3.13 shows such a spectrum recorded with $\tau = \frac{\tau_R}{4}$ under 29762 Hz OMAS with a magic-angle offset of 0.46°. In the indirect (DQ) dimension the lines are perfectly separated according to their different chemical shifts, while in the direct (SQ) dimension DQ-filtered quasistatic line shapes are observed, from which the quadrupole coupling parameters can be extracted.

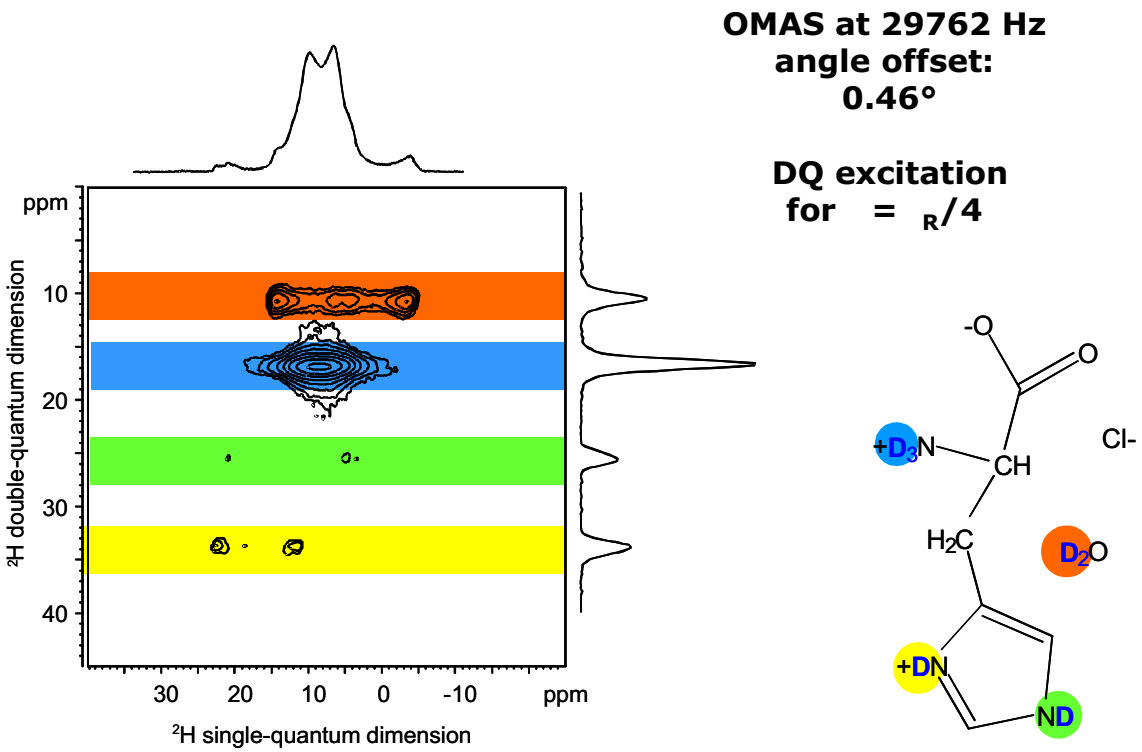

Figure 3.13: *Two-dimensional ^2H DQ OMAS spectrum of L-histidine hydrochloride monohydrate recrystallised from D_2O recorded under 29762 Hz spinning with a magic-angle offset of 0.46° using $\frac{\tau_R}{4}$ excitation/reconversion times.*

In Fig. 3.14, three spectra recorded under spinning at different magic-angle offsets are shown. Naturally, the quasistatic line shapes broaden with increasing magic-angle offset. For small magic angle offsets the lines originating from nuclei experiencing only small quadrupolar interactions (in this case ND_3) do not yet split, while for too large magic-angle offsets the lines arising from strongly coupled nuclei suffer from relaxation. In this way, the sensitivity of the experiment can be adjusted according to the demands of the material under investigation.

Finally, Fig. 3.15 and Fig. 3.16 illustrate how the DQ-filtered quasistatic line shapes are extracted separately for all ^2H resonances from the two-dimensional spectra. The spectra were recorded under 29762 Hz spinning at a magic-angle offset of 0.78°. Fig. 3.15 shows the spectrum recorded for $\frac{\tau_R}{4}$ excitation/reconversion time. All resonances exhibit DQ-filtered quasistatic line shapes with sufficient splitting and intensity to extract the quadrupole parameters. For $\tau = \frac{\tau_R}{2}$ the lines originating from the two amide positions (δ-ND and η-

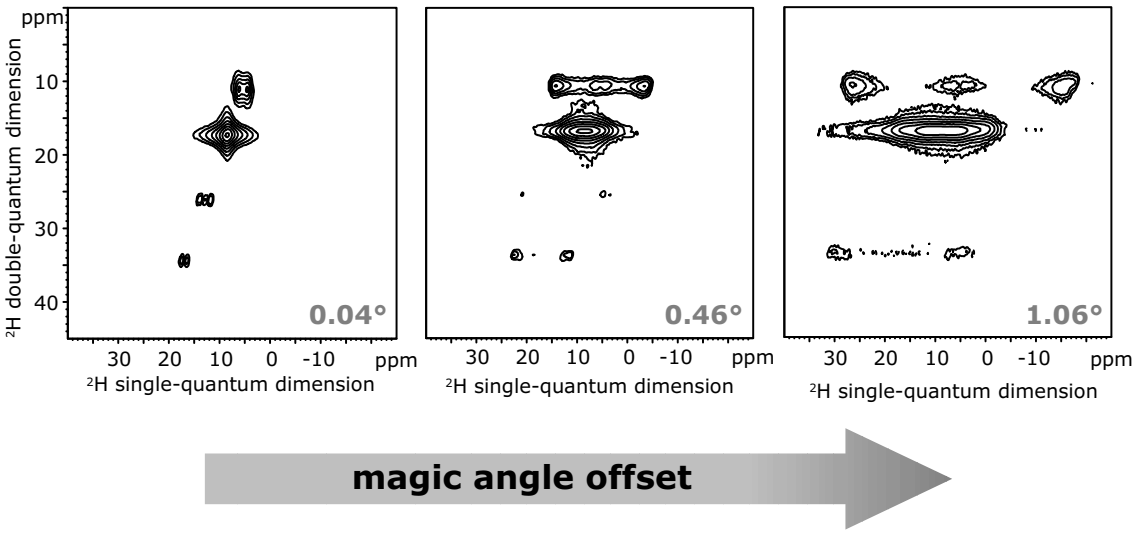

Figure 3.14: *Two-dimensional ^2H DQ OMAS spectrum of L-histidine hydrochloride monohydrate recrystallised from D_2O. The spectra were recorded under 29762 Hz spinning at increasing magic-angle offsets using $\frac{\tau_R}{4}$ excitation/reconversion times.*

ND^+) already suffer from relaxation, and the anisotropy of the ND_3 quadrupole coupling is too small to generate a splitting of the line. In both spectra, the lines exhibit phase distortions, that presumably arise from timing imperfections. The quadrupole parameters were determined by comparison with calculated line shapes (i.e. "fit by eye"). In Fig. 3.15 and 3.16, the calculated lines that were found to best fit both spectra simultaneously are plotted in red together with the extracted line shapes of the four different resonances.

The estimated errors of the parameters determined in this way are about 3 kHz for the quadrupole couplings and 0.02 for the asymmetry parameters. These errors arise from (i) the error of the "fit by eye" itself and (ii) the error of the magic-angle calibration that is about 0.02° and arises from the fit of the static spectrum to the OMAS spectrum and the temperature calibration. To improve the accuracy, the DQ-filtered quasistatic lines could be evaluated by fitting the line shapes with a simulation including timing offsets and finite pulse lengths. However, this would only yield a significantly smaller overall error when combined with a higher accuracy of the magic-angle calibration. The latter would involve a more precise temperature calibration in combination with a time domain fit of the ^2H OMAS spectrum of the calibration compound. Combined with the possibility to adjust the sensitivity of the experiment by changing excitation/reconversion time and/or the magic angle-offset, this might significantly improve the overall errors. However, as the quadrupole parameters determined on histidine are compared to values obtained by DFT

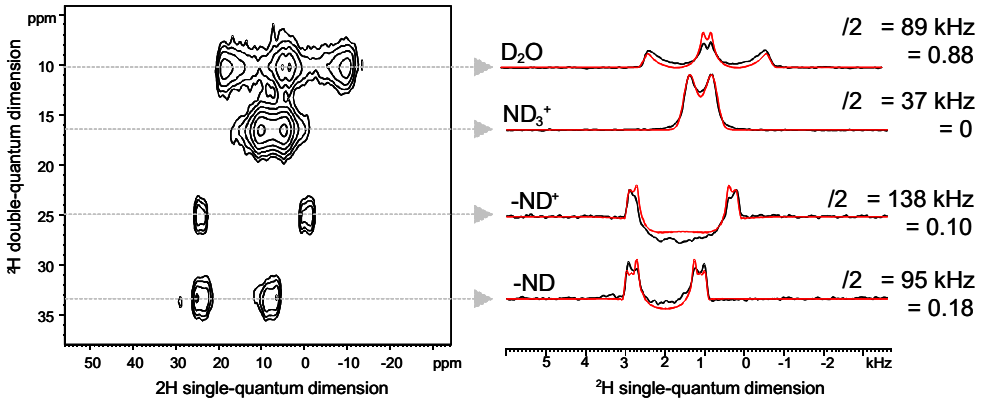

Figure 3.15: *Two-dimensional ^2H DQ OMAS spectrum of L-histidine hydrochloride monohydrate recrystallised from D_2O (29762 Hz spinning, magic-angle offset 0.71°, $\tau = \frac{\tau_R}{4}$). The individual ^2H line shapes at the four ^2H resonances are shown on the right together with calculated lines (red) for the determined quadrupole coupling parameters.*

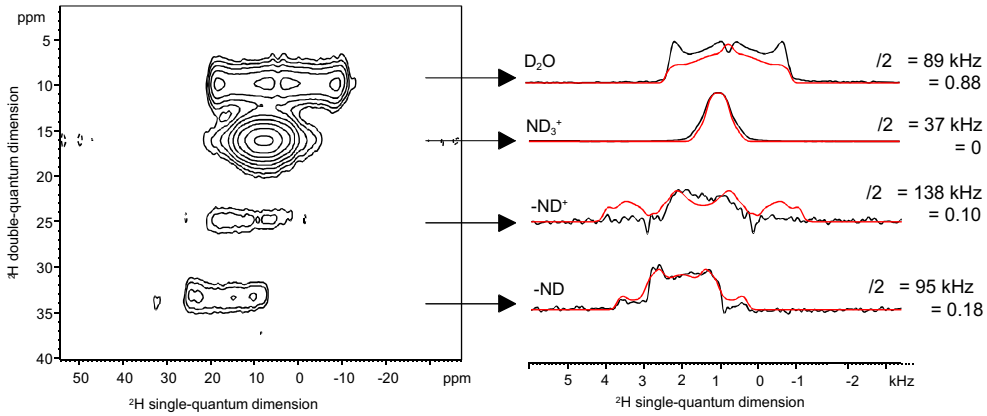

Figure 3.16: *Two-dimensional ^2H DQ OMAS spectrum of L-histidine hydrochloride monohydrate recrystallised from D_2O (29762 Hz spinning, magic-angle offset 0.71°, $\tau = \frac{\tau_R}{2}$). The individual ^2H line shapes at the four ^2H resonances are shown on the right together with calculated lines (red) for the determined quadrupole coupling parameters.*

calculations, which are not expected to have a much higher accuracy, the accuracy of the parameters as obtained by the simple "fit-by-eye" method is sufficient for this purpose.

Fig. 3.17 shows a 2D ^2H OMAS spectrum (recorded at 29762 Hz, $\tau = \frac{\tau_R}{4}$, magic-angle offset 0.75°) of fully deuterated L-histidine hydrochloride monohydrate. The lines arising from the CD and CD_2 deuterons overlap, and the quadrupole coupling parameters can therefore not be determined properly. However, the quadrupole couplings producing this

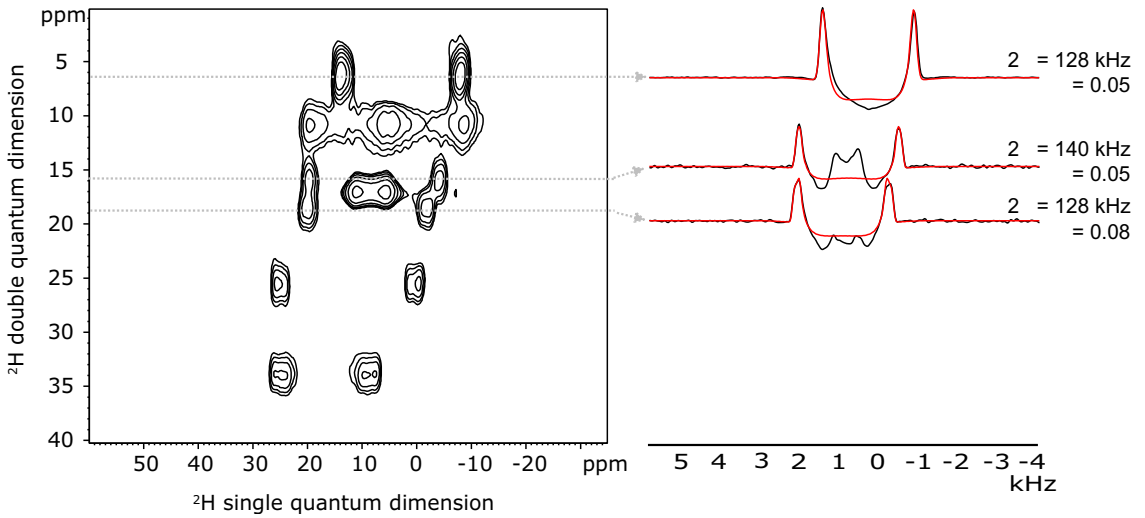

Figure 3.17: *Two dimensional ^2H DQ OMAS spectrum of fully deuterated L-histidine hydrochloride monohydrate (29762 Hz spinning, magic angle offset 0.75° , $\tau = \frac{\tau_R}{2}$) . The ^2H line shapes of the methine/methylene deuterons cannot be separated. The individual ^2H line shapes are shown on the right together with calculated lines (red) for the determined quadrupole coupling parameters.*

line shape do not seem to differ too much. A line calculated with $\frac{\delta}{2\pi} = 128$ kHz and $\eta = 0.05$ nicely matches the line. While the asymmetry parameter of the CH and CH_2 deuterons cannot be extracted from the lines, as the superposition of two lines with different quadrupole coupling parameters has almost the same effect on the line shape as a small asymmetry parameter, the anisotropy of all three deuterons clearly cannot deviate significantly from $\frac{\delta}{2\pi} = 128$ kHz. The two aromatic deuterons, though not resolved in a one dimensional spectrum due to the overlap with the ND_3 line, can be separated in the 2D DQ OMAS spectrum as, accidentally, the quadrupole couplings and, thus, the line shapes of the ND_3 and the aromatic deuterons deviate significantly, and the lines can therefore be easily decomposed.

3.1.6 Calculation of Quadrupole Coupling Parameters

Quadrupole coupling parameters in hydrogen bonds are known to sensitively depend on the geometry. Hunt and Mackay, for example, correlated the quadrupole coupling observed in ND···O hydrogen bonds with the D···O distance [Hunt 74]. In this section, the quadrupole coupling parameters of L-histidine hydrochloride monohydrate extracted

Table 3.1: *Calculated quadrupole parameters obtained from equilibrium geometry and molecular dynamics simulation and experimental values. (* the values obtained from the calculations were averaged (as described in the text) to account for the motion of D_2O, resp. ND_3.)*

		calc. 0K	calc. 300K (MD)	experimental values
δ-ND	$\frac{\delta}{2\pi}$ [kHz]	81	84	95 ($\pm$3)
	η	0.19	0.20	0.18($\pm$0.02)
ϵ-ND	$\frac{\delta}{2\pi}$ [kHz]	133	136	140($\pm$3)
	η	0.10	0.11	0.10($\pm$0.02)
aromatic-D (3)	$\frac{\delta}{2\pi}$ [kHz]	125	125	128($\pm$3)
	η	0.11	0.11	0.08($\pm$0.02)
aromatic-D (5)	$\frac{\delta}{2\pi}$ [kHz]	140	139	140($\pm$3)
	η	0.07	0.08	0.05($\pm$0.02)
ND_3	$\frac{\delta}{2\pi}$ [kHz]	37*	39*	37($\pm$3)
	η	0.00*	0.00*	0.00($\pm$0.02)
D_2O	$\frac{\delta}{2\pi}$ [kHz]	64*	71*	89($\pm$3)
	η	0.89*	0.88*	0.88($\pm$0.02)

from the 2D ^{2}H OMAS experiment are compared to computed values obtained from quantum-chemical calculations performed by Jochen Schmidt. The combination of NMR experiments with quantum-chemical calculations is of great value for structure determination and is the subject of the next chapter.

As the electric field gradient (EFG) is a ground state property, its calculation requires practically no additional computation time. This is a big advantage compared to, e.g., chemical-shift calculations, as it permits one to calculate the EFG tensor in each step of a molecular dynamics (MD) simulation in reasonable time. The calculations were performed within density functional theory (DFT) using a fully periodic description of the systems within the pseudopotential plane wave programme package CPMD [Hutter 03] (see Appendix B). In a first step, the EFG tensors were calculated for the equilibrium structure as obtained from geometry optimisation. Then, to account for temperature effects, a molecular dynamics (MD) simulation was performed, in which the system was heated to 300 K, and the EFG tensor was calculated for each step of the MD and subsequently averaged.

The computed values, as well as the experimental values, are listed in Table 3.1. The

two aromatic deuterons do not show a difference in the quadrupole coupling parameters obtained from the equilibrium structure and from the MD simulation, and agree well with the experimental parameters within the experimental errors. For the methylene and methine deuterons, the calculations yield values of $\frac{\delta}{2\pi}$ =124 kHz − 128 kHz and asymmetries of $\eta \approx 0.06$. Experimentally, the spectral resolution does not allow for a separation of these lines but, as described in the last section, the anisotropy can safely be estimated to be $\frac{\delta}{2\pi} \approx 128$ kHz.

For δ-ND and ϵ-ND, the anisotropy parameters obtained from the MD simulation at 300K are significantly larger than the ones from the equilibrium structure. This is expected, as both these deuterons are hydrogen-bonded. However, the anisotropy δ determined by the experiment is still larger, significantly so for δ-ND which exhibits a very strong hydrogen-bond. This deviation can be explained by the fact that zero-point vibrations are not accounted for in the calculations.

For water molecules embedded in crystal structures, a 180° jump motion about the molecular C_2 symmetry axis is commonly observed at room temperature. The calculated values given in Table 3.1 are averaged tensors assuming such a motion and a D-O-D angle of 104° , as found in the equilibrium structure. The asymmetry parameters obtained in this way nicely reproduce the experimental value, while the anisotropy parameter behaves similar to the ND deuterons: The value obtained from the MD simulation is larger than the one obtained from the equilibrium structure, but still lower than the experimental value. The ND_3 group rapidly rotates about its threefold symmetry axis, which renders the averaged ^{2}H quadrupole tensor symmetric. As for the crystal water, the calculated values were averaged, assuming a 3-site jump, with cone angles obtained from the equilibrium structure. However, for the ND_3 group, the calculated anisotropies do not underestimate the experimental values. This might be due to the fact that methyl-rotation increases the cone angle, leading to a decrease of the averaged anisotropy, which in turn compensates the effect of zero-point vibrations.

The above observations show that the anisotropy of the quadrupole coupling sensitively depends on the hydrogen-bond strength and can be reproduced reasonably well by calculations. However, to fully reproduce the experimental results, zero-point vibrations have to be included in the calculations. An experimental observation of temperature effects performed by heating the sample did not lead to a significant change of the quadrupole coupling parameters; however, the relative increase in temperature that can be achieved, before degradation of the sample sets in, is rather low. At low temperatures, on the other hand, OMAS experiments are technically challenging as the stability of the spinning

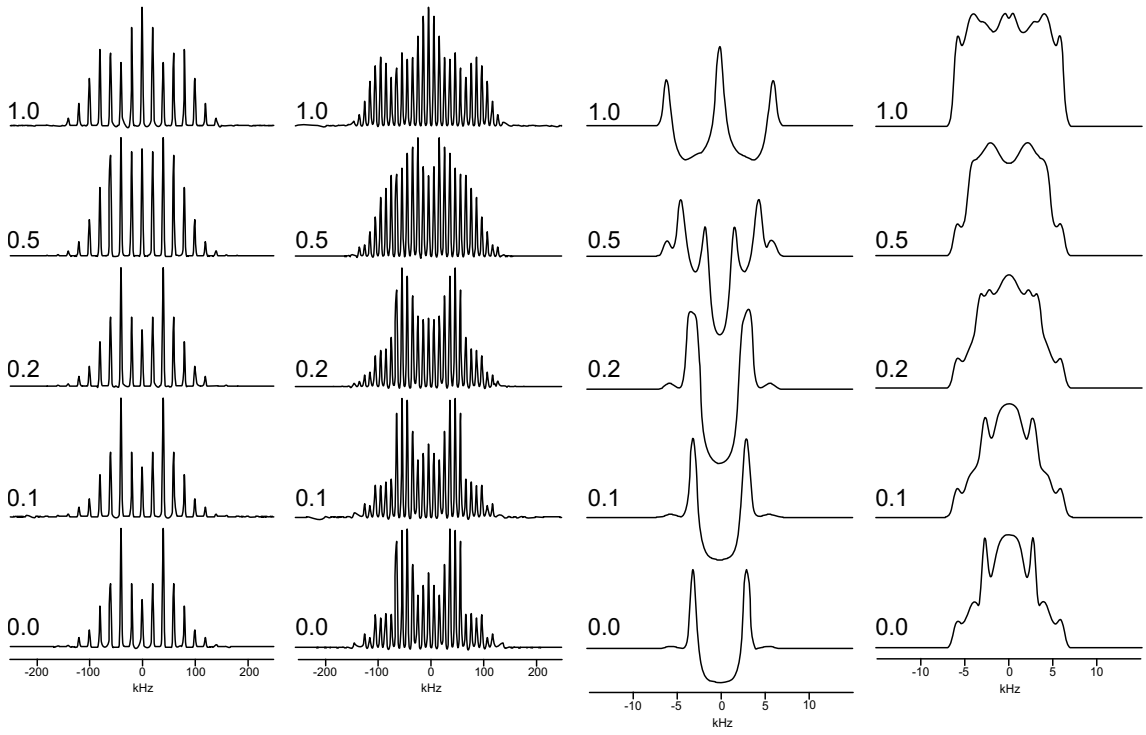

Figure 3.18: *Calculated ^2H MAS sideband patterns (left) and DQF-quasistatic ^2H line shapes (right), showing the η-sensitivity provided by the spectra. The quadrupole coupling was set to $\frac{\delta}{2\pi}$=125 kHz.*

suffers from cooling.

3.1.7 ^{2}H OMAS vs. Spinning Sidebands

As mentioned earlier, another method for determining quadrupole coupling parameters of samples deuterated at multiple sites are one-dimensional MAS sideband spectra. As these actually require less experimental effort, the advantage of the more involved 2D DQ OMAS spectra over spinning sidebands will be discussed in the following.

While sideband patterns, in principle, contain the whole information on the anisotropy and asymmetry of an interaction, it is frequently found in practice that the anisotropy δ can be extracted quite accurately from the sideband pattern, whereas the patterns are much less sensitive to the asymmetry η, in particular for asymmetries $\eta < 0.5$. In a detailed study comparing the reliability of tensor parameters as obtained from static and spinning sideband patterns [Hodgkinson 97], it was found that, for the determination of

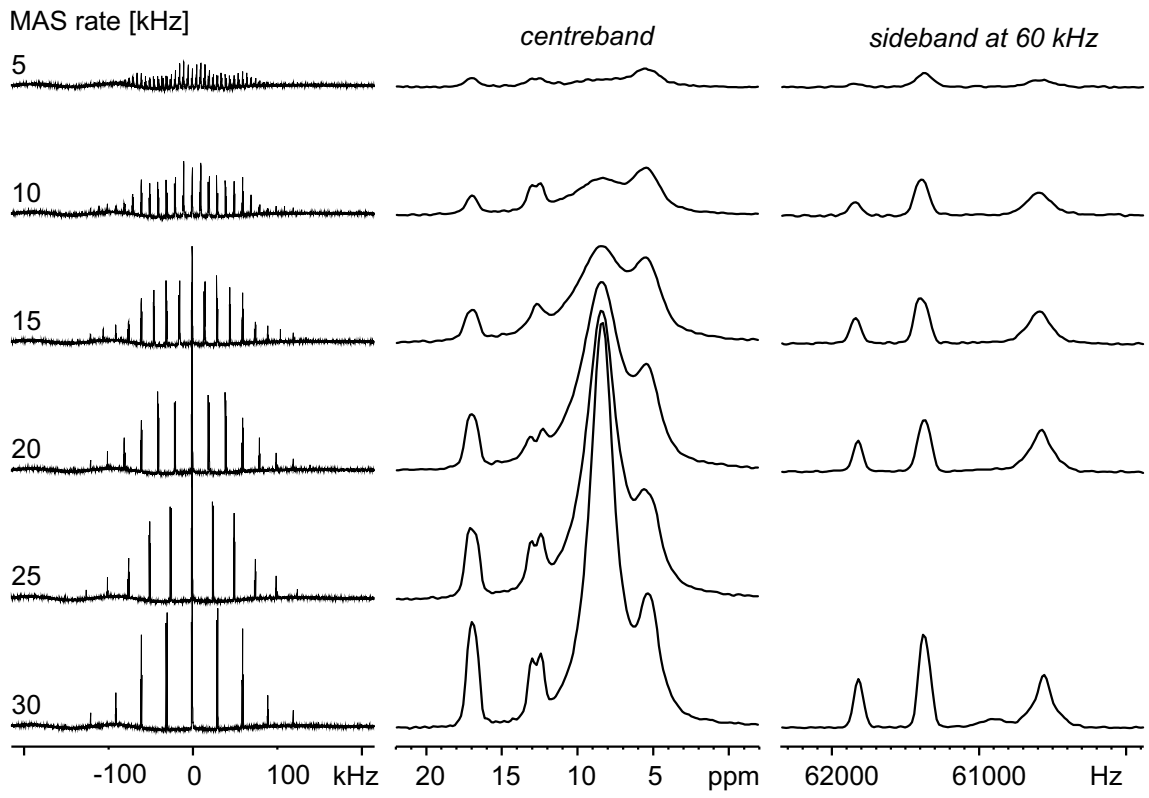

Figure 3.19: *Experimental ^2H sideband spectra of L-histidine hydrochloride monohydrate recrystallised from D_2O, recorded at different MAS frequencies.*

the quadrupolar asymmetry parameter, static spectra are always more reliable, significantly so for $\eta < 0.2$. Spinning sidebands are slightly superior for the determination of the anisotropy in the case of asymmetries $0.2 < \eta < 0.6$, but significantly less reliable in the case of $\eta < 0.2$.

This should also hold for the DQ-filtered quasistatic line shapes, as they resemble static spectra. Fig. 3.18 shows simulated spectra comparing the sensitivities of MAS sidebands and DQ-filtered quasistatic line shapes. The spectra illustrate that it is rather difficult to extract small η from spinning sideband patterns, while, as discussed above, the quasistatic line shapes can can be fitted to experimental data with an η-accuracy of 0.02. As most of the asymmetries of the observed quadrupole couplings (with the exception of the crystal water) adopt values of $\eta < 0.3$, the 2D ^{2}H OMAS experiment is preferable. In addition, it provides more degrees of freedom to adjust the experimental sensitivity.

In Fig. 3.19, experimental spinning sidebands patterns recorded under various MAS spinning frequencies are depicted. To sensitively measure the quadrupole coupling param-

eters, a high number of sidebands and, hence, a low spinning frequency is preferable. This in turn means that the signal intensity is spread over many sidebands, leading to a sensitivity problem especially for the outer, i.e. smaller, sidebands. The analysis of the nested sideband patterns is further complicated by the fact that a base-line correction has to be performed prior to the evaluation. Having said this, it should be added that the resolution of the sideband patterns does not suffer considerably from lower spinning frequencies, with the exception of a pronounced broadening of the ammonium resonance line that will be discussed in the next section.

As a last point, the example of fully deuterated L-histidine hydrochloride monohydrate is to be mentioned, where the aromatic ^{2}H resonances that are not resolved in the one-dimensional experiment are clearly separated in the 2D ^{2}H OMAS experiment due to their largely deviating quadrupole coupling parameters. This is, of course, a coincidence, but still an extraction of these parameters from spinning sidebands is not possible.

3.1.8 Motional Recoupling of the Quadrupole Interaction in the ND_3 group

As mentioned in the last section, the ND_3 resonance line in the one-dimensional ^{2}H NMR spectrum is significantly broader than the lines arising from all other deuterons. In the DQ spectrum (i.e. the skyline-projection of the indirect dimension of a 2D DQ experiment) this effect is not observed, suggesting that the broadening is caused by the quadrupole interaction, since this would not affect the DQ spectrum. Line broadening in satellite transitions of quadrupolar nuclei has been observed by Stephen Wimperis et al. [Ashbrook 02] and was explained by motional recoupling of the quadrupole interaction due to molecular motion.

The origin of motional broadening under MAS are reorientation induced frequency changes during a rotor period (i.e. changes in the resonance frequency due to a reorientation of the molecule), which interfere with the formation of the echo at the end of the rotor period. As a result the amplitude of the echo is reduced and a decay of the echo maxima is observed with time, which means an increased linewidth in the spectrum. Thus, the line broadening of the ammonium resonance observed in L-histidine hydrochloride monohydrate might be caused by the rotation of the group. In this case, the width of the line should show a dependence on temperature. In Fig. 3.21 a, ^{2}H NMR spectra recorded under 15 kHz MAS are shown for three different sample temperatures. For lower tem-

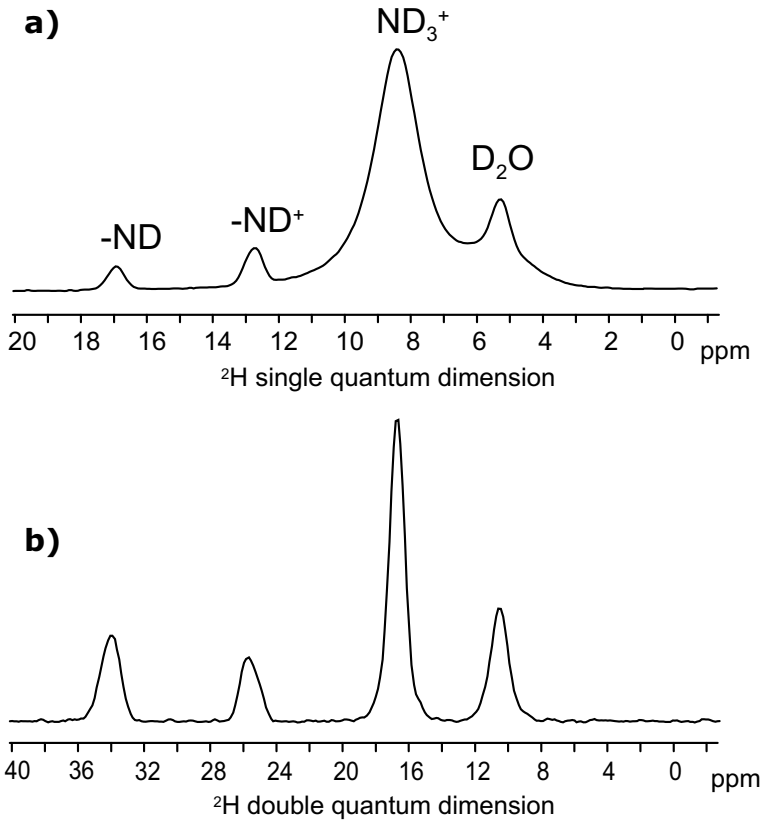

Figure 3.20: *^2H MAS NMR spectrum of L-histidine hydrochloride monohydrate recrystallised from D_2O (a) and projection of the DQ dimension of a 2D ^2H DQ OMAS spectrum (b).*

peratures, the width of the ND_3 line increases significantly, and at a sample temperature of 355 K the line is broadened to such an extent that it can hardly be observed.

The broadening of the line depends on three parameters, namely the MAS spinning frequency ν_R, the jump rate k of the molecular motion, and the change in quadrupolar frequency expected for different positions $\Delta\nu$. In the case of the ND_3 rotation, the jump rate by far exceeds the two other frequencies, as it usually is found to be of the order of GHz. From [Ashbrook 02] it is known that, in the limit of $k >> |\Delta\nu|$, the linewidth R is related to the jump rate k by the following equation:

$$R \sim \frac{(\Delta\nu\ )^2}{k}. \tag{3.7}$$

As the activation energy E_a is related to the jump rate by

$$k \sim e^{\frac{E_a}{kT}} \tag{3.8}$$

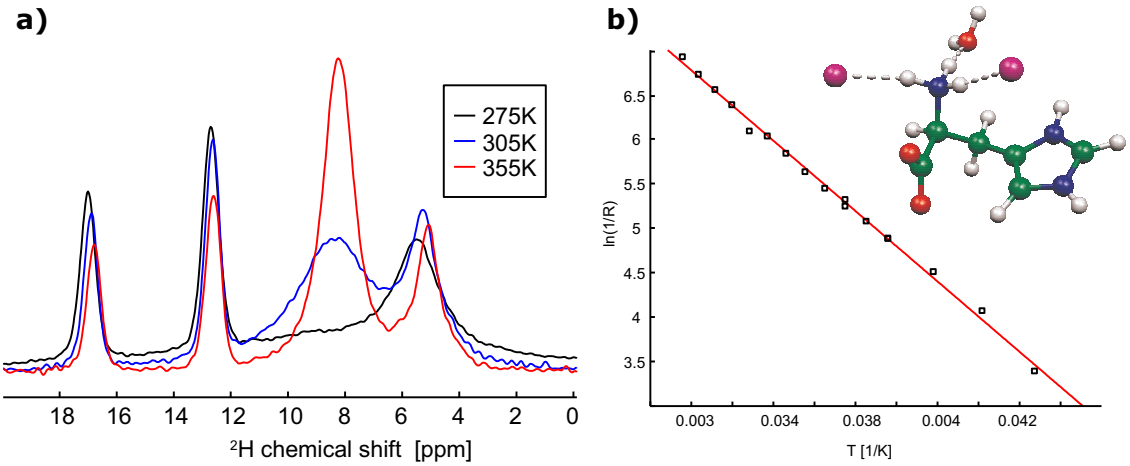

Figure 3.21: *(a) ^2H MAS NMR spectra of L-histidine hydrochloride monohydrate recrystallised from D_2O recorded at different sample temperatures. (b) Arrhenius plot of the jump rate versus temperature.*

it can be extracted from the slope of an Arrhenius plot of $\log(\frac{1}{R})$ versus $\frac{1}{T}$. (Fig. 3.21 b). The obtained value of $E_a \approx 30$ kJ/mol seems reasonable, since in the crystal all three deuterons of the ND_3 group exhibit hydrogen bonds which hinder the rotation.

The line broadening observed for decreasing MAS frequencies described in the last section can be explained by the different sample temperatures for different spinning speeds, caused by frictional heat. Spectra recorded under 30 kHz and 15 kHz MAS at the same sample temperature (Fig. 3.22) exhibit similar line widths of the ND_3 resonance. This indicates that the dipole-dipole couplings experienced by the deuterons in L-histidine hydrochloride monohydrate are small enough to be sufficiently averaged already under 15 kHz MAS.

3.1.9 Alkylamines

Finally, the application of the 2D DQ OMAS experiment will be demonstrated on alkylammonium chlorides. These systems are known to exhibit a variety of layered phases and can serve as a model for studying the internal dynamics and transitions in cell membranes. The phase transitions are accompanied by changes in the chain order and dynamics. A previous study on n-decyl-ammonium chloride [Jurga 91] revealed that these structural and dynamical changes are monitored by the ^2H quadrupole coupling parameters. In this study, three samples of n-decyl-ammonium chloride deuterated at chain positions 1

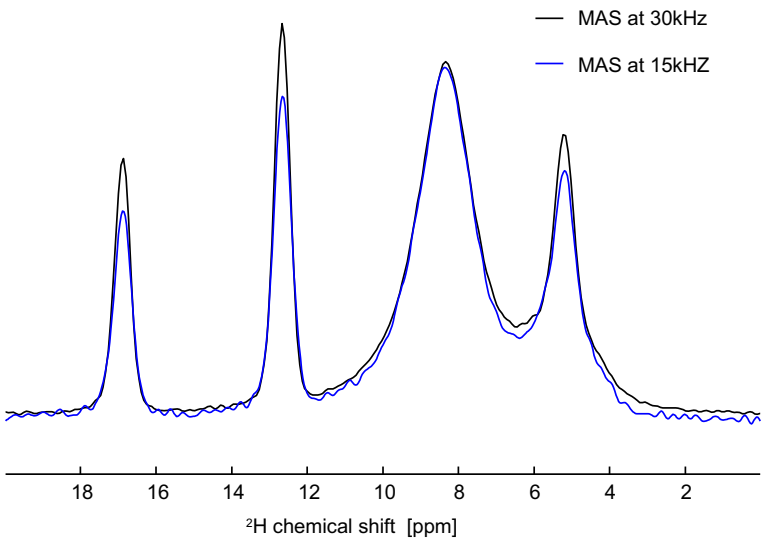

Figure 3.22: *^{2}H NMR spectra of L-histidine hydrochloride monohydrate recrystallised from D_2O under 30 kHz and 15 kHz MAS, both recorded at a sample temperature of 330K.*

and 6 and in the ammonium group, respectively, were used and the quadrupole coupling parameters were extracted from static ^{2}H line shapes. As the system sensitively depends on temperature, special care has to be taken to perform the experiments on all three samples at precisely the same temperature in order to obtain a complete picture of the phase behaviour. This is a problem commonly found when working, for example, with polymers whose structure is considerably affected by the thermal history. In such cases, it can be quite cumbersome to ensure reproducibility of temperature dependent experiments.

At this point, the advantage of the 2D ^{2}H DQ OMAS experiment becomes obvious. It allows quadrupole coupling parameters of samples deuterated at multiple sites to be measured in a single experiment and, in this way, ensures that the quadrupole coupling parameters of deuterons at all positions in the molecule are measured under exactly the same conditions. To demonstrate this, a mixture of three alkylamines deuterated at different chain positions was investigated, namely CH_3-$(CH_2)_4$-CD_2-$(CH_2)_5$-NH_3Cl, CH_3-$(CH_2)_7$-CD_2-NH_3Cl and CH_3-$(CH_2)_{10}$-ND_3Cl. (This mixture was chosen for convenience, as the samples already existed and the main intention of the experiments was to test the capability of the 2D ^{2}H OMAS experiment to determine the quadrupole coupling parameters of the different deuterated sites in these systems. The same experiment would, of course, be also applicable to a sample consisting of a single compound deuterated at multiple sites.)

Fig. 3.23 shows a 2D ^{2}H OMAS spectrum of this mixed sample recorded with $\tau = \frac{\tau_R}{4}$ (29762 Hz spinning, MA offset 0.82°) at a sample temperature of 330 K. The signals of all three positions are clearly separated in the double-quantum dimension. The resonances originating from the deuterons in the methylene groups positioned in the middle of the chain and next to the NH_3-group are found in the double-quantum dimension at 2.9 ppm and 7.5 ppm, respectively (corresponding to 1.45 ppm and 3.75 ppm in the single-quantum dimension). The extracted DQ-filtered quasi-static line shapes, together with the calculated best-fit line shapes, are shown on the right of Fig. 3.23. For both methylene groups an anisotropy of $\frac{\delta}{2\pi} = 86$ kHz was extracted from the line shapes, which is significantly smaller than the anisotropy expected for a immobile methylene group $\frac{\delta}{2\pi} \approx 120$ kHz. In addition, the rather large observed asymmetry parameters ($\eta = 0.53$ and $\eta = 0.35$) imply a motion of the hydrocarbon chains. Asymmetries in this range can be explained by an unequally populated four-site jump, as it was found in [Jurga 91]. The ammonium group, in contrast, rotates rapidly and uniformly about its C_3-axis. This renders the quadrupole coupling tensor symmetric and leads to a reduction of the anisotropy by a factor of about $\frac{1}{3}$, which, as expected, is in the range of $\frac{\delta}{2\pi} \approx 40$ kHz. From this it can be concluded that the C-N bond is rigid at this temperature. When heating the sample to 350 K (Fig. 3.24), the quadrupole coupling of the ammonium group further decreases to $\frac{\delta}{2\pi} = 35$ kHz and the tensor now becomes asymmetric. This means that, in addition to the fast rotation of the ND_3 group, the C-N bond undergoes reorientational motions. The tensor of the deuterons at C-1 position is found to be symmetric at higher temperatures with $\frac{\delta}{2\pi} = 77$ kHz, indicating a symmetric motion of this position (e.g., an equally populated four-site jump). The quadrupole coupling tensor of the deuterons in the middle of the chain only changes few with increasing temperature.

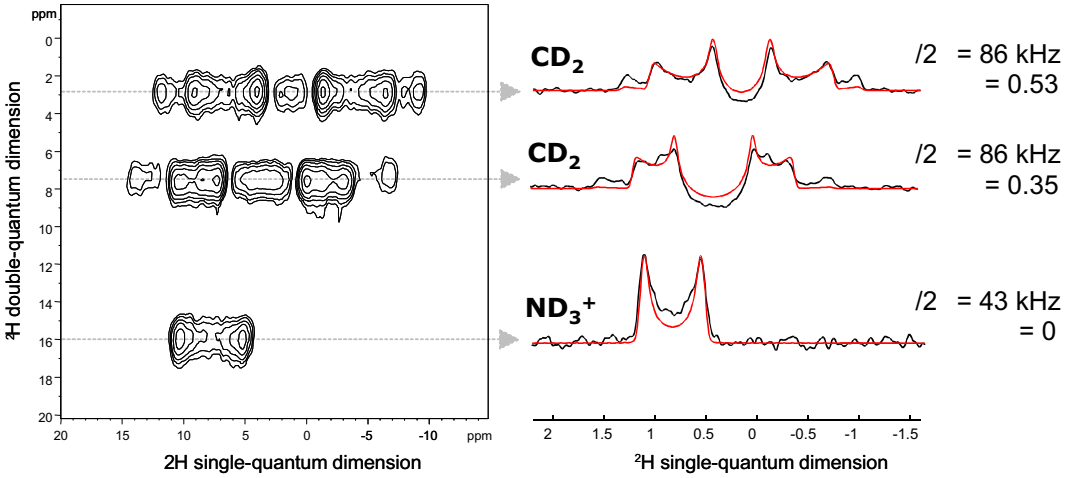

Figure 3.23: *Two dimensional ^2H DQ OMAS spectrum of a mixture of alkylamines deuterated at three positions recorded at a sample temperature of 330 K (29762 Hz spinning, magic angle offset 0.82° , $\tau = \frac{\tau_R}{4}$). The individual ^2H line shapes at the three ^2H resonances are shown on the right together with calculated lines (red) for the determined quadrupole coupling parameters.*

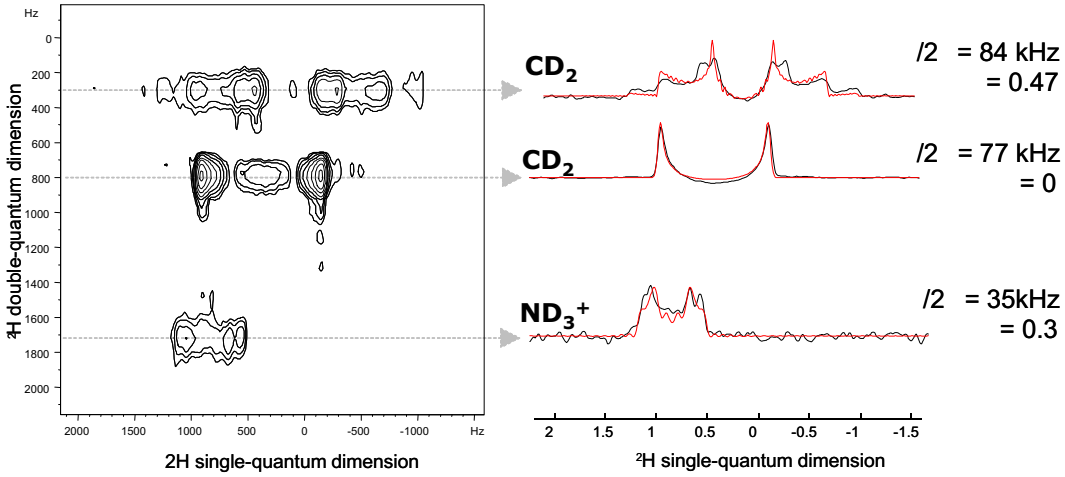

Figure 3.24: *Two dimensional ^2H DQ OMAS spectrum of a mixture of alkylamines deuterated at different positions recorded at a sample temperature of 350 K (29762 Hz spinning, magic angle offset 0.82° , $\tau = \frac{\tau_R}{4}$). The individual ^2H line shapes at the three ^2H resonances are shown on the right together with calculated lines (red) for the determined quadrupole coupling parameters.*

3.2 ^{7}Li NMR

Lithium ions are frequently used as a charge carriers in ion conductors and rechargeable lithium ion batteries. The number, location and mobility of the Li ions in these materials determine the performance of the device, yet standard structural techniques such as X-ray often cannot provide information, since the materials contain considerable disorder and lithium has a small scattering cross section. Solid-state NMR, in turn, provides information on local order and is therefore well suited for investigating nanocrystalline or amorphous systems.

There are two NMR-active Lithium isotopes that both possess a quadrupolar moment. ^{6}Li is a spin-1 nucleus with a rather small quadrupole moment of $Q = -8 \cdot 10^{-32}$ m^2, while ^{7}Li is a spin-$\frac{3}{2}$ nucleus with $Q = -4 \cdot 10^{-30}$ m^2. As a consequence, for many applications ^{6}Li has the more favourable NMR properties and can be treated similar to ^{2}H . On the other hand, ^{6}Li has only 7.5% natural abundance and a lower gyromagnetic ratio than ^{7}Li . Hence, the sensitivity of ^{7}Li is about a factor of 400 higher than that of ^{6}Li. Additionally the low natural abundance of ^{6}Li means a major drawback not only with respect to S/N issues, but also, when homonuclear dipole-dipole couplings are to be investigated, as the probability of finding neighbouring ^{6}Li nuclei is low. The knowledge of the quadrupole coupling parameters of lithium nuclei in solids allows the determination of the local symmetry of the crystallographic site. Again, working with ^{7}Li is favourable as its higher quadrupolar moment renders it more sensitive to its electronic environment. ^{7}Li NMR under static and MAS conditions has successfully been used to investigate the mobility and the geometry of the electronic environment of lithium ions in solids [Wagemaker 01].

In the following, ^{7}Li NMR experiments will be presented that were carried out on lithium intercalated in TiO_2. This material has been subject to a large number of studies [Koudriachowa 02, Koudriachowa 03, Wagemaker 01] due to its possible application in solar cells, electrochemic devices and rechargeable lithium ion batteries. The samples were prepared by Muhammad Nawaz Tahir (University of Mainz), by intercalating butyl-lithium into TiO_2 nanotubes with 0.4-0.5 equivalents lithium. In X-ray investigations of this material very broad weak reflexes were observed indicating that the material is not crystalline. For comparison, lithium was intercalated in TiO_2 anatase and TiO_2 rutile, prepared by tempering the material before intercalation. However, in the NMR experiments no difference was observed between samples prepared from TiO_2 anatase and TiO_2 rutile. As the EFG tensor sensitively depends on the local geometry, it is highly

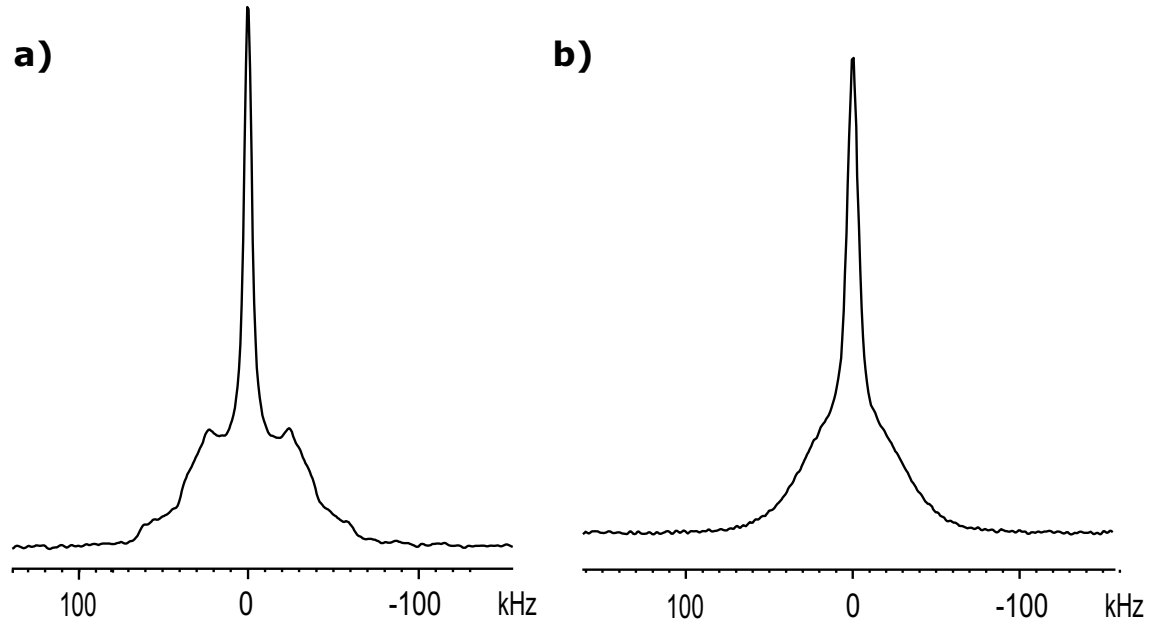

Figure 3.25: *Static ^7Li NMR spectra of Li_xTiO_2-1 (a) and Li_xTiO_2-2 (b).*

impropable that two different structures give rise to exactly the same quadrupole interaction tensors. From literature [Wagemaker 01] it is known that, for insertion ratios of lithium in TiO_2 anatase larger than $x = 0.05$, the structure changes from anatase to lithium titanate and two phases are observed, namely lithium titanate and lithium in anatase. For insertion ratios in the range of $x = 0.5$, as in the materials investigated here, more than 90% of the material is lithium titanate. This structural change has also been observed for intercalation of lithium in TiO_2 rutile, and might thus provide an explanation for the similarity of the NMR spectra recorded on samples prepared from TiO_2 anatase and TiO_2 rutile. In the following ^{7}Li NMR experiments of the crystalline samples will be presented, which are then applied to the amorphous samples.

3.2.1 Static ^{7}Li NMR

Fig. 3.25 displays the static ^{7}Li NMR spectra of two Li_xTiO_2 samples (referred to as Li_xTiO_2-1 and Li_xTiO_2-2). The line obtained from Li_xTiO_2-1 shows the typical features of a spin-$\frac{3}{2}$ static line shape. The narrow peak arises from the central transition $+\frac{1}{2} \leftrightarrow -\frac{1}{2}$ that is not affected by the quadrupolar interaction, while the broad line arises from the satelite transitions $\pm\frac{1}{2} \leftrightarrow \pm\frac{3}{2}$. The width of the spectrum is equivalent to the quadrupolar coupling constant $C_q = \frac{e^2qQ}{h}$, which is approximately 130 kHz. Static quadrupolar line

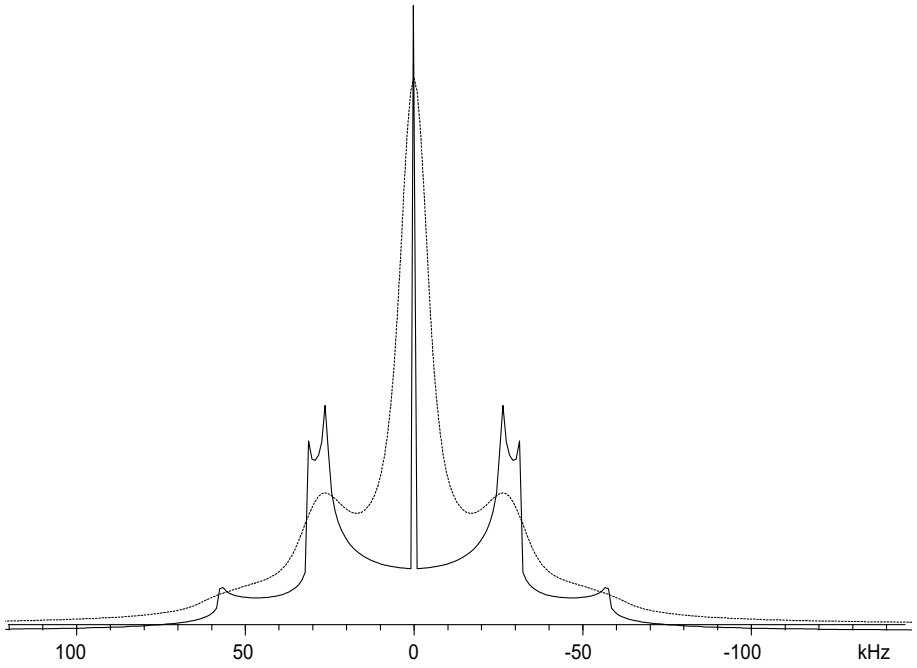

Figure 3.26: *Simulated static ^{7}Li NMR line shapes with C_q=128 kHz and η=0.2, with (dotted line) and without (solid line) additional line broadening.*

shapes were simulated with the simulation software SIMPSON [Bak 00] (see Fig. 3.26). By comparing simulated and experimental spectra, a quadrupolar coupling constant of C_q =128 kHz and an asymmetry $\eta \approx 0.2$ is obtained for Li_xTiO_2-1. The observation of a line shape governed by a single set of parameters δ, η indicates a well defined position of the lithium ions in the sample.

The asymmetry of the quadrupole coupling tensor supports the assumption that the intercalation leads to a structural change of the anatase structure. In the middle of an octahedral site in anatase, lithium would have four neighbouring oxygens in the a-b-plane at 1.93 Å distance and two in the c-direction at 2.78 Å distance which, in a first estimation, would lead to a symmetric quadrupole coupling tensor. For lithium in lithium titanate, in contrast, two neighbouring oxygens at 1.97 Å distance and two at 2.04 Å distance are found in the a-b plane and in the c-direction one at 2.17 Å distance and one at 2.8 Å distance, leading to an asymmetric electronic environment for the lithium ions. In [Wagemaker 01] an estimate for the quadrupole coupling constant in lithium titanate based on the six nearest neighbour atoms was calculated to be $C_q \approx 160$ kHz, while for lithium in the centre of the anatase octahedral site $C_q \approx 300$ kHz is expected.

The longitudinal relaxation time T_1 of the samples was found to be in the order of

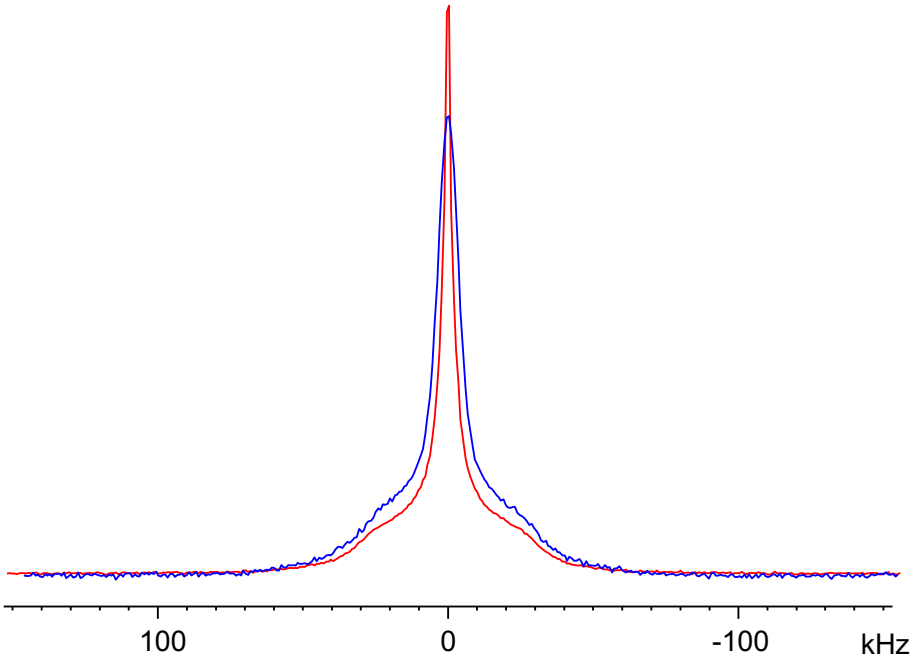

Figure 3.27: *Static ^{7}Li NMR spectra of Li_xTiO_2-2 recorded at sample temperatures of 149 K (blue line) and 398 K (red line).*

seconds. From this, it can be concluded that no paramagnetic ions are present in the sample as they would lower T_1 significantly; even for low concentration of paramagnetic ions, T_1 can become as low as 10^{-4} s. Upon $Li^+ + e^-$ insertion in TiO_2 (being a large gap semiconductor with a band gap of $\approx$ 3 eV) the electron may become localised on Ti or may be inserted in a conduction band. While Ti^{4+} is nonmagnetic, Ti^{3+} has a paramagnetic moment. The observed T_1 relaxation constants clearly show the absence of paramagnetic Ti^{3+} ions in the sample.

Compared to the simulations, the experimental spectrum is significantly broadened. This is even more drastic in the case of the static line shape of Li_xTiO_2-2, which has the same width as the Li_xTiO_2-1 line, but the additional broadening renders the line almost featureless. In general, additional line broadening can either be caused, in a "homogeneous" fashion, by dipole-dipole interactions of the observed nuclei with neighbouring nuclei, or it can, in an "inhomogeneous" fashion, be due to the presence of distorted crystals with various and slightly different electronic environments. Static ^{7}Li NMR spectra of Li_xTiO_2-2 recorded at different sample temperatures (see Fig. 3.27) showed a increase of the linewidth with decreasing temperature. This suggests that the line broadening is caused by dipole-dipole interactions, as they are reduced by lithium diffusion, which is

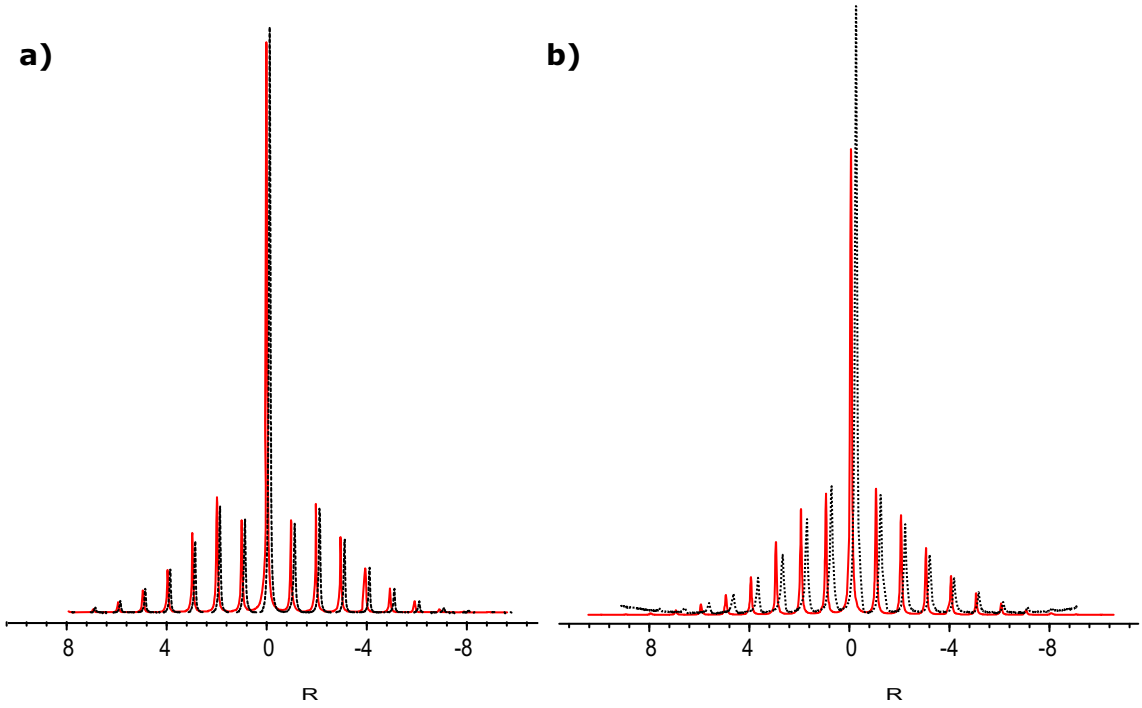

Figure 3.28: ^{7}*Li MAS NMR sideband patterns recorded under 10 kHz MAS of* Li_xTiO_2*-1 (a) and* Li_xTiO_2*-2 (b). The simulated sideband patterns with* C_q*=128 kHz and* η*=0.2 are shown in red for additional dipole-dipole couplings of* $\frac{D_{ij}}{2\pi}$*=2 kHz (a) and* $\frac{D_{ij}}{2\pi}$*=4 kHz (b).*

expected to be faster at higher temperatures. The presence of dipole-dipole interactions implies, that the Li hopping rates are not fast compared to the dipolar interaction as, otherwise, the dipole-dipole coupling would be averaged to zero. A quantitative determination of dipole-dipole coupling strengths from static line shapes is not possible as additional inhomogeneous line broadening arising from variously distorted crystals cannot be excluded. Therefore, ^{7}Li MAS NMR experiments were carried out, which will be discussed in the following.

3.2.2 ^{7}Li Spinning Sidebands

For both samples the sideband spectra recorded under 10 kHz MAS (see Fig. 3.28) have the same overall width, but show a significant difference of the first-order sidebands. From simulated spectra, it becomes clear that additional dipole-dipole couplings mainly affect the first-order sidebands. In Fig. 3.28, the simulated spectra are shown in red, using the same quadrupole parameters of $C_q = 128$ kHz and $\eta = 0.2$, but different additional dipole-

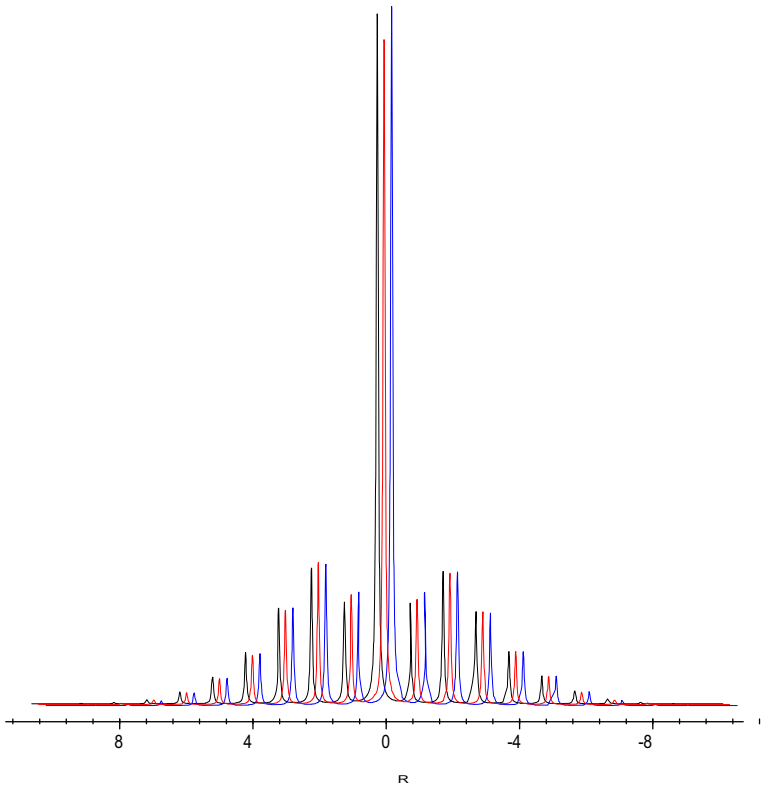

Figure 3.29: *Simulated ^7Li NMR sideband patterns with C_q = 128 kHz and η = 0.2, of two ^7Li nuclei with $\frac{D_{ij}}{2\pi}$ = 1 kHz (black line) and $\frac{D_{ij}}{2\pi}$ = 2 kHz (blue line) as well as a three spin system in which the observed nucleus is coupled to two other ^7Li nuclei with $\frac{D_{ij}}{2\pi}$ = 1.5 kHz (red line).*

dipole couplings. For both samples, the simulated lines agree well with the experimental patterns, with the exception of a difference in the intensities of the central line which will be discussed later. For Li_xTiO_2-1 and Li_xTiO_2-2 dipole-dipole coupling constants of $\frac{D_{ij}}{2\pi} = 2$ kHz and $\frac{D_{ij}}{2\pi} = 4$ kHz, respectively, were extracted.

The dipole-dipole interaction experienced by lithium in Li_xTiO_2 is dominated by homonuclear type of couplings, as the natural abundance of the NMR-active titanium nuclei ^{47}Ti and ^{49}Ti is only 13% in total and their gyromagnetic ratios are about one order of magnitude smaller than that of ^{7}Li; the natural abundance of NMR-active oxygen ^{17}O is below 0.04%. The shortest Li-Li distance in lithium titanate is about 2.5 Å and would lead to a dipole-dipole coupling strength of $\frac{D_{ij}}{2\pi} = 1.25$ kHz. However, in the crystal, lithium nuclei experience dipole-dipole interactions of several neighbouring ^{7}Li nuclei. Fig. 3.29 shows simulated sideband patterns for two spins with dipole-dipole couplings of $\frac{D_{ij}}{2\pi} = 1$ kHz and

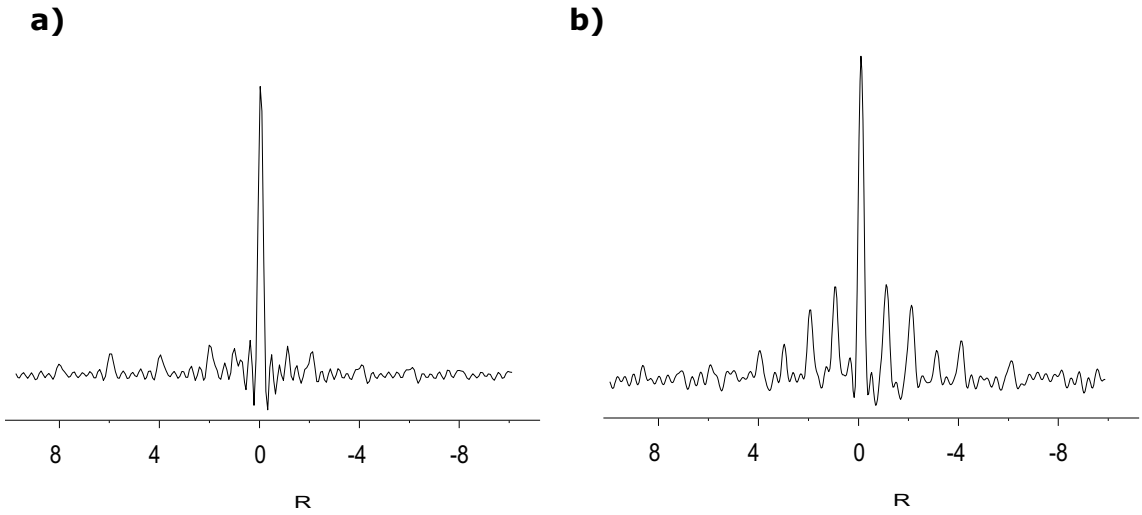

Figure 3.30: *Experimental ^7Li TQ sideband pattern of Li_xTiO_2-1 (a) and Li_xTiO_2-2 (b) recorded under 10 kHz MAS with excitation/reconversion times of $\tau = \frac{\tau_R}{2}$.*

$\frac{D_{ij}}{2\pi} = 2$ kHz, as well as a simulation of a three spin system in which the observed nucleus is coupled to two other ^{7}Li nuclei with $\frac{D_{ij}}{2\pi} = 1.5$ kHz. From this, it is obvious that the effect of many weakly coupled spins on the pattern is similar to the effect of one strongly coupled spin, because additional couplings mainly affect the first order sidebands. The only noticeable difference is a slight decrease of the central line. This deviation has also been found when comparing the experimental sideband patterns with the simulated spectra, significantly so for Li_xTiO_2-2, indicating that the larger dipole-dipole coupling is caused by a sum of weaker couplings. Hence, the observed difference in the dipole-dipole coupling constants of the two samples may be due to different lithium contents in the sample. However, the observed difference in the central line could as well arise from a second species of Li ions in the sample with a very small quadrupole coupling. This is a general problem of the determination of dipole-dipole couplings from SQ sideband patterns: For samples containing more than one species or a distribution of quadrupole couplings, it is often not possible to distinguish wether effects on sidebands arise from different quadrupole couplings of different lithium species, or from dipole-dipole couplings to other nuclei.

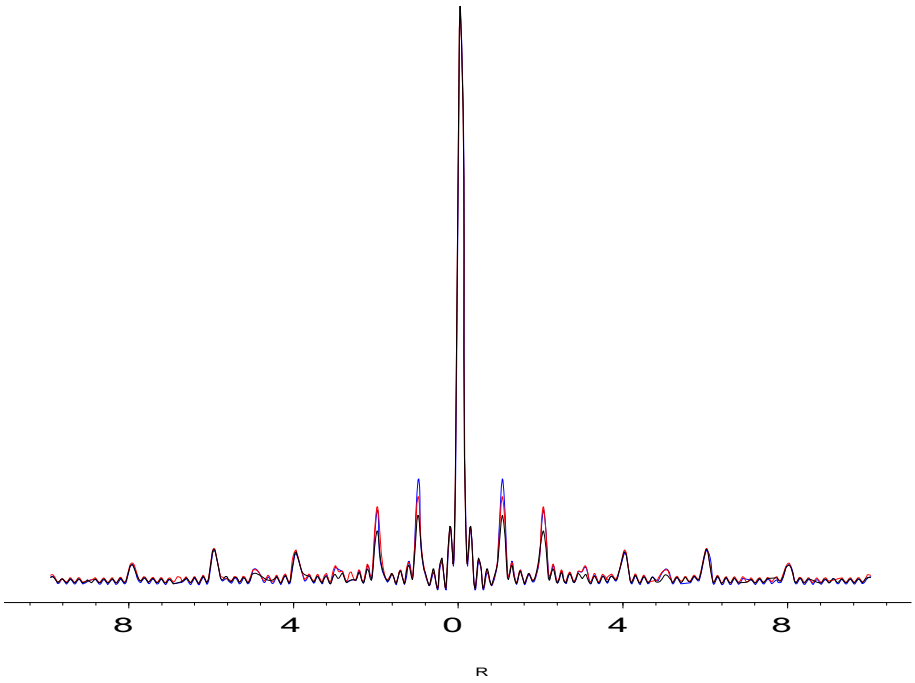

Figure 3.31: *Simulated ^{7}Li TQ NMR sideband patterns with C_q = 128 kHz and η = 0.2, of two ^{7}Li nuclei with $\frac{D_{ij}}{2\pi}$ = 1 kHz (black line) and $\frac{D_{ij}}{2\pi}$ = 2 kHz (blue line) as well as a three spin system in which the observed nucleus is coupled to two other ^{7}Li nuclei with $\frac{D_{ij}}{2\pi}$ = 1.5 kHz (red line).*

3.2.3 ^{7}Li MQ MAS NMR

As ^{7}Li is a spin-$\frac{3}{2}$ nucleus, it can form triple-quantum (TQ) coherences. The evolution of such TQ coherences can be monitored in the indirect dimension of a two-dimensional TQ NMR experiment. A rotor-encoded version of the TQ five pulse experiment was performed under 10 kHz MAS using excitation/reconversion periods of $\tau = \frac{\tau_R}{2}$. From these, TQ sideband patterns were obtained, after Fourier transformation in both dimensions and summation over the observed line in the direct dimension (see Fig. 3.30).

The advantage of the TQ sideband patterns over the SQ data becomes apparent in the simulated patterns shown in Fig. 3.32. In absence of additional dipole-dipole couplings, only even-order sidebands are observed. The inclusion of dipole-dipole couplings in the simulation gives rise to odd-order sidebands and also affects, to a lesser extent, the even-order sidebands. The effect of additional dipole-dipole couplings on the TQ sideband patterns is much more pronounced than for SQ patterns because, effectively, the homonuclear ^{7}Li -^{7}Li couplings are amplified, i.e. scaled, by the coherence order [Friedrich 98].

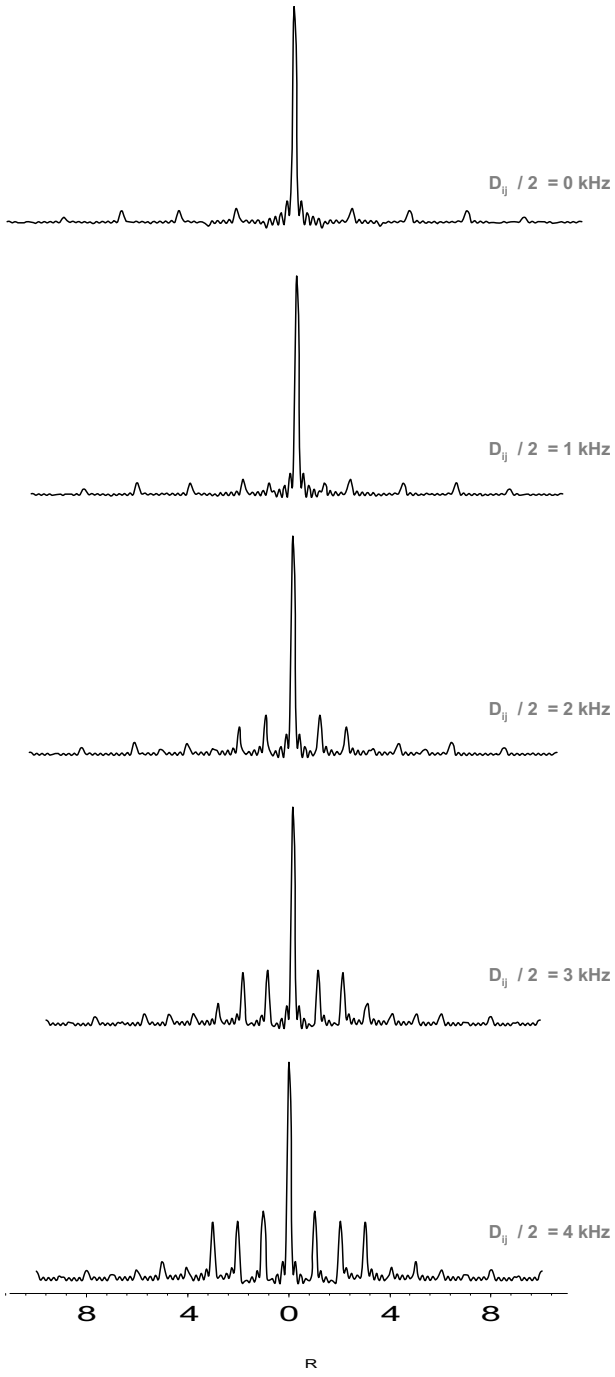

Figure 3.32: *Simulated ^7Li TQ NMR sideband patterns with C_q = 128 kHz and η = 0.2. Without additional dipole-dipole coupling (top) and with additional dipole-dipole couplings of (top to bottom) $\frac{D_{ij}}{2\pi}$ = 1 kHz, $\frac{D_{ij}}{2\pi}$ = 2 kHz,$\frac{D_{ij}}{2\pi}$ = 3 kHz and $\frac{D_{ij}}{2\pi}$ = 4 kHz.*

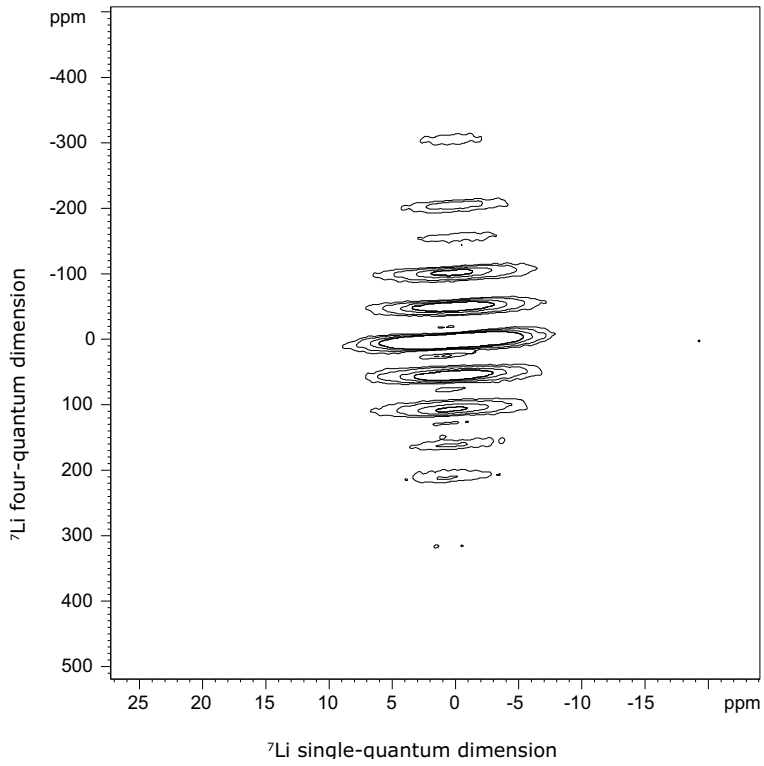

Figure 3.33: *Two dimensional ^{7}Li 4Q spectrum of Li_xTiO_2-2 recorded under 10 kHz MAS with excitation/reconversion times of $\tau = \frac{\tau_R}{2}$.*

Comparing the experimental and simulated patterns reveals that for TQ sidebands the effect of multiple coupled spins seems to be different from the effect observed in the SQ sideband patterns. While the SQ sideband pattern of Li_xTiO_2-2 resembles the pattern calculated for one dipolar coupled spin with $\frac{D_{ij}}{2\pi} = 4$ kHz, this is not confirmed by the TQ sideband pattern. Fig. 3.31 shows the simulated lines for two ^{7}Li nuclei coupled with $\frac{D_{ij}}{2\pi} = 1$ kHz and $\frac{D_{ij}}{2\pi} = 2$ kHz as well as a simulation of a three spin system in which the observed nucleus is coupled to two other ^{7}Li nuclei with $\frac{D_{ij}}{2\pi} = 1.5$ kHz. In contrast to the observations made for the SQ sideband patterns, the effect of two additional dipole-dipole couplings is clearly different from that of a single dipolar coupled spin-pair, as they affect the first- and second-order sidebands to a different extent. The comparison of SQ and TQ sideband patterns supports the assumption that the observed dipole-dipole couplings are caused by the lattice sum of weak dipole-dipole couplings.

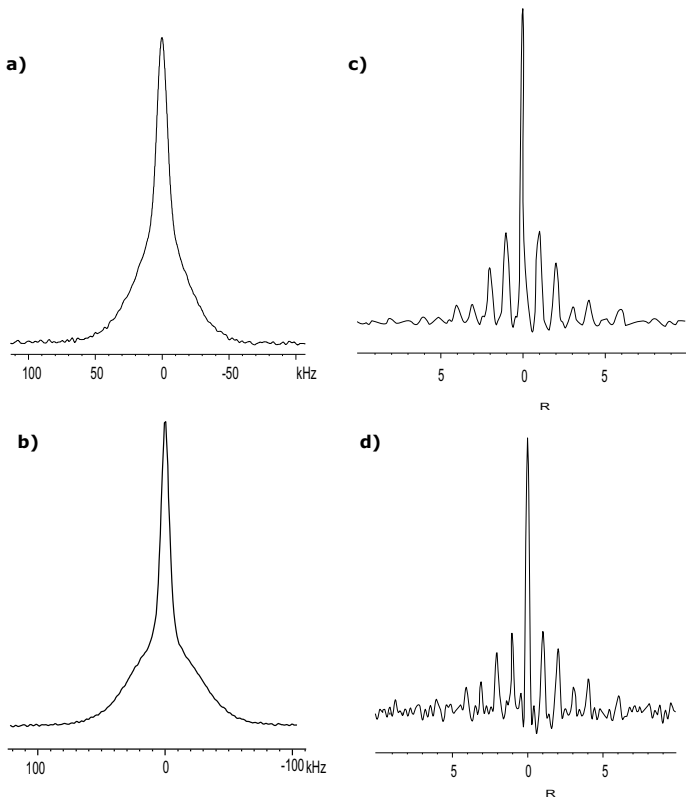

Figure 3.34: *Static ^{7}Li NMR spectra of the amorphous sample (a) and the crystalline sample (b) and ^{7}Li TQ NMR sideband patterns of amorphous sample (c) and the crystalline sample (d).*

As mentioned before, a single ^{7}Li nucleus can form a TQ coherence. Therefore, in order to be indicative of ^{7}Li -^{7}Li interactions, a four-quantum (4Q) experiment needs to be conducted in which 4Q coherences are monitored that (predominantly) arise from a ^{7}Li nucleus in a TQ state coupled to another ^{7}Li nucleus and, thus, forming a 4Q state. Fig. 3.33 shows a rotor-encoded 4Q NMR spectrum recorded on Li_xTiO_2-2 under 10 kHz MAS. For Li_xTiO_2-1, no signal was observed in the 4Q NMR spectrum, as the dipole-dipole coupling strength of $\frac{D_{ij}}{2\pi} = 2$ kHz is too weak to generate detectable 4Q signal.

3.2.4 Amorphous Sample

Fig. 3.34 shows the static ^{7}Li NMR spectra of the amorphous sample after lithium intercalation, and the line obtained from the same material intercalated with lithium after tempering to TiO_2 anatase (Fig. 3.34 a and b, respectively). The line of the amorphous

sample is slightly more broadened as compared to the line of the crystalline sample. However, in the ^{7}Li TQ sideband patterns of the amorphous and the crystalline sample (Fig. 3.34 c and d), no difference is observed, and the same holds for the SQ spinning sidebands patterns (not shown here). Thus, it can be concluded that, while the amorphous sample shows no bulk crystallinity in the X-ray investigations, the geometry of the local environment of the lithium ions is the same as in the crystalline samples, since the ^{7}Li nuclei in both samples experience the same quadrupole coupling. The slightly larger line broadening of the static spectra might be caused by a less well defined crystal structure of the amorphous sample.

3.3 Determination of Carbon-Proton Distances with REREDOR

Dipole-dipole couplings are widely used as a source of structural information, as they depend on the distance between the coupled nuclei as well as on the orientation of the internuclear vector. Thus, the knowledge of dipole-dipole coupling constants in rigid systems can provide precise information on internuclear distances, and in mobile systems information on mobility can be extracted from residual, i.e. motionally reduced, dipole-dipole couplings. In a previous study, proton-nitrogen distances could be determined with picometer accuracy [Schulz-Dobric 04] using the REREDOR experiment. In the following sections, the reliability of proton-carbon dipole-dipole couplings obtained from REREDOR experiments will be discussed.

Fig. 3.35a shows the time evolution of the REREDOR signal in the indirect dimension for the methine group in L-alanine recorded under 31250 Hz MAS with 4 rotor periods recoupling time. The sideband pattern is obtained from the time domain signal after catenating it several times prior to Fourier transformation. The dipole-dipole coupling constant is usually extracted by comparing the experimental sideband pattern with calculated ones. In Fig. 3.35b, the experimental sideband pattern is shown together with the calculated pattern for $\frac{D_{ij}}{2\pi} = 20.5$ kHz. Additionally, the calculated patterns for $\frac{D_{ij}}{2\pi} = 20$ kHz and $\frac{D_{ij}}{2\pi} = 21$ kHz are shown in Fig. 3.35c and d. As all lines show significant deviations from the experimental pattern, a precise determination of the coupling constant by a simple comparison of the spectra is problematic, and the estimated error is larger than 500 Hz. The deviations of the simulated and experimental data might either arise from imperfections of the experimental setup or from slight oversimplifications in the simulations. In the following sections, first, systematic errors arising from experiments, and subsequently the reliability of the calculations and fitting procedures will be discussed.

3.3.1 Experimental Setup

This section focuses on systematic errors potentially arising from the experimental setup. As the REREDOR sequence is a multi-pulse sequence performed under MAS, the **timing of the pulses** is crucial. The REREDOR experiments presented in this section were performed under 31250 Hz spinning. This frequency was chosen as it corresponds to a rotor period of exactly 32 μs and, hence, the time increment in the direct dimension can

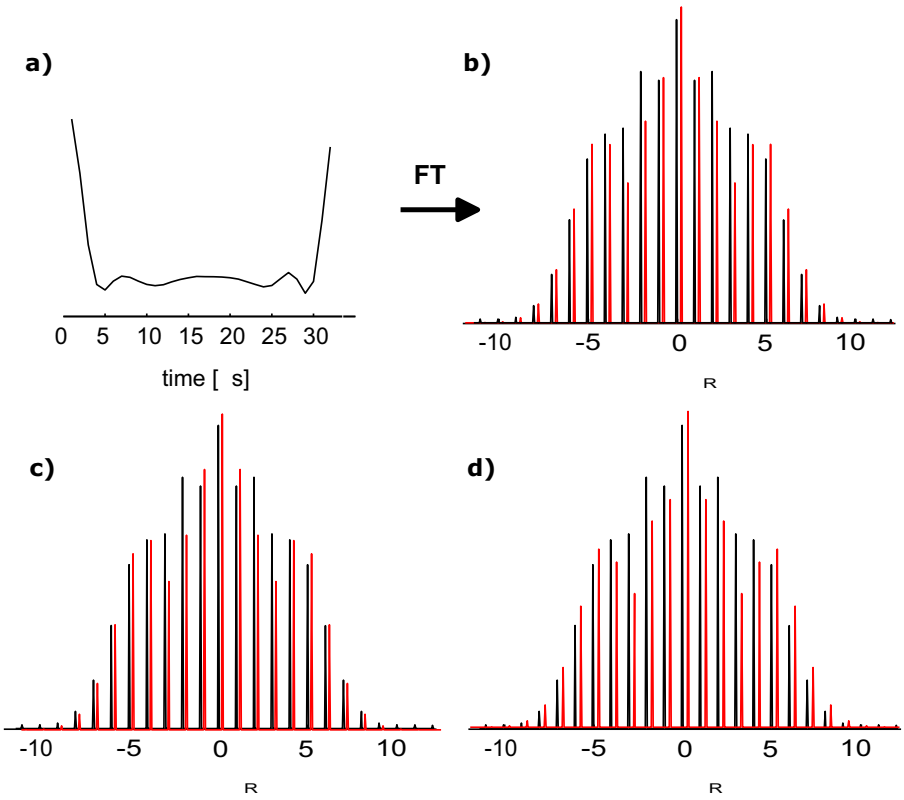

Figure 3.35: *(a) REREDOR time domain signal in the indirect dimension recorded for the methine group of alanine under 31250 Hz MAS using a recoupling time of four rotor periods. Sideband pattern obtained by Fourier transformation of the signal (black line), together with the sideband pattern obtained by an analytic calculation with (b)* $\frac{D_{ij}}{2\pi}$*=20.5 kHz, (c)* $\frac{D_{ij}}{2\pi}$*=20 kHz, and (d)* $\frac{D_{ij}}{2\pi}$*=21 kHz (red lines).*

be chosen to be exactly 1 μs by acquisition of 32 data points per rotor period. This is important, as the internal spectrometer timing cannot deal with arbitrary timing intervals, and the time increment in the indirect dimension is rounded before incrementation of t_1. This leads to a increasing timing offset of the time in the indirect dimension when working with t_1 increments that cannot precisely be handled by the spectrometer. Under 31250 Hz MAS, t_1-FIDs recorded with 32 and 64 data points per rotor period did not show significant deviations or other timing problems.

For setup purposes, the pulse power levels are usually adjusted in a single-pulse or CP experiment. To investigate the **influence of misadjusted pulses**, numerical simulations were carried out within the SIMPSON programme package [Bak 00] with slightly varying pulse lengths (see Fig. 3.36 a-d). This data is compared to experimental spectra recorded

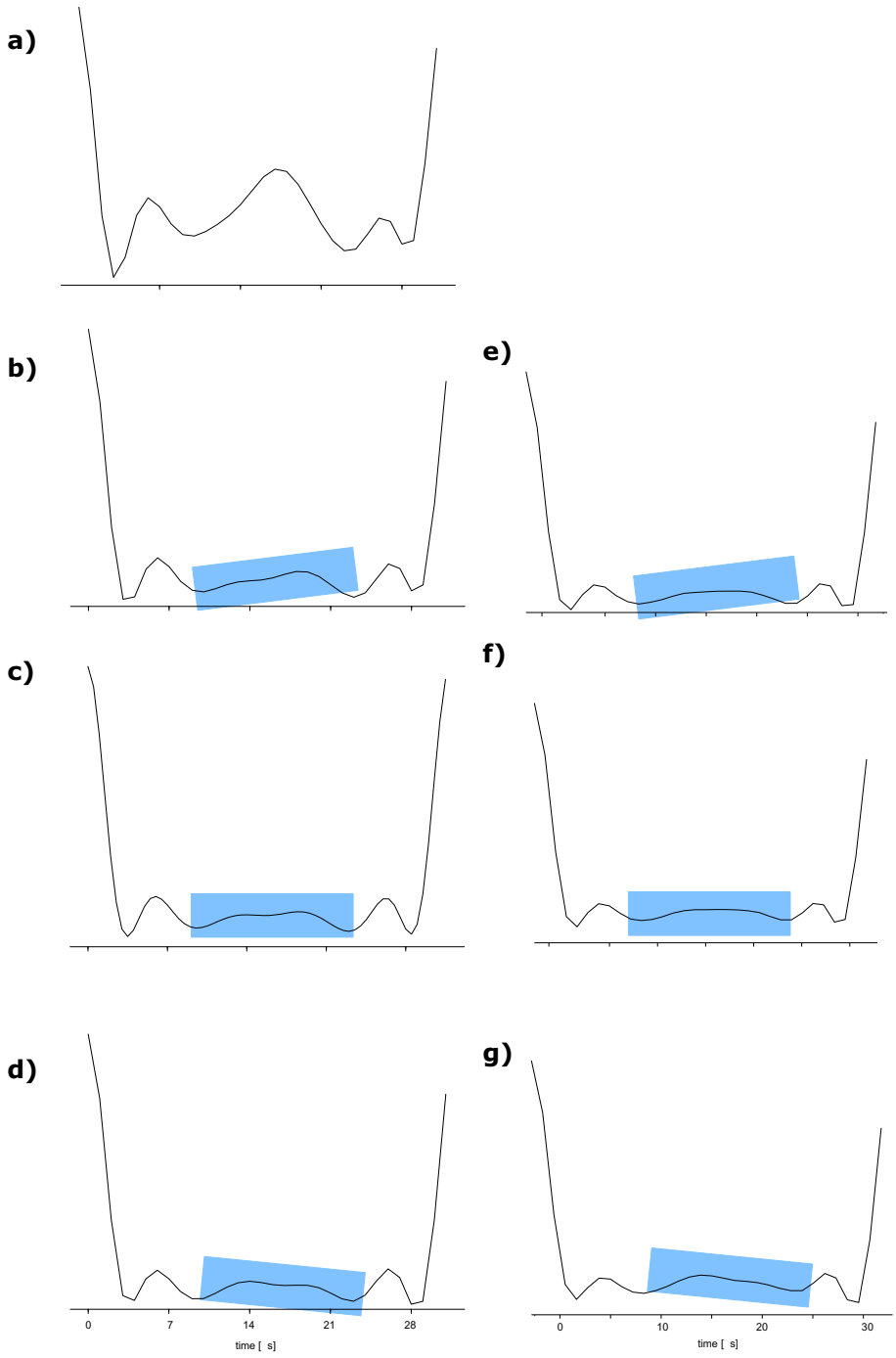

Figure 3.36: *(a-d) Simulated REREDOR signals including pulse imperfections: (from top to bottom) pulse length multiplied with a factor of 0.9, 0.98, 1.0 and 1.02. (e-g) Experimental REREDOR signals with decreasing pulse power level (top to bottom).*

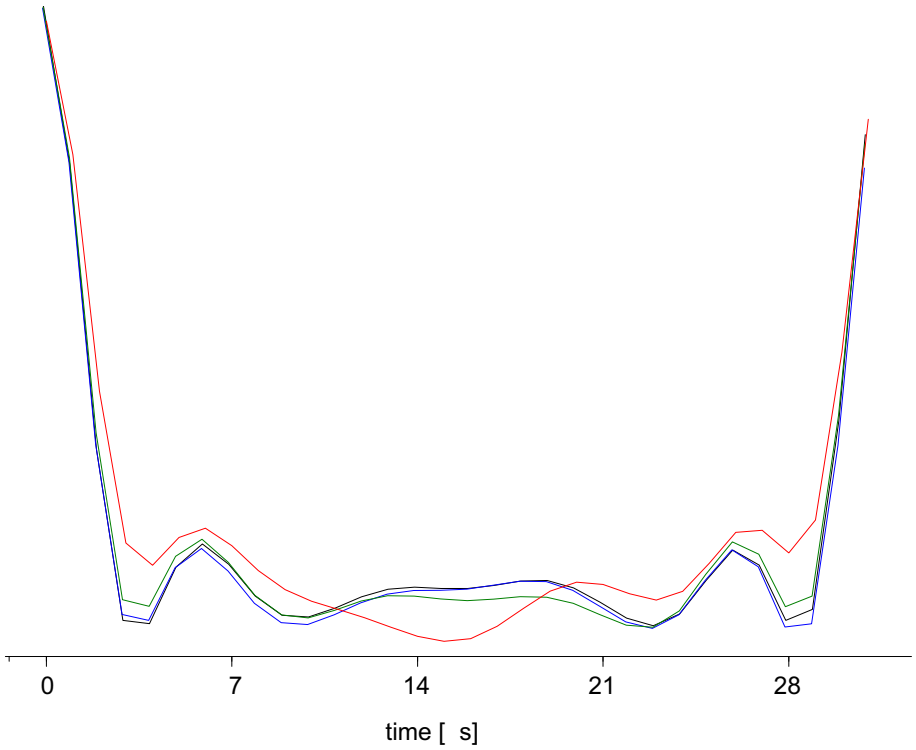

Figure 3.37: *Simulated REREDOR curves without chemical shift (black line) and including chemical shifts of 52 ppm (blue line), 100 ppm (green line) and 180 ppm (red line) relative to the RF carrier frequency.*

with different pulse power levels (see Fig. 3.36 e-g). The influence of pulse misadjustments observed in the experiments is reproduced by the calculations. For small misadjustments the influence is only minor, and if precise measurements are needed, the pulse power levels can be directly set in REREDOR experiment on a reference sample, e.g. alanine.

Another parameter to be set in the experiments is the **irradiation frequency** of the RF pulses. If it is not set on the resonance of the ^{13}C nucleus under investigation, the signal evolves under the ^{13}C chemical-shift. In the REREDOR pulse sequence, a central 180° pulse is applied on the carbon channel to refocus the evolution under the chemical-shift, but this compensation is only accomplished in a first-order approximation, while higher-order cross-terms of the Hamiltonians may still cause weak perturbations. Fig. 3.37 shows simulated t_1-data with different ^{13}C chemical shifts, from which it is obvious that the shifts have an influence on the signal. If only one dipolar coupled proton-carbon pair is investigated, it is therefore advisable to set the irradiation frequency to the ^{13}C resonance frequency. If more than one ^{1}H -^{13}C pair is investigated and the time requirements of

the experiment do not allow for separate measurements, the CS can be included in the simulations, as it is precisely known from the ^{13}C spectra. For the experiments performed on the methine group in alanine, the irradiation frequency was set to the resonance frequency of the methine carbon. Experiments with different irradiation frequencies on the protons did not show significant deviations. The same holds for simulations including the CSA of the alanine methine carbon.

Finally, another potential source of experimental errors are **instabilities of the rotor spinning**. The influence of fluctuations in the spinning frequency has been discussed in [Schulz-Dobric 04]. It was shown that the intentional use of "bad" rotors can significantly influence the recorded FIDs, while for intact rotors these influences were neglible. To check for the influence of fluctuations of the spinning axis as well as slight misadjustments of the magic angle, simulations with small magic-angle offset were carried out, but did not show significant deviations and can hence not serve as an explanation for the observed deviations between theory and experiment.

As ^{13}C labelled alanine is used in the experiments, the noise level in the direct dimension is very low. This leads to the fact that the noise in the indirect dimension exceeds the noise in the direct dimension. To arrive at a measure of the noise level in the indirect dimension, a series of REREDOR spectra was recorded with the same t_1. The noise level was found to be about 1% of the maximum signal amplitude (which is about 10 times as large as the noise in t_2) and was used to determine the significance of the results obtained from the fitting procedures which are discussed in the following section.

3.3.2 Simulations

The calculated patterns can either be obtained by using the analytic expression (see Eq. (2.88)) or by numerical simulations using the SIMPSON programme package [Bak 00]. The advantage of the analytic expression over the numerical simulation is the much shorter computation time. However, the analytic expression contains several approximations: The applied pulses are assumed to be infinitely short, and the calculations are restricted to ideal 2-, 3- or 4-spin systems, in which only the heteronuclear dipole-dipole interaction is considered, while all other perturbing interactions are neglected. Furthermore, the analytic expressions do not account for other coherences or relaxation phenomena.

In general, a fit of the time domain signal is expected to yield more reliable values and errors [Hodgkinson 97] than a simple comparison of the sideband patterns. Therefore,

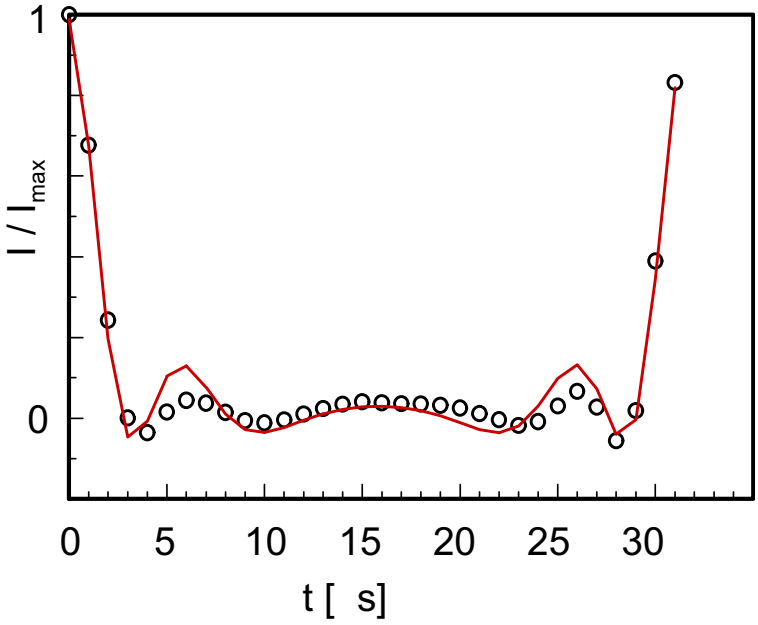

Figure 3.38: *Time domain fit of the experimental REREDOR signal (dots) with the analytical model (red line).*

a least-squares fit of the time domain signal was performed using the analytic model, yielding $\frac{D_{ij}}{2\pi} = 20.1$ kHz $\pm$ 0.3 kHz for the methine group in alanine. However, as can be seen in Fig. 3.38, the significance of the fit is rather low, i.e. the analytic calculation does not fully reproduce the experimental signal, but exhibits small characteristic deviations.

The largest systematic error of the analytical fit is the assumption of **infinitely short pulses**. The experiment was performed under 31250 Hz MAS, i.e., one rotor period has a length of 32 μs, while the pulse duration of the 180° pulses spaced at half rotor periods is 5 μs. Consequently, the fraction of a rotor period in which pulses are applied is about 30%, resulting in a lower recoupling efficiency. To visualise this effect, a signal with $\frac{D_{ij}}{2\pi} = 21$ kHz was numerically simulated with pulse length 0.25 μs and 2.5 μs, respectively. For the short pulse length, the analytic calculation nicely matches the numerical simulation with same dipole-dipole coupling strength (see Fig. 3.39a). However, when 2.5 μs are used, the calculated line (red line in Fig. 3.39b) significantly deviates from the simulation, and a fit of the analytic model yields $\frac{D_{ij}}{2\pi} = 19.8$ kHz. In addition, the calculated signal does not fully reproduce the shape of the simulated line. In a previous work [Schulz-Dobric 04], a correction of the analytic calculation for REREDOR signals was derived on the basis of a work of Jaroniec et al. [Jaroniec 00]. In these calculations, the dipole-dipole coupling constant is reduced by a factor, depending on the ratio of

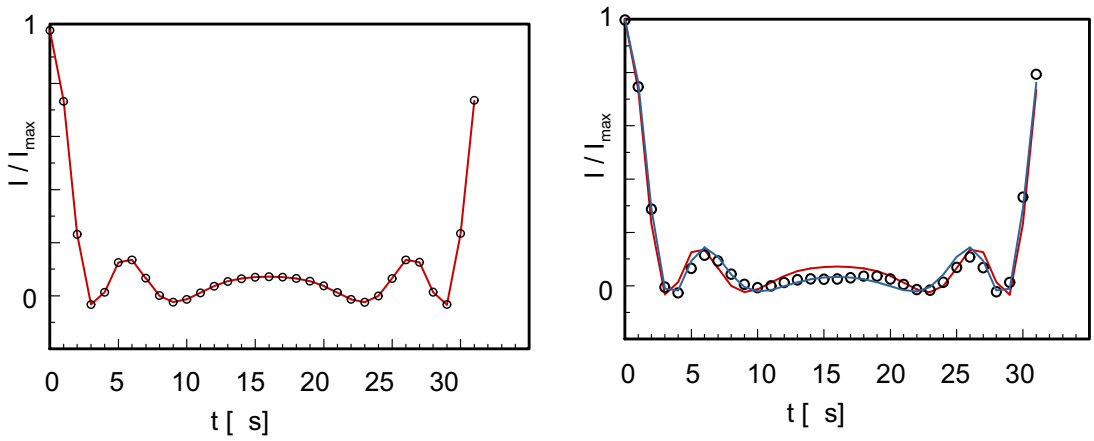

Figure 3.39: *Simulated REREDOR curves with* $\frac{D_{ij}}{2\pi}$*=21 kHz using 180° pulses of 0.25 µs (a) and 2.5 µs (b). The red line is the analytic calculation for* $\frac{D_{ij}}{2\pi}$*=21 kHz, while the blue line in (b) shows the analytic calculation that fits best (*$\frac{D_{ij}}{2\pi}$*=19.8 kHz).*

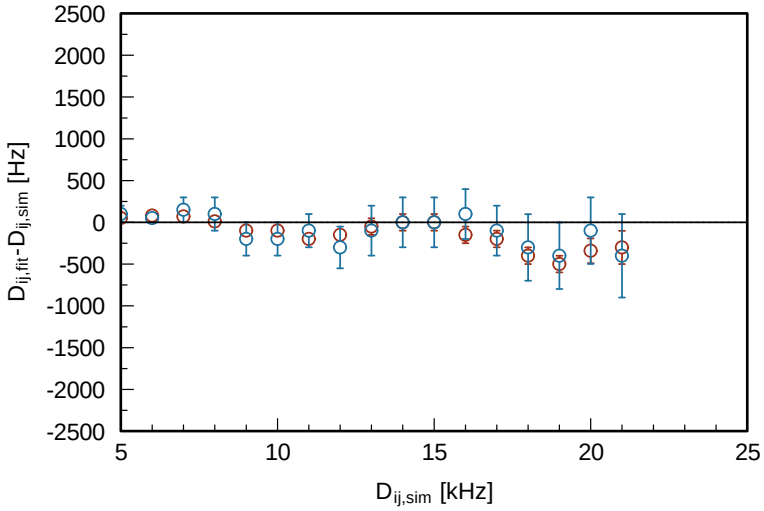

Figure 3.40: *Deviation of the dipole-dipole coupling of the fit and the simulation for least-squares fit with the analytic function including finite pulse length correction.*

the pulse length and the rotor period. Using this correction, a dipole-dipole coupling of $\frac{D_{ij}}{2\pi}$ = 20.2 kHz is obtained for the signal simulated with $\frac{D_{ij}}{2\pi}$ = 21 kHz. However, as the correction just scales the dipole-dipole coupling, the shape of the line is not changed and, hence, the significance of the fit is not improved.

To further test the pulse-length correction, REREDOR signals were simulated for several

dipole-dipole coupling strengths, and then fit with the analytic model. Noise was added in the simulations, using levels of 1% and 10% of the maximum signal amplitude. These noise levels are typical values found in spectra experimentally recorded on labelled and natural abundance samples, respectively. For each coupling strength and noise level, five FIDs were simulated and fitted with the analytical model including the finite-pulse correction. Fig. 3.40a shows the deviation of the dipole-dipole coupling obtained from the fit and the simulation together with the error margins resulting from the fit. First, it should be noted that all deviations lie within the range of ±500 Hz. For large couplings, the fitted values show a clear tendency to slightly underestimate the actual coupling, significantly so for simulated data with low noise level and $\frac{D_{ij}}{2\pi} > 18$ kHz. Additionally, the significance was rather low for these fits. A more detailed study revealed that this effect depends on the product of pulse length t_p and coupling strength $\frac{D_{ij}}{2\pi}$. For $\frac{D_{ij}}{2\pi}\, t_p$ >0.03, the significance of the fit is poor and the coupling parameters are underestimated. This means that for a coupling strength of $\frac{D_{ij}}{2\pi} = 21$ kHz, a pulse length of 1.5 μs (for $\frac{\pi}{2}$ pulses) is required, which is, in principle, technically accessible with standard probes, in order to avoid significant deviation of the analytic and simulated data.

From the above observations it becomes clear that, especially for large dipole-dipole couplings as they are typically found for rigid ^{1}H -^{13}C bonds, the analytic model is only suited to a limited extent, as long as pulse lengths larger than 1.5 μs are applied. Therefore, a least squares fit of the numerical simulation was performed on the experimental data, using the MINUIT optimisation tools implemented in SIMPSON [Vosegaard 02]. From this, a dipole-dipole coupling of $\frac{D_{ij}}{2\pi} = 20.9$ kHz ± 0.2 kHz could be obtained. The significance of the fit was considerably improved (see Fig. 3.41), but was still relatively low.

So far, only one CH dipolar coupled pair was considered in the simulations. In real systems, however, also **contributions from other protons** have to be taken into account. In [Schulz-Dobric 04], it was shown that usually only the influence of the strongest perturbing coupling has to be considered. Unfortunately, for alanine-CH, six further protons at approximately the same distance are found in the methyl and ammonium group. A calculation of all six protons plus CH group is not feasible on a routine basis and, in addition, the large number of parameters would probably lead to ambiguous results. To estimate the systematic error arising from these protons, a four-spin system was simulated, placing two additional protons at the position of the centre of the methyl and ammonium group, respectively, with reduced dipole-dipole couplings to account for the averaging effect of the methyl and ammonium rotation. The so-obtained data set was then fitted using the

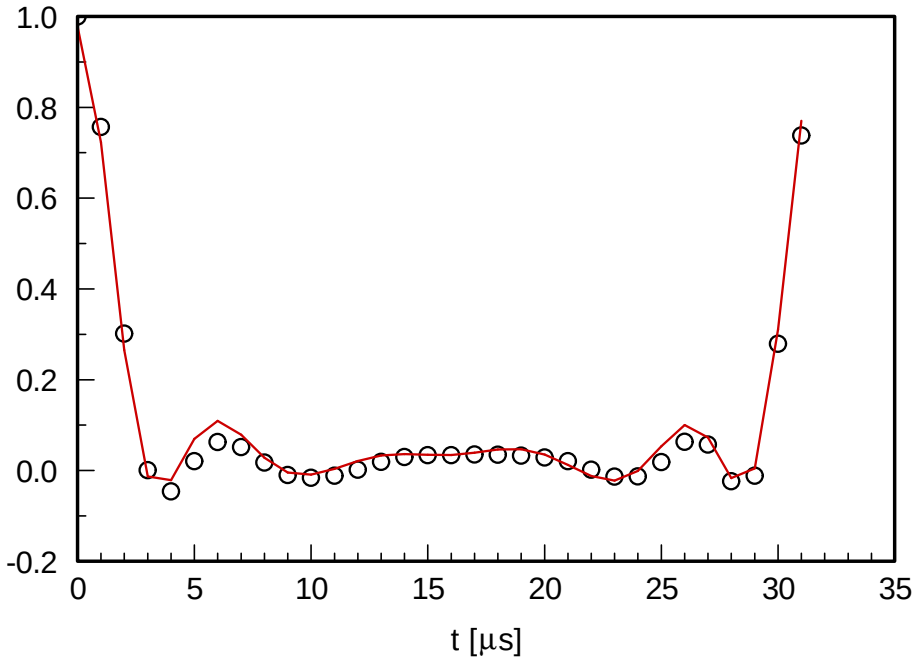

Figure 3.41: *REREDOR signal of the methine group in alanine recorded under 31250 Hz MAS using 4 rotor periods recoupling (dots) and numerical simulation of a two-spin system that fits best ($\frac{D_{ij}}{2\pi}$=20.9 kHz).*

numerical simulation of a two-spin system. The dipole-dipole coupling of the methine group was set to $\frac{D_{ij}}{2\pi} = 20.9$ kHz in the simulation and, from the fit with the two-spin system, a coupling constant of $\frac{D_{ij}}{2\pi} = 20.75$ kHz $\pm$ 0.2 kHz was obtained. As can be seen in Fig. 3.42, the deviations of the signals of the two-spin and the four-spin system are similar to the deviations of the experimental signal and the two-spin simulation. From the above analysis, the dipole-dipole coupling constant of the methine group in alanine can safely be determined as $\frac{D_{ij}}{2\pi} = 21.0$ kHz with an error margin of $\pm$0.5 kHz.

3.3.3 CH Distances

The main intention of measuring dipole-dipole coupling constants in rigid molecules is the determination of internuclear distances. The internuclear distance is related to the dipole-dipole coupling by

$$D^{(ij)} = \frac{\mu_0 \hbar \gamma_i \gamma_j}{4\pi r_{ij}^3} \tag{3.9}$$

The dipole-dipole coupling constant determined experimentally is actually motionally averaged due to nuclear motions that occur on fast timescales, such as stretching motions

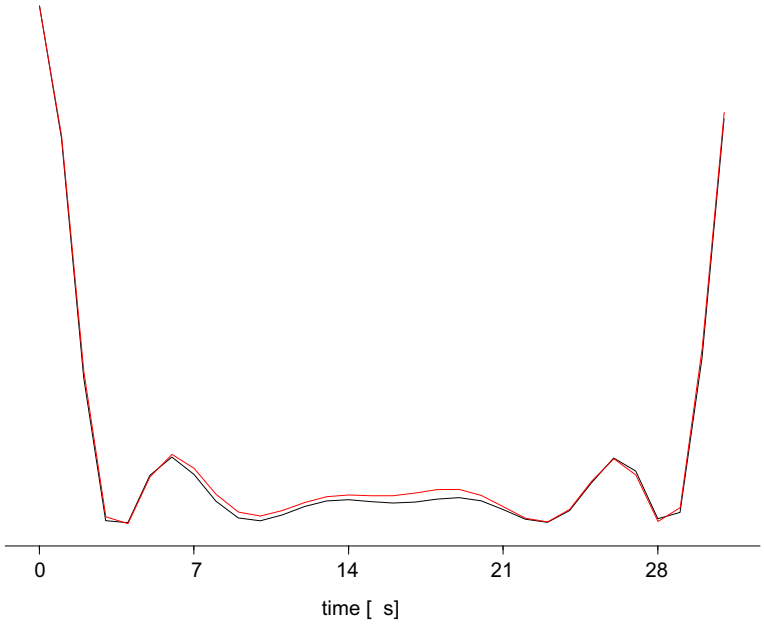

Figure 3.42: *Simulation of a four-spin system with two additional protons placed at the position of the centre of the methyl and ammonium group, respectively. The dipole-dipole coupling of the methine group was set to* $\frac{D_{ij}}{2\pi}$*=20.9 kHz (black line). The so-obtained data set was then fitted using the numerical simulation of a two-spin system (red line), yielding a coupling constant of* $\frac{D_{ij}}{2\pi}$*=20.75 kHz.*

and/or reorientations of the internuclear vector with respect to the magnetic field θ:

$$\langle D^{(ij)} \rangle_{\mathrm{NMR}} \sim \langle r_{ij}^{-3} \frac{1}{2} (3\cos^2(\theta) - 1) \rangle_{\mathrm{NMR}} \tag{3.10}$$

In [Schulz-Dobric 05] the stretching motion was found to only marginally influence the coupling, because the effect of $\langle r_{ij}^{-3} \rangle_{NMR}$ weighting, causing an increase of the averaged dipole-dipole coupling, is compensated by the enlarging of the mean distance due to the asymmetric energy potential. The bending motions had a much larger influence on the averaged NH dipole-dipole coupling, leading to a reduction of $\langle D^{(ij)} \rangle_{\mathrm{NMR}}$ of about 7%, corresponding to an enlargement of the N-H bond $\langle r_{ij} \rangle_{\mathrm{NMR}}$ by about 2.5 pm.

In the previous section, the dipole-dipole coupling constant of the alanine methine group was determined to be $\langle D^{(ij)} \rangle_{\mathrm{NMR}} = 21$ kHz $\pm$ 0.5 kHz, corresponding to a bond length of $\langle r_{ij} \rangle_{\mathrm{NMR}} = 110$ pm $\pm$ 1 pm. Hence, the influence of nuclear motion might exceed the experimental error. Thus, when comparing the internuclear distance obtained from NMR experiments to quantum-chemical calculations or, e.g., X-ray structures, this averaging

has to be taken into consideration. Quantum-chemical calculations of the dipole-dipole coupling including zero-point vibrations were implemented by Thorsten Metzroth (University of Mainz) and calculations on L-alanine are currently underway. Preliminary results showed a decrease of the CH dipole-dipole coupling by about 500 Hz, due to zero-point vibrational motions such as bending and stretching motions. Thus, the expected deviations are of the same order as the experimental accuracy, whose main limitation arises from the influence of additional dipole-dipole couplings, i.e multiple spin effects.

3.4 Discussion

In Sec. 3.1.1 it was shown that ^{2}H MAS NMR spectra are comparable to ^{1}H MAS NMR spectra with respect to chemical shifts and resolution. In combination with recrystallisation of the samples from deuterated solvents, this provides a simple method to assist the assignment of ^{1}H /^{2}H resonance lines.

In samples deuterated at various positions, the parameters of ^{2}H quadrupole couplings can be determined individually for each site by the newly developed ^{2}H 2D DQ OMAS experiment which correlates the isotropic chemical shifts with quasistatic DQ-filtered line shapes. The sensitivity range of the experiment can be optimised with respect to the material under investigation by adjusting the magic-angle offset. Furthermore, no additional equipment is needed, as the experiment can be performed on commercially available probes. The five-pulse sequence used in the experiment is particularly robust and easy to use. Moreover, it readily allows for further extension of the experiment, for example towards 3D ^{2}H exchange experiments.

The quadrupole coupling parameters of L-histidine hydrochloride monohydrate were, without further effort, determined to a satisfactory precision. In contrast to spinning sideband patterns, the extraction of quadrupole coupling parameters from quasistatic DQ-filtered line shapes is unproblematic even for small values of the asymmetry parameter η. The experiments performed on alkylamines showed that the ^{2}H 2D DQ OMAS experiment is especially suited for the investigation of mobilities of different positions in a molecule in temperature-dependent experiments.

In ^{7}Li NMR experiments performed under static and MAS conditions, the sensitivity of the quadrupole coupling tensor on the electronic environment provides information on the crystal symmetry. The strength of ^{7}Li -^{7}Li dipole-dipole couplings can be extracted from ^{7}Li 3Q NMR sideband patterns, while for the identification of ^{7}Li -^{7}Li proximities a 4Q experiment experiments can be performed. The investigation of a Li_xTiO_2 sample that, according to X-ray diffraction, seemed to be amorphous revealed that the sample is actually nanocrystalline and has the same local structure as the crystalline materials.

The ^{1}H -^{13}C REREDOR experiment was found to be capable of determining the averaged CH bond distance in the alanine methine group to picometer accuracy. The limiting factor of the precision is not the experimental setup, but the influence of additional dipole-dipole couplings arising from the methyl and ammonium protons, that are difficult to account for in the simulation. A recrystallisation from D_2O leading to a replacement of the protons

in the ammonium group by deuterons might improve the precision.

As mentioned above, ^{2}H MAS NMR with CS resolution is feasible. This opens up the possibility to perform ^{2}H spectroscopy in analogy to the ^{1}H case, i.e. including homo- and heteronuclear dipolar recoupling. As a first example, this has already been implemented by Martin Schulz-Dobrick [Schulz-Dobric 04] for ^{1}H -^{2}H and ^{2}H -^{15}N correlation experiments as well as for a ^{2}H -^{15}N REREDOR experiment. The development of a ^{2}H -^{13}C REREDOR experiment is currently underway and opens up the possibility to study ^{1}H -^{2}H isotope effects on C-H bonds. While the CS resolution in ^{2}H and ^{1}H experiments is similar, the application of 180° pulses on deuterium is problematic. Therefore, the pulse sequences used for ^{1}H -^{13}C experiments cannot be readily adopted to ^{2}H -^{13}C experiments but must be changed in such a way that the number of pulses applied on deuterons is minimised.

The comparison of experimentally determined ^{2}H quadrupole coupling parameters with quantum-chemical calculations revealed that quadrupole coupling parameters are especially sensitive to the geometry of hydrogen-bonds for which temperature effects have to be considered in the calculations. To fully reproduce the experimental results zero-point vibrations have to be taken into account. This was also found for the comparison of CH distances obtained by REREDOR experiments and quantum-chemical calculations. Furthermore, it should be noted, that a more detailed analysis of the structure of Li_xTiO_2 should be possible by comparing the ^{7}Li quadrupole coupling parameters with EFG calculations. Thus, the combination of solid-state NMR experiments and quantum-chemical calculations can provide information on mobility and structure of molecules not accessible by NMR experiments alone. This will be subject of the next chapter.

Chapter 4

Combining Solid State NMR Experiments and Quantum Chemical Calculations

In recent years concepts of supramolecular self-assembly and self-organisation have attracted considerable interest as a means to build structures on the nanoscale. In these architectures non-covalent interactions, e.g. hydrogen bonding and aromatic π-π interactions, are of particular importance as they usually determine the superstructure. Solid state NMR is a powerful tool to investigate non-covalent bonding, as the ^{1}H chemical shift is a sensitive probe of hydrogen-bonding and aromatic ring current effects. This is especially useful in cases where X-ray investigations fail, e.g. in disordered or partially mobile systems. However, supramolecular organic structures usually contain a large number of protons and in rigid systems the resolution of solid-state NMR spectra suffers from line broadening. Hence, the identification and assignment of ^{1}H lines is often obscured. Additionally, from NMR investigations alone only qualitative information on secondary interactions can be inferred.

Quantum-chemical calculations of NMR parameters can supplement the interpretation of NMR spectra by assisting the resonance assignment and providing quantitative information on secondary interactions. For instance, a combined experimental and theoretical approach carried out on hexabenzocoronene derivatives allowed the observed ^{1}H chemical shifts to be related in a quantitative manner to the intermolecular structure [Ochsenfeld 01].

In this chapter, two examples of supramolecular architectures investigated by a combi-

nation of solid-state NMR and quantum-chemical calculations will be presented.

4.1 Molecule Trapping in Calix[4]hydroquinone Nanotubes

Hollow tubular self-assembled structures based on organic molecules have attracted considerable interest, because of their potential abilities for artificial biological channels, drug delivery, nanochemical reactors, and nano-organic materials. Kim and coworkers synthesised self-assembled organic nanotubes composed of nontubular subunits of calix[4]hydroquinone (CHQ) [Hong 01b, Hong 01a], which were initially designed by computational methods. These CHQ-nanotubes combine a tubular structure with an strong electrochemical reduction potential and can therefore be used as templates for silver nanowires [Kim 02a, Kim 02b]. Calix[4]arenes are well-known host molecules with a pronounced capability of including small guest molecules [Namor 98, Ikeda 97]. Therefore, the question arises whether the tubes are actually hollow or whether another species is trapped inside the CHQ bowls in the course of the production process. X-ray data, however, cannot provide clear evidence for the presence of guests, such as acetone [Ungaro 84, Lu 99, Lu 00] and water [Zhang 92, Leverd 00], because disordered or mobile species cannot be observed. In this section, ^{1}H and ^{2}H solid-state NMR experiments combined with ab-initio calculations of NMR parameters [Brown 01, Ochsenfeld 02, Sebastiani 01, Sebastiani 03] will be presented that provide information on the inclusion of guest molecules in the CHQ nanotube crystals.

4.1.1 The Structure of Calix[4]hydroquinone Nanotubes

Experimentally, the CHQ nanotubes are grown from a mixture of water and acetone. The addition of water molecules to a solution of CHQ in acetone results in stable self-assembling tubular polymers of CHQ in solution. As the solvents evaporate, these tubes arrange in bundles to form needlelike crystals with sizes depending on the evaporation rate. In the crystal structure obtained by X-ray crystallography [Hong 01b], the CHQ molecules adopt a bowl shaped conformation (Fig. 4.1a), which is well known from related calix[4]arenes [Namor 98, Ikeda 97]. It is stabilised by the four inner hydroxyl groups which form a circular proton tunnelling resonance of hydrogen-bonds at the bottom of each bowl. The tubes (Fig. 4.1b) are built from stacks of CHQ molecules which are tied together at their upper rims through extended one-dimensional arrays of –O–H$\cdots$O hydrogen bonds. Each of these arrays consists of a well-defined sequence of water molecules

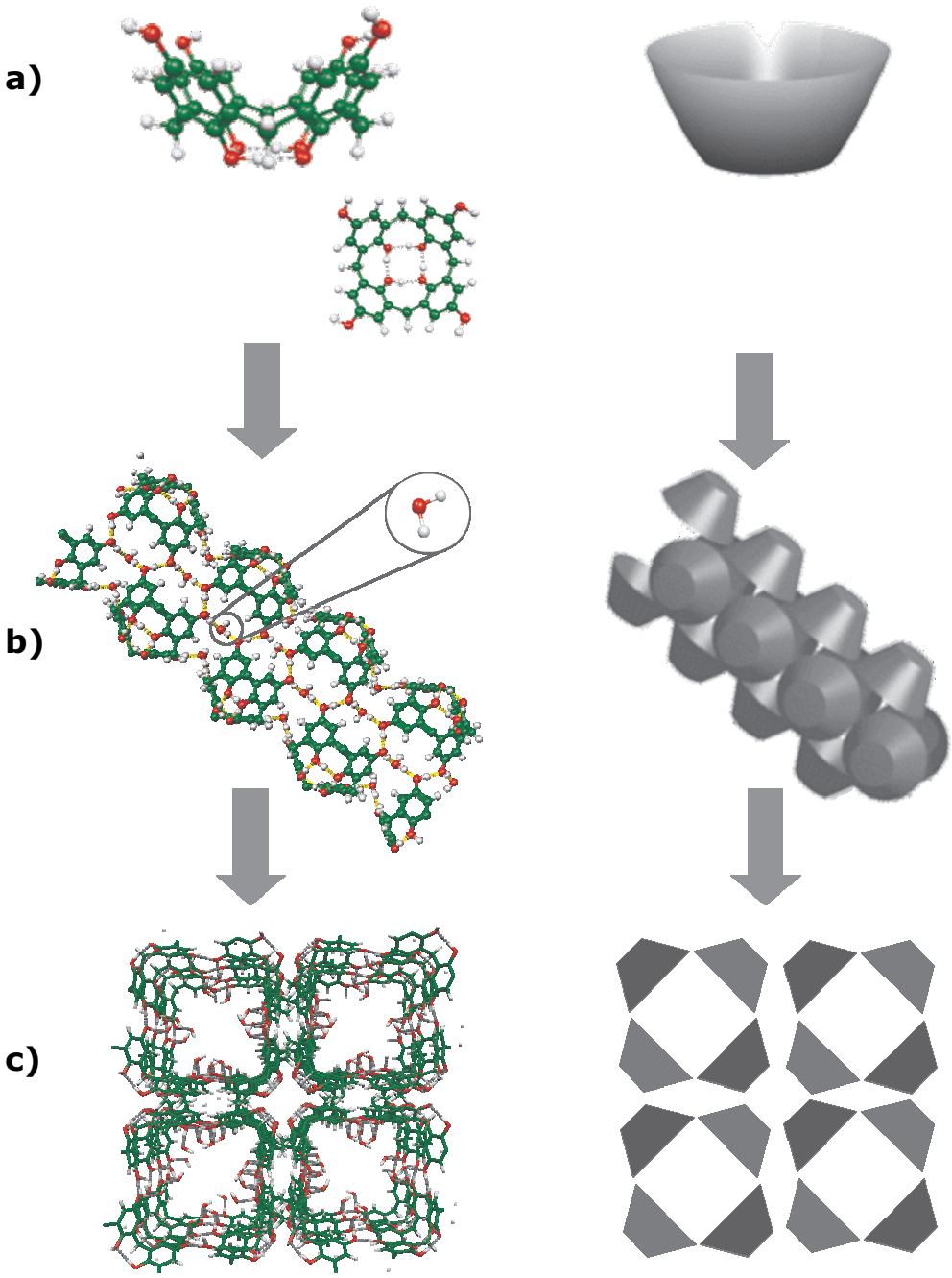

Figure 4.1: *(a) Bowl-shaped conformation of calix[4]hydroquinone, stabilised by proton tunnelling resonance of the bottom H-bonds. (b) Self-assembly of the CHQ bowls into nanotubes, via 1D chains of hydrogen bonds composed of the rim OH groups and water molecules. (c) Arrangement of the tubes in rectangular arrays via π-π stacking pairs.*

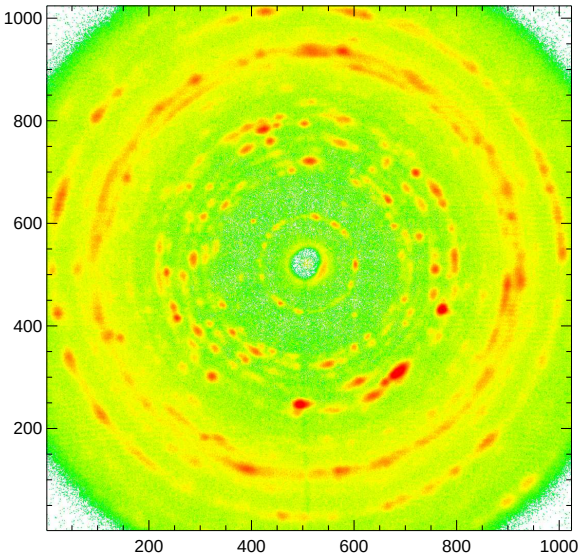

Figure 4.2: *Wide angle X-ray diffraction pattern of CHQ nanotube crystals (Jochen Gutmann).*

and the hydroxyl groups at the upper rim of the CHQ molecules. Due to this arrangement, the CHQ bowls are open towards the inner part of the tubes, and one proton per bridging water molecule is potentially available for additional hydrogen bonding. In the crystal, the tubes arrange in chessboard-like rectangular arrays via displaced π-π stacking pairs (Fig. 4.1c). Each nanotube has a 17 Å $\times$ 17 Å cross section with a 6 Å $\times$ 6 Å pore (with the van der Waals volume excluded).

The CHQ nanotube samples investigated in this thesis were synthesised by Dr. Erli Sugiono in our research group (for details see [Hoffmann 04]). The wide angle X-ray diffraction pattern of the CHQ nanotubes measured with only a small number of needlelike crystals in the scattering volume is shown in Fig. 4.2. The observed distinct reflections indicate that the needles are single crystals.

4.1.2 Solid State NMR and Calculations of the Hollow Nanotubes

Carbon chemical shifts of a single CHQ were calculated at the Hartree-Fock level using the program package TURBOMOLE [Ahlrichs 89] (see Appendix B). As packing effects (such as π-π-stacking and hydrogen-bonding) are expected to influence the ^{1}H chemical

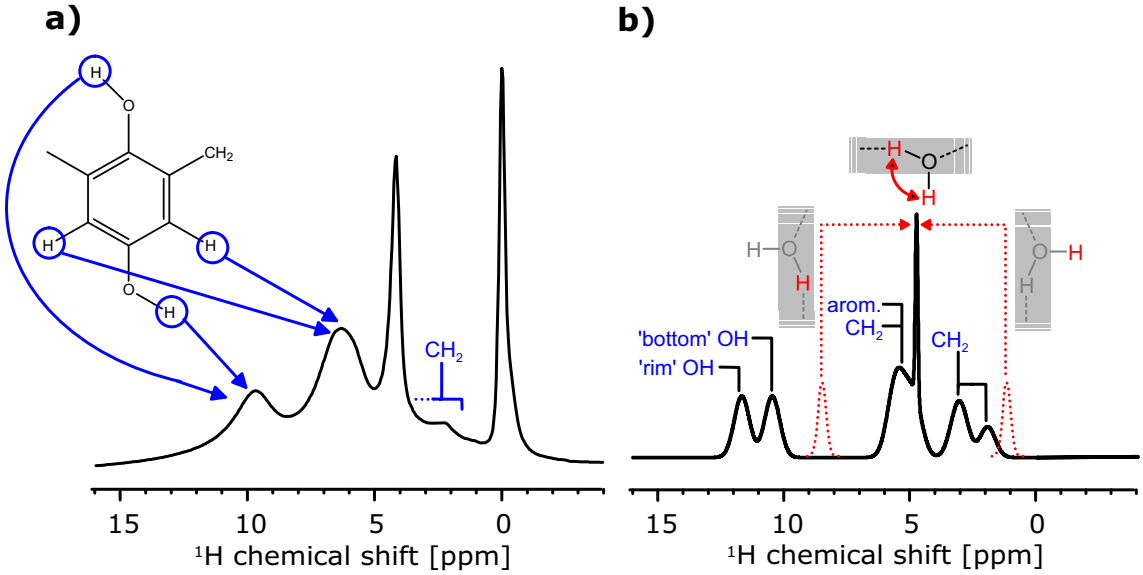

Figure 4.3: *(a) ^1H solid-state NMR spectrum of CHQ nanotubes recorded under 30 kHz MAS. (b) Calculated ^1H spectrum of the CHQ nanotubes (without guest molecules). The lines originating from the two protons of the water molecules in the hydrogen-bond chain have been averaged in order to account for fast motional processes in which the protons interchange their positions. Different Gaussian line broadening was applied for the signals of rigid (nanotube) and mobile (water) atoms.*

shifts, ^{1}H NMR spectra were calculated by Dr. Daniel Sebastiani by means of density functional theory (DFT) using a fully periodic description of the systems [Sebastiani 01, Sebastiani 03] within the pseudopotential plane wave programme package CPMD [Hutter 03] (see Appendix B).

The experimental ^{1}H MAS NMR spectrum of the CHQ nanotubes is shown in Fig. 4.3 a. Based on typical values of ^{1}H chemical shifts, the signals at 10 ppm and 6.5 ppm can be ascribed to the CHQ hydroxyl and aromatic protons, respectively. The resonance position of the hydroxyl protons at 10 ppm is shifted downfield, which is characteristic for protons involved in hydrogen bonds. For the methylene protons, a line at 2 ppm would be expected, and in the spectrum a distinct shoulder is observed at this position. However, the line seems to be significantly broadened by packing effects and partly lies underneath the other resonance lines. It therefore cannot be assigned to a single ppm value. The two relatively sharp lines at -0.5 ppm and 4.5 ppm cannot be readily assigned. Spectra recorded on different CHQ nanotube samples showed variations in the integral intensities of the line at 0.5 ppm as well as deviations in the position of the signal at

4.5 ppm, indicating that these resonances sensitively depend on the sample preparation.

The calculated spectrum shown in Fig. 4.3 b confirms the assignment of the CHQ signals. In the case of the hydroxyl protons, the calculation yields two separated resonances for the four protons forming the strong ring-shaped hydrogen bonds at the bottom of the CHQ cones, and the four hydroxyl protons at the rim which are involved in the extended chain of hydrogen bonds along the tubes. Experimentally, however, the spectral resolution does not allow for this distinction among the hydroxyl resonances. The methylene proton resonances are found to be spread over a range from about 2 ppm up to 5 ppm, which includes considerable downfield shifts due to "ring current effects" arising from the π-electrons of the aromatic rings in neighbouring CHQ. Experimentally, this spread is reflected by the broad methylene line which is not resolved in the one dimensional ^{1}H NMR spectrum.

Turning to the water molecules, the calculations yield two separated ^{1}H resonances at 8.5 ppm and 1 ppm, which belong to the same water molecule and arise from the proton involved in the hydrogen bonding and from the other proton dangling freely inside the tube. Experimentally, an intense resonance is observed at -0.5 ppm (Fig. 4.3a), which could correspond to the "free" protons of the water molecules, but there is no counterpart resonance at around 8.5 ppm. Moreover, the thermal energy at room temperature is expected to cause fast reorientation motions of the small water molecules. Thereby, the two protons interchange their positions and average their resonance frequencies to about 4.8 ppm, which corresponds to the rather sharp signal at 4.5 ppm in the experimental spectrum.

Accidentally, about the same chemical shift would be observed for water in a liquid bulk phase. However, the samples were dried under moderate conditions after crystallisation to remove residual amounts of volatile solvent. Exposing them to more drastic heat and vacuum conditions showed that signal losses at 4.5 ppm are always associated with a highfield shift of the hydroxyl signal and changes over the whole spectrum. This indicates that the network of hydrogen bonds is directly affected and, after intense heat and vacuum treatment, even destroyed. Therefore, the samples do not contain significant amounts of liquid-like bulk water inside the tubes, which could be removed without affecting the tube structure.

To take a closer look at molecular mobilities, ^{1}H -^{1}H DQ-filtered spectra were recorded using a back-to-back pulse sequence with various excitation times. When short excitation times are used, signals in these spectra are only observed for protons that experience

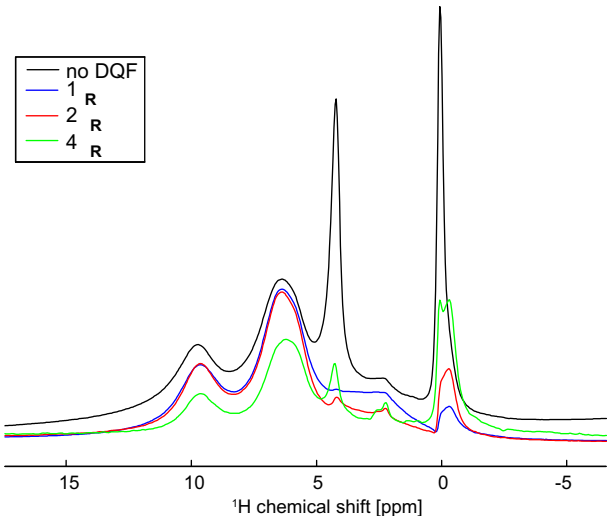

Figure 4.4: ^{1}H -^{1}H *double quantum filtered spectra of CHQ nanotubes recorded with various back-to-back excitation/reconversion times under 30 kHz MAS.*

strong homonuclear dipole-dipole couplings and, therefore, belong to immobile molecules, while the signals of mobile species are suppressed. As shown in Fig. 4.4, the two narrow lines at 4.5 ppm and -0.5 ppm basically disappear from the DQF spectrum recorded with one rotor period excitation, and only the signals of the (rigid) CHQ molecules remain. Firstly, this finding confirms the assumption that the water molecules in the CHQ crystals undergo fast reorientation motions. Secondly, the DQF spectrum provides evidence that the other narrow resonance line at -0.5 ppm also arises from a species with a pronounced mobility on the $< \mu$s timescale, as is typically encountered for solvent molecules. From the variation of the signal intensities with excitation time it becomes evident that the line at -0.5 ppm actually consists of two different resonances indicating the presence of more than one species, which differ in their motional properties as well as in their resonance frequencies.

Fig. 4.5a shows the ^{1}H -^{13}C CPMAS spectrum of the CHQ nanotubes, recorded under 30 kHz MAS. All CHQ resonances can be assigned and, as expected, agree well with the chemical shifts obtained from calculations of an isolated CHQ molecule as they do not experience large packing effects. However, a splitting of the signal originating from the aromatic carbons 2 and 6 is observed. This can be explained by the displaced π-π stacking of the CHQs in neighbouring tubes, which leads to a symmetry breaking for these carbons.

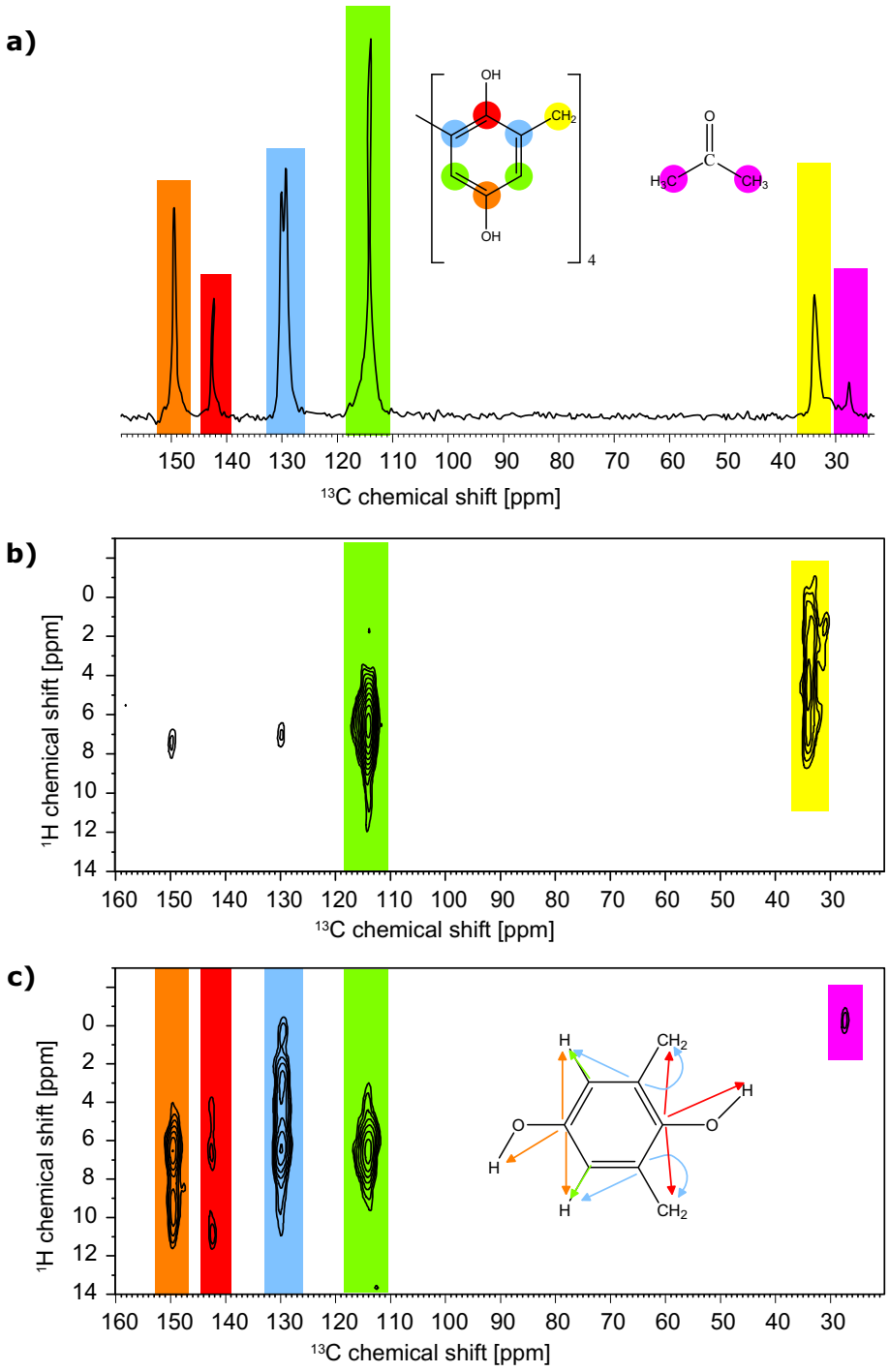

Figure 4.5: ^{1}H -^{13}C *CPMAS spectrum recorded at 30 kHz MAS (a) and* ^{1}H -^{13}C *REPT-HSQC spectra recorded under 30kHz MAS with recoupling times of one (b) and two (c) rotor periods.*

The small signal at 28 ppm cannot be assigned to any of the CHQ carbons but agrees reasonably well with the chemical shift of methyl carbons in acetone (30.6 ppm in liquid bulk acetone). The carbonyl signal of acetone is not observed in the cross-polarisation spectrum; however, in a ^{13}C NMR single pulse experiment (not shown here) a line at 210 ppm was observed that fairly agrees with the chemical shift of carbonyl in liquid bulk acetone (206.7 ppm). This suggests that acetone molecules remain in the sample even after moderate drying. After the sample was exposed to vacuum conditions, the ^{13}C signal at 28 ppm was still observed even though the ^{1}H NMR spectrum already showed degradation of the crystal structure. Thus the acetone cannot be easily removed, indicating that it is trapped inside the crystal structure.

To separate the proton chemical shifts and to gain information on ^{1}H -^{13}C proximities, heteronuclear correlation spectra were recorded using the REPT-HSQC pulse sequence. Fig. 4.5 b shows such a spectrum recorded with a recoupling time of one rotor period under 30 kHz MAS. In these spectra, peaks are only observed if the dipole-dipole interaction of the involved nuclei is strong enough, i.e. the distance of the concerned nuclei is in the range of typical CH bond distances and the molecule is immobile. The signal at 34 ppm in the direct dimension reveals that the resonances of the methylene protons are spread over a range from about 2 ppm to 7 ppm, which is in agreement with the values obtained from calculations. The correlation signal of protons directly bonded to protons in mobile species as well as long range CH contacts are only detected for longer recoupling times. In the ^{1}H -^{13}C REPT-HSQC spectrum recorded with two rotor periods recoupling time the long range contacts of the CHQs are observed, as depicted in Fig. 4.5. Additionally, a CH signal is detected at (38 ppm, -0.5 ppm) that cannot be assigned to the CHQ molecules, but is likely to originate from the acetone methyl group.

The information obtained from the ^{13}C CPMAS as well as the ^{1}H -^{13}C heteronuclear correlation spectra strongly suggest that the line observed at -0.5 ppm in the ^{1}H spectrum originates from the methyl protons of acetone molecules trapped inside the CHQ nanotubes. To verify this assumption and to ensure no other protons accidentially give rise to a resonance at the same frequency, CHQ nanotube crystals were grown from solvent mixtures with one component deuterated, i.e. D_2O/acetone and H_2O/D_6-acetone. The ^{1}H spectra of the two samples are shown in Figs. 4.6a and b, respectively. When using D_2O, the narrow signal at 4.5 ppm disappears almost completely from the ^{1}H spectrum, which again confirms the above interpretation. When growing the CHQ tubes from H_2O/D_6-acetone, the ^{1}H spectrum no longer shows the intense signal at -0.5 ppm (Fig. 4.6b), indicating that no other species gives rise to a signal at this position. Correspond-

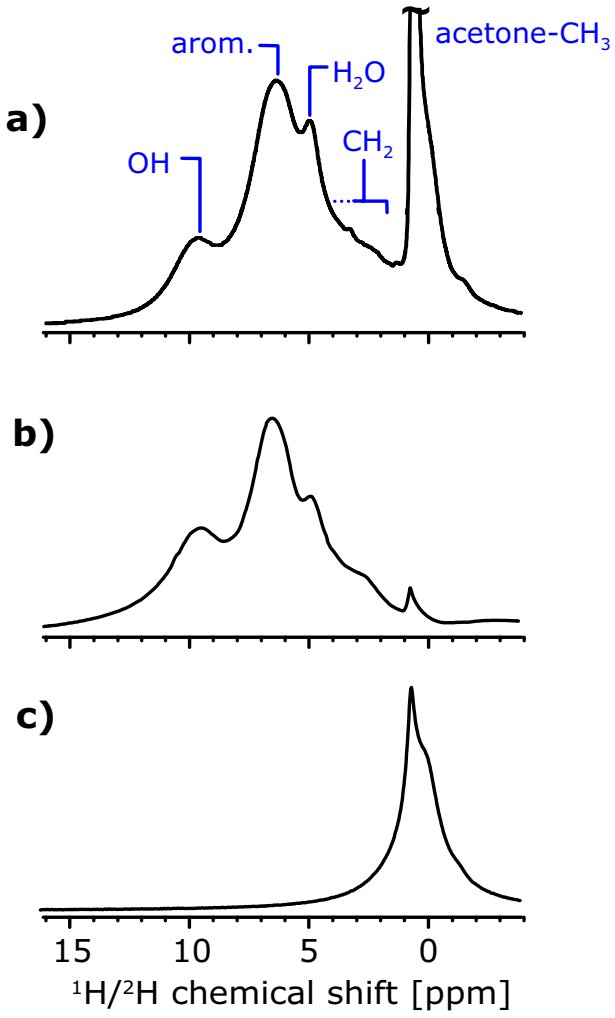

Figure 4.6: *NMR spectra recorded under 30 kHz MAS of CHQ nanotube crystals grown from solvent mixtures with one component deuterated. (a) ^1H MAS spectrum of CHQ tubes grown from D_2O/acetone. (b) ^1H MAS spectrum and (c) ^2H MAS spectrum of CHQ tubes grown from H_2O/D_6-acetone.*

ingly, the ^{2}H spectrum of the same sample exhibits exactly (and only) this signal (Fig. 4.6c), which provides clear evidence that the peak at -0.5 ppm arises from the methyl groups of acetone. Interestingly, for various samples grown from H_2O/D_6-acetone mixtures, the water resonance at about 4.5 ppm was found to be strongly reduced, too. This effect is provisionally ascribed to chemical proton-deuteron exchange processes which are discussed later in this section.

Thus, it can be concluded that acetone is present in the CHQ nanotube crystals. The

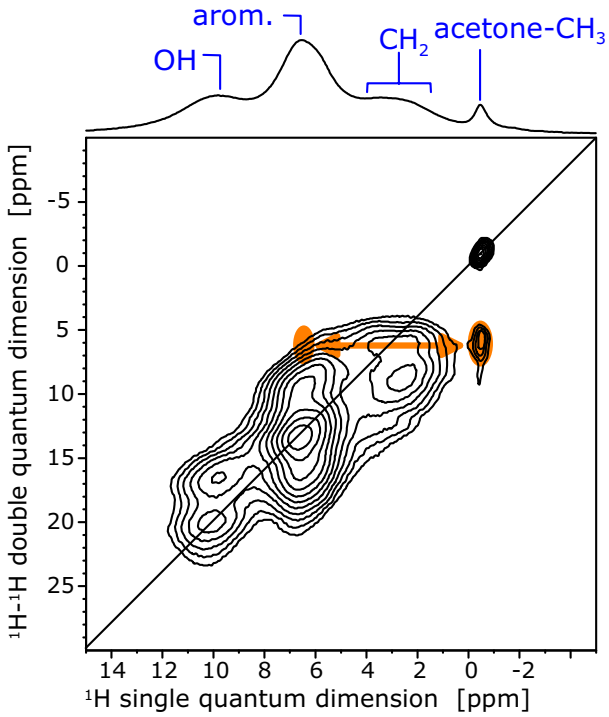

Figure 4.7: *^1H -^1H double-quantum (DQ) NMR spectrum of CHQ nanotube crystals, recorded under 30 kHz MAS using one rotor period of back-to-back recoupling for excitation and reconversion of the DQ coherences.*

acetone molecules are partially mobile, but occupy an average position at which they experience aromatic ring current effects that cause an upfield shift of their signal by about -2.5 ppm. Recalling the typical shielding effects of benzene rings, this implies a position of the acetone methyl groups above (and not beside) the aromatic ring planes, which indicates that the methyl groups stick inside the CHQ bowls.

To verify this assumption and exclude the possibility that the acetone and the tubes form separated phases in the crystal, a two-dimensional ^{1}H -^{1}H DQ spectrum was recorded that provides information of spatial proximities in the sample. The DQ signals are indicative for proton-proton distances below 4 Å in rigid systems, when the experiment is performed under fast MAS conditions with short excitation times (i.e. $\leq$ one rotor period) [Schnell 01a]. The ^{1}H -^{1}H DQ spectrum of the CHQ tubes recorded with one rotor period excitation under 30 kHz MAS (Fig. 4.7) clearly shows a DQ signal which involves the acetone methyl protons and the CHQ phenyl protons. Thus, the acetone molecules do not form a separated phase, but are in close contact with the aromatic rings in the CHQ nanotube. This is in accordance with the results from X-ray diffraction,

which showed that the crystalline needles are in fact single crystals.

4.1.3 Calculations of Acetone Trapped in the Nanotubes

The solid-state NMR measurements presented in the last section provide clear evidence that acetone molecules are trapped inside the CHQ bowls of the nanotubes. Such trapping phenomena are very well known in the context of calix[4]arenes [Namor 98, Ikeda 97, Ungaro 84, Lu 99, Lu 00].

Based on these observations, a geometry optimisation of an acetone molecule placed inside a CHQ bowl was performed by Dr. Daniel Sebastiani. As one proton of the water molecules in the chain of hydrogen-bonds is dangling freely into the tube, the oxygen of the acetone is likely to form a hydrogen bond with that "free" proton. A part of the one dimensional array of hydrogen bonds was therefore included in the geometry optimisation (see Fig. 4.8 a). From energy calculations a full adsorption energy of 68 kJ/mol was found, which is sufficiently strong to support the hypothesis of a preferential position of the acetone molecules in the center of the CHQ bowls (For a detailed description see Appendix B). This is in agreement with recent findings of Ripmeester et al. [Udachin 03], where trapping of acetone molecules inside *p-tert*-butylcalix[4]arenes was obseved in solution. In this work, the acetone carbonyl and methyl ^{13}C chemical shifts were found to be shifted upfield to 201 ppm and 25 ppm, respectively, compared to the values of liquid bulk acetone of 206.7 ppm and 30.7 ppm. As mentioned before, about the same effect was observed for the acetone molecules trapped inside the CHQ nanotubes.

To calculate the ^{1}H chemical shifts, four acetone molecules were placed inside a unit cell, which corresponds to filling the CHQ bowls with one acetone molecule each (see Fig. 4.8 b). Their exact positions were slightly randomized to yield a better statistics of the chemical shifts, which were subsequently averaged. The calculated ^{1}H spectrum is shown in Fig. 4.8 d. To account for molecular mobilities, the parameters were averaged over all protons belonging to the same acetone and water molecule, respectively, and little Gaussian broadening was applied to these lines. In comparison to the spectrum calculated without acetone (Fig. 4.3b), three major differences are obvious: *(i)* The methyl protons of acetone give rise to an additional resonance line at -0.7 ppm, which fully reproduces the experimental observation (see Fig. 4.8c). *(ii)* For water molecules with and without acetone being hydrogen-bonded to them, different average ^{1}H shifts of 6.8 and 5 ppm, respectively, are found. Without acetone, averaging takes place between two shifts of about 8.5 and 0.5 ppm for hydrogen-bonded and free protons, respectively, as discussed

Table 4.1: *Experimental and calculated values of the ^1H NMR chemical shifts of the CHQ tubes, along with those of the inserted acetone. The presence of several values for a single atom type indicates topologically different atoms of the same molecule.*

	experimental chemical shift [ppm]	calculated chemical shift empty tube [ppm]	calculated chemical shift tube with acetone [ppm]
CHQ-aliphatic	2.0-7.0	1.5; 3.0; 5.0	1.5; 3.0; 5.0
CHQ-aromatic	6.5	5.6	5.6
CHQ rim-OH	10.0	11.7	11.3
CHQ bottom-OH	10.0	10.4	11.6
H_2O	4.5	1.5; 8.3	1.5-10
Acetone CH_3	-0.5	-	-0.7

above. With acetone, both water protons have chemical shifts of 6...7.5 ppm, because the hydrogen bond of one water proton to the acetone carbonyl oxygen weakens the other two hydrogen bonds in which the water molecule is involved in the one-dimensional chain. This is in agreement with the observations described earlier, that for various samples the position of the water resonance was found at slightly different positions. *(iii)* The shifts of the hydroxyl protons are affected by the acetone through a weakening of the rim-OH network, causing a slight geometrical rearrangement and, in particular, a strengthening of the bottom -OH hydrogen-bonds.

4.1.4 Mobility of Acetone Studied by ^2H NMR

As described above, the ^1H -^1H DQF spectra reveal the existence of two acetone resonances with slight differences in chemical shifts and the underlying mobilities. To further investigate the mobilities, ^2H NMR experiments were carried out on CHQ nanotubes crystallised from a water/D_6-acetone mixture. As the quadrupole coupling constant of solid bulk acetone (where only methyl rotation occurs) is known to be $\frac{\delta}{2\pi} = 40$ kHz [Udachin 03], the coupling constant of acetone molecules trapped in the CHQ nanotubes provides information on the mobility of the molecules. Fig. 4.9 shows a sideband spectrum of a sample recorded under 4 kHz MAS. The signal can be decomposed into a line with intensity mainly in the centreband arising from a very mobile species, and a second component that exhibits sidebands up to fourth order and belongs to a species with rather low mobility. The two components can be separated by applying a double quantum filter that supresses the ^2H signal arising from the mobile component as shown in Fig. 4.9.

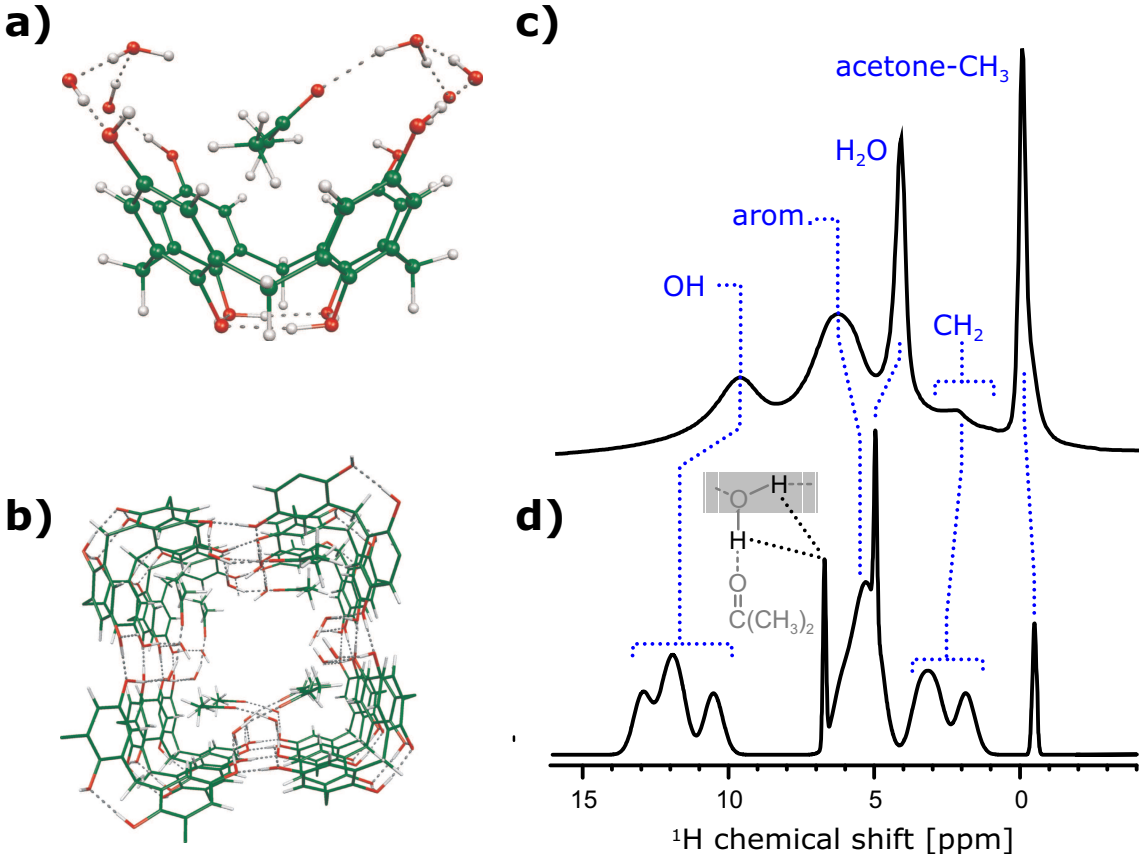

Figure 4.8: *(a) Representation of a bowl-shaped CHQ molecule taken out of the nanotube crystal structure (i.e. with hydrogen-bonded water molecules attached). An acetone molecule is trapped inside the CHQ bowl with its carbonyl oxygen hydrogen-bonded to a water proton. (b) CHQ nanotube crystal structure filled with acetone molecules. (c) Experimental ^1H spectrum of CHQ nanotube crystals. (d) Calculated spectrum of the CHQ nanotubes filled with acetone molecules. All chemical shifts of acetone-methyl and water protons have been averaged. Different Gaussian line broadening was applied for the signals of rigid (nanotube) and mobile (water, acetone) atoms.*

Surprisingly, in a static spectrum of the sample (see Fig. 4.10) a third component was observed that gives rise to a PAKE pattern of approximately 120 kHz width. This spectrum was recorded several weeks after the preparation of the sample and from a ^2H spectrum recorded under 30 kHz MAS it becomes clear that proton-exchange had occured in the meantime, leading to deuteration of the CHQ carboxyl groups as well as the water molecules. This phenomenon will be further discussed in the following section. Fig. 4.11 shows a sideband pattern recorded under 25 kHz MAS as well as a simulated spectrum

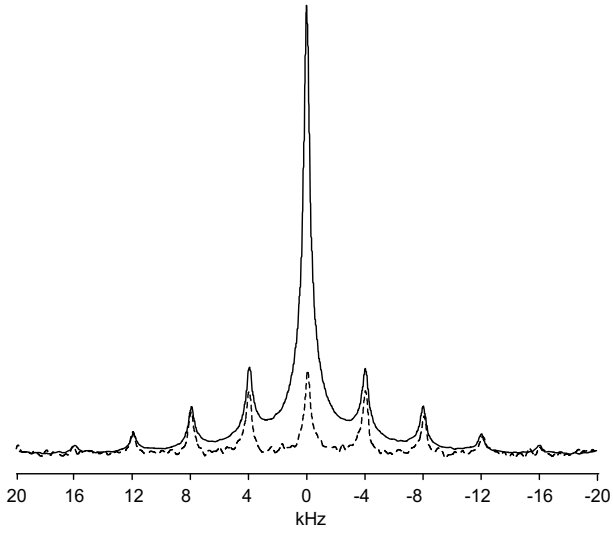

Figure 4.9: *^2H NMR spinning sideband spectrum of CHQ nanotubes crystallised from a water/D_6-acetone mixture recorded under 4 kHz MAS, with (dotted line) and without (solid line) use of a ^2H double-quantum filter*

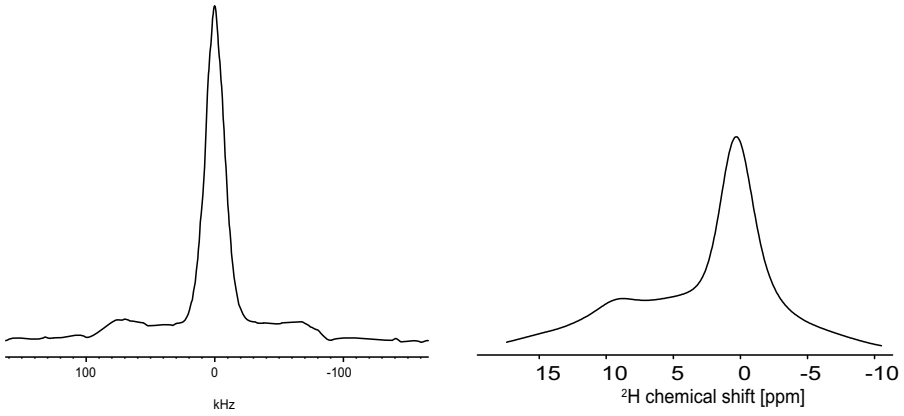

Figure 4.10: *Static ^2H NMR spectrum (a) and ^2H spectrum recorded under 30 kHz MAS (b) of CHQ nanotubes crystallised from a water/D_6-acetone mixture several weeks after preparation of the sample.*

with $\frac{\delta}{2\pi} = 120$ kHz that matches the sideband pattern of the line at 10 ppm. This indicates that the broad pattern in the static spectrum originates from the CHQ hydroxyl deuterons which are rather immobile. The static spectrum arising from acetone, however, does not resemble a Pake pattern, indicating a distribution of mobilities of the acetone molecules. Both, the foot of the static line as well as the DQ-filtered sideband pattern, have a width of approximately 40 kHz, indicating that the largest quadrupole coupling of

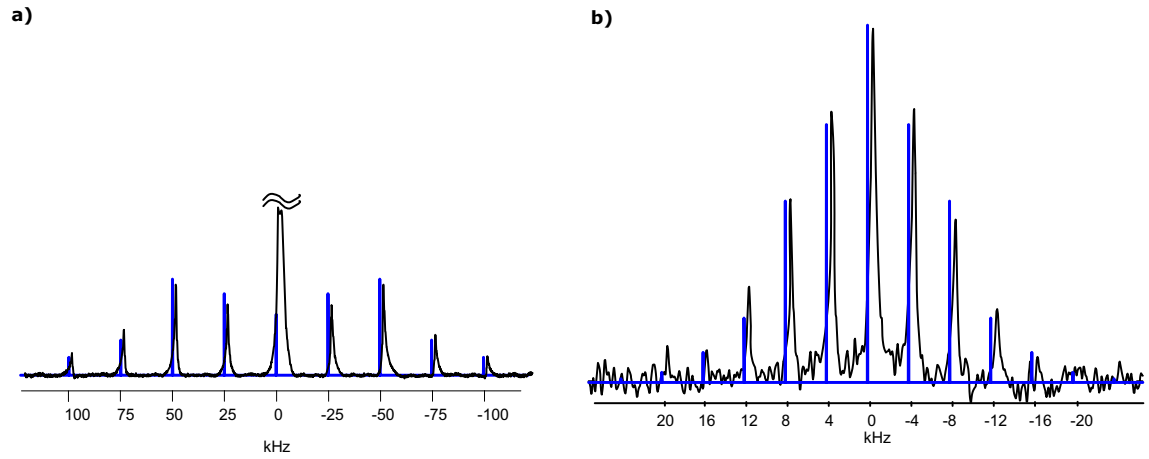

Figure 4.11: *Experimental (black) and simulated (blue) sideband patterns. (a)* ^2H *sideband pattern of the carboxyl group of the CHQ recorded under 25 kHz MAS; simulation with* $\frac{\delta}{2\pi} = 120$ *kHz. (b) DQ-filtered* ^2H *sideband pattern of the acetone methyl group of the CHQ recorded under 4 kHz MAS; sum of simulations with* $\frac{\delta}{2\pi} = 10\ kHz$ *and* $\frac{\delta}{2\pi} = 20$ *kHz.*

the deuterons in acetone is about $\frac{\delta}{2\pi} \approx 20$ kHz. As the mobility of the acetone molecules seems to be distributed over some range and there is no reason to assume any special distribution, no unique quadrupole coupling constant can be extracted from the DQ filtered sideband pattern. Rather, the sum of two simulated spectra with $\frac{\delta}{2\pi} = 20$ kHz and $\frac{\delta}{2\pi} = 10$ kHz, respectively, agrees fairly well with the experimental spectrum (see Fig. 4.11). This implies that the quadrupole coupling adopts values in this range.

Turning to molecular motions potentially responsible for the observed couplings, a fast exchange of the positions of the methyl groups (i.e., a 180° jump of the acetone around the C=O bond) would yield a reduction of the quadrupole coupling to $\frac{\delta}{2\pi} \approx 20$ kHz. Hence, some of the trapped acetone molecules can be assumed to perform only this motion. A further reduction of the quadrupole coupling constant requires additional motion. From ^{2}H NMR experiments carried out on acetone trapped in *p-tert*-butylcalix[4]arene [Udachin 03] it is known that an additional exchange of positions of the external methyl and the carbonyl group leads to $\frac{\delta}{2\pi} \approx 10\ kHz$. In the CHQ nanotubes the carbonyl group is hydrogen bonded to the 1D array of hydrogen-bonds and, thus, this exchange is constrained. Slight variations in the chemical environment of the acetone and, thus, the topology of these hydrogen-bonds might be an explanation for the observed distribution of quadrupolar couplings.

The highly mobile species that is supressed in the DQ-filtered experiment exhibits quadrupole

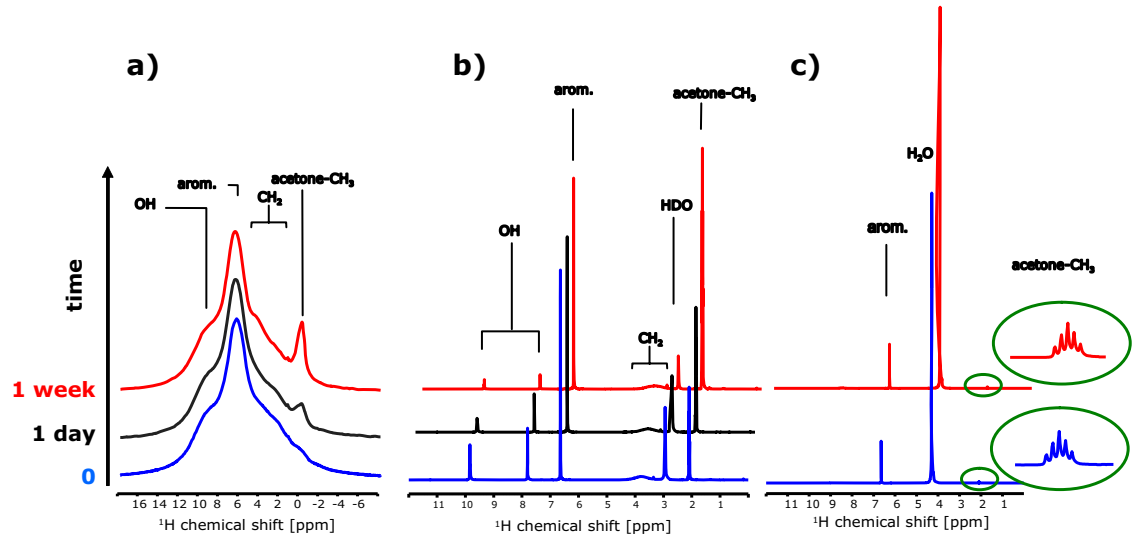

Figure 4.12: ^1H *NMR spectra recorded at different times after sample preparation. (a) solid-state NMR spectra of CHQ nanotubes crystallised from a water/D_6-acetone mixture, (b) solution NMR of CHQ in D_6-acetone, (c) solution NMR of hydroquinone in a water/D_6-acetone mixture.*

couplings $\frac{\delta}{2\pi} < 10$ kHz. At the same time, the line is only shifted upfield by about 2 ppm (compared to 2.5 ppm for the other line). This suggests that some of the acetone molecules are placed less deep inside the CHQ bowls and therefore experience smaller shift effects and retain a higher mobility.

4.1.5 Proton Exchange in CHQ Nanotubes

As mentioned above, the samples crystallised from solvent mixtures with one component deuterated showed a slow proton exchange. In the ^{1}H NMR spectra of a sample crystallised from a water/D_6-acetone mixture the integrated intensitiy of the signal arising from the acetone methyl protons is found to increase with time (Fig. 4.12 a). The same observation is made for a solution of CHQ molecules in acetone, while, for hydroquinone dissolved in a water/D_6-acetone mixture no proton exchange was observed. The trapping of acetone in the CHQ bowls seems to have a catalytic effect on the keto-enol-tautomery in that it stabilises the much less favorable enol form through hydrogen-bonding to the carbonyl oxygen. This effect is preserved in the CHQ nanotube crystals. Theoretical investigations concerning the mechanism of this exhange are currently underway.

4.2 C_3-Symmetrical Discs

In the field of discotic liquid crystals helical structures are of particular interest, as chiral liquid crystals are one of the few organic materials frequently applied in electronic devices. The building blocks usually consist of a rigid core and flexible sidechains. One major goal is the development of larger rigid cores to enhance the temperature range of liquid crystallinity. To obtain helical structures in a self-assembly process, the building blocks must induce helicity. This is usually achieved by attaching chiral sidechains to the core, but can also originate from secondary interactions, such as π-π-stacking and hydrogen bonding, or from the structure of the core itself. To invesitgate the influence of the different secondary interactions, discotic liquid crystals with various sidechains and cores usually need to be synthesised. The stacking geometry is commonly investigated by X-ray diffraction. However, detailed information on the core geometry and mobility is usually not accesible from X-ray data. In the following sections, a combination of solid-state NMR measurements and quantum-chemical calculations carried out on C_3-symmetrical discs will be described that provide information on the origin of helicity in a system of C_3-symmetrical discs described in the following section.

4.2.1 Structure of the C_3-symmetrical Discs

Meijer et al. [Palmans 97, Gorp 05] synthesized bipyridinyl-based C_3-symmetric discs that exhibit a helical structre even when equipped with achiral sidechains. As depicted in Fig. 4.13, the bipyridinyl parts are planar due to intramolecular hydrogen bonds, leading to an extended core size. The gallic moieties are equipped with alkyl chains, inducing phase separation. From X-ray investigations [Gorp 05] it is known that discs carrying achiral alkyl sidechains assemble in helical columnar stacks with an inter-disc distance of 3.3 Å and a helical pitch of 17.6 Å. In the case of chiral sidechains, a small change in the stacking geometry is observed, leading to an inter-disc distance of 3.5 Å and a helical pitch of 17.4 Å. In the stacks, the discs obtain a propeller like structure that is assumed to arise from intermolecular hydrogen bonding between the central benzene-1,3,5,-tricarboxamide units [Gorp 05]. The X-ray data on which this assumption is based, however, does not directly prove the existence of such inter-disc hydrogen-bonds.

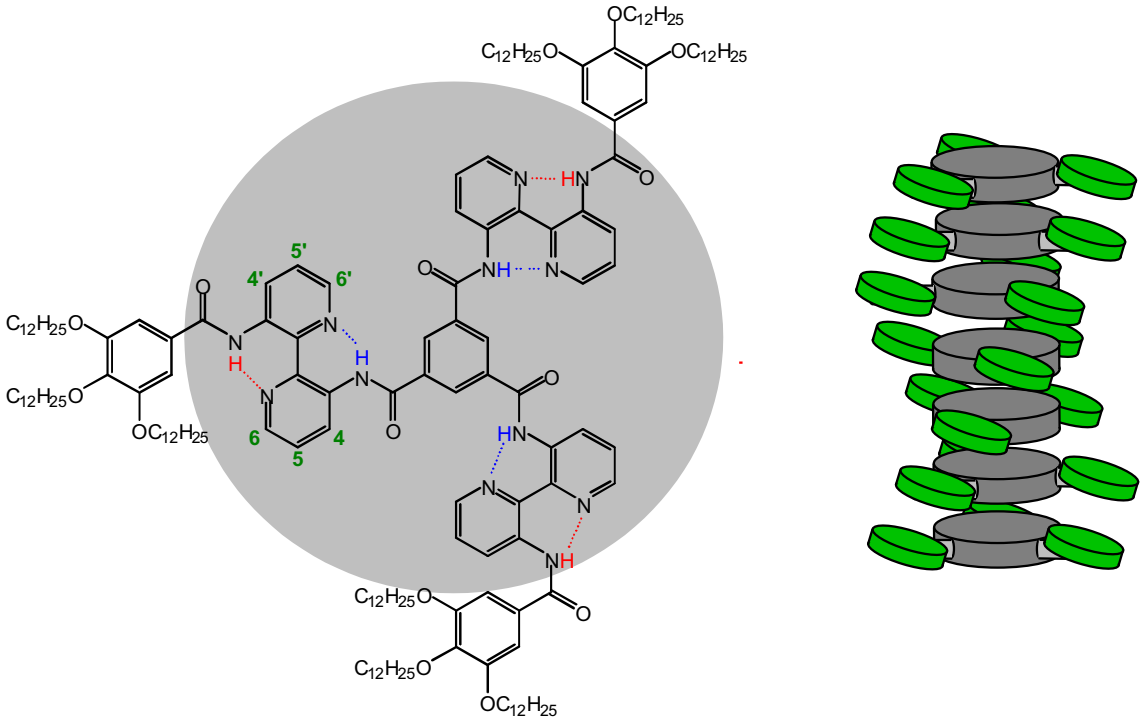

Figure 4.13: *Bypiridine-based C_3-symmetrical disc and illustration of the helical stacking of the propeller-like structures.*

4.2.2 Solid-State NMR

Information on packing in solids can be obtained by comparing ^{1}H NMR shifts found in solid state NMR with the shifts observed in dilute solutions. While the chemical shifts in solution mainly arise from the electronic structure of the molecule, in the solid state also other molecules take effect on the observed shifts. For the C_3-symmetrical discs, the π-π-stacking of aromatic rings is expected to result in π-shifts of the proton resonances due to aromatic ring current effects. The solid state ^{1}H NMR spectrum of the discs (see Fig. 4.14) is dominated by a large alkyl peak originating from the side chains and two low-field NH shifts (δ = 13 ppm and δ = 13.8 ppm) are observed. Comparing these with the shifts obtained from solution NMR [Palmans 97] (δ = 14.36 ppm and δ = 15.49 ppm) reveals large upfield shifts of more than 1 ppm, indicating π-π stacking effects or differences in the hydrogen-bonds in the solid and in solution. A similar but weaker effect is obtained for the OCH protons that experience a high-field shift of about 1 ppm from 4.05 ppm in the solution to 3.2 ppm in the solid-state spectrum. The signals of the aromatic protons overlap and can therefore not be readily assigned. However, packing

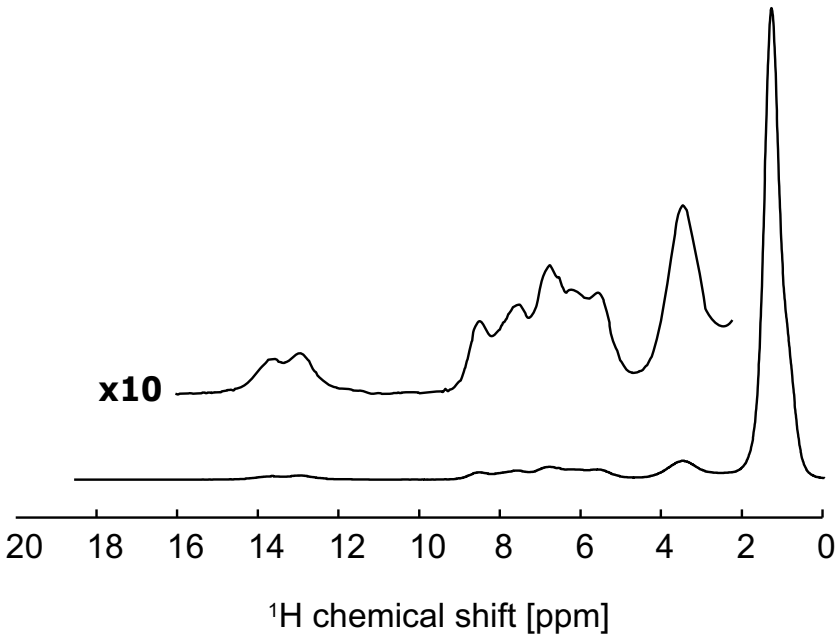

Figure 4.14: ^1H *NMR spectrum of the discs recorded under 30kHz MAS.*

effects are still observed, as in the solid state spectrum all aromatic resonances occur in the range of 5 ppm to 9 ppm, while in solution shifts from 7 ppm to 9.6 ppm are obtained for the aromatic protons.

To gain information on proton-proton proximities, a two dimensional double-quantum (DQ) spectrum was recorded under 30 kHz MAS, using the back-to-back pulse sequence with an excitation/reconversion time of one rotor period. For this rather short excitation time, DQ coherences are only observed if the dipole-dipole couplings of the respective nuclei are strong enough, i.e the nuclei are not further apart than approximately 4 Å. As can bee seen in Fig. 4.15a, the huge alkyl peak leads to severe phase distortions in the double-quantum spectrum which makes it difficult to tell whether the peaks are due to DQ coherences or only artifacts arising from the phase distortions caused by the alkyl signal. To overcome this problem WATERGATE peak suppression was utilized, a technique well-known from liquid NMR that has been adapted to solid-state NMR under MAS [Fischbach 03b]. The spectrum recorded with WATERGATE suppression of the alkyl peak (Fig. 4.15 b) appears much cleaner than the usual DQ BABA spectrum, as the phase distortions arising from the alkyl peak are well below the intensity level of the peaks of interest. The NH-alkyl cross peak confirms the assumption that this resonance originates from the outer NH protons. In the aromatic region, strong cross peaks originating from neighbouring aromatic protons are observed, but still the resolution is too

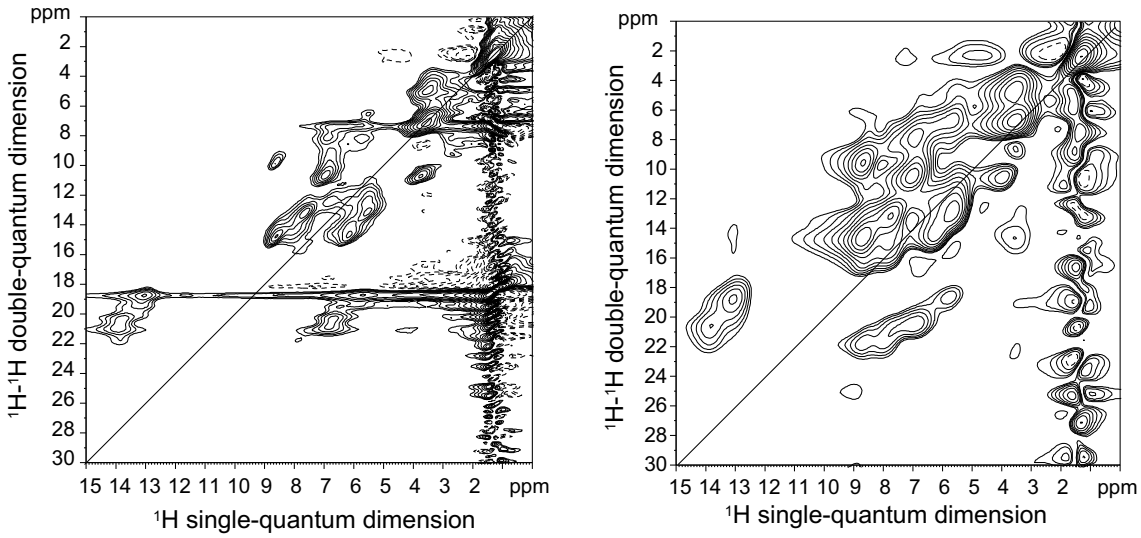

Figure 4.15: *^{1}H -^{1}H double-quantum (DQ) NMR spectrum of C_3 symmetric discs, recorded under 30 kHz MAS using one rotor period of back-to-back recoupling for excitation and reconversion of the DQ coherences without (a) and with (b) WATERGATE supression of the alkyl signal.*

low to unambibiously assign all protons.

To separate the ^{1}H chemical shifts, a ^{1}H -^{13}C correlation spectrum was recorded using one rotor period excitation time. Spectra of this kind benefit from the better resolution achievable for ^{13}C and allow for the separation of ^{1}H resonances, since peaks are only observed for directly ^{13}C -bonded protons. The protons bonded to the outer aromatic rings give rise to signals at (6.8 ppm / 108 ppm) and (5.6 ppm / 104 ppm), showing a highfield shift as compared to the ^{1}H chemical shift of 7.2 ppm obtained from solution NMR. By comparison with the solution ^{13}C chemical shifts, the solid state ^{13}C resonances and, thus, the proton resonances can partially be assigned, but a complete assignment is not possible, since some of the ^{13}C resonances overlap and the ^{1}H chemical signals show large shifts due to packing effects. The size of these effects for the various positions in the molecules sensitively depends on the geometry and is therefore not known. Even combining the information of the ^{1}H -^{1}H DQ spectrum and the ^{1}H -^{13}C -correlation spectrum does not lead to an unambigious resonance assignment, since especially the ^{1}H resonances differ only very little when compared to the experienced π-shifts.

In a quantitative analysis of the ^{1}H -^{13}C dipole-dipole interaction performed by Almut Rapp [Rapp 04], dipole-dipole coupling constants of $\frac{D_{ij}}{2\pi} = 20.5$ kHz were obtained for the aromatic CH groups at the biphenyl rings and the central aromatic ring, which

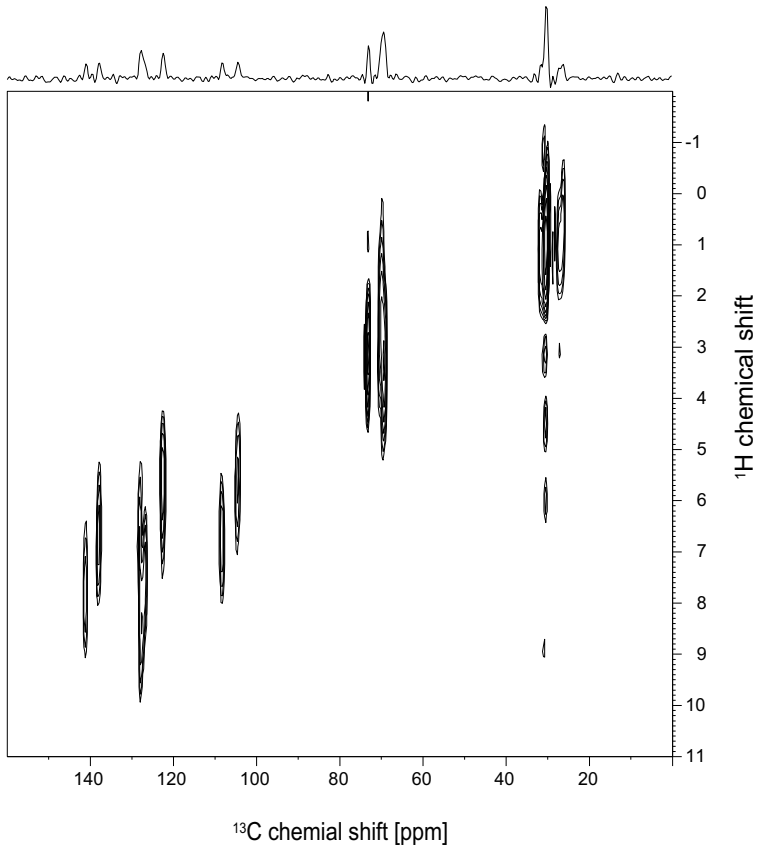

Figure 4.16: ^1H -^{13}C *correlation spectrum (REPT-HSQC) of the* C_3*-symmetrical discs recorded under 30kHz MAS with an excitation time of one rotor period.*

agrees with the typical value for immobile segments. Hence, as expected the N-H$\cdots$H hydrogen-bonds prevent aromatic ring flips. In addition, it can be concluded that there is no rotation of the discs in the stack. For the outer aromatic rings, a dipole-dipole coupling constant of $\frac{D_{ij}}{2\pi} = 20.5$ kHz was obtained, indicating a small angle motion of the rings with a mean excursion of $\pm 15°$, while a full rotation or a ring flip can be excluded.

4.2.3 Quantum Chemical Calculations

Ab initio calculations were performed by Thorsten Metzroth (University of Mainz) using the program package TURBOMOLE [Ahlrichs 89] (see Appendix B).

For the calculations, a simplified model depicted in Fig. 4.17 was used, in which the gallic moieties equipped with dodecyl sidechains in 3,4,5 position were ignored and replaced by protons. This approach is in so far feasible as from X-ray investigations it is known that

the sidechains have only minor influence on the stacking geometry (inter-disk distance and helical pitch). This keeps the calculation time reasonably short and also avoids the problem of choosing an appropriate conformation for the alkyl chains.

First, the geometry of the monomer was optimised on the DFT (B-LYP) [Parr 89, Becke 88, Lee 88] and MP2 [Moeller 34] level of theory, employing an SVP [Schäfer 92] basis set and the resolution of identity (RI) technique [Eichkorn 95]. Both methods yield a monomer geometry with the plane of the biphenyl groups slightly twisted with respect to the aromatic core plane. Thus, the propeller-like structure of the core observed in the stacks is already found for the monomer.

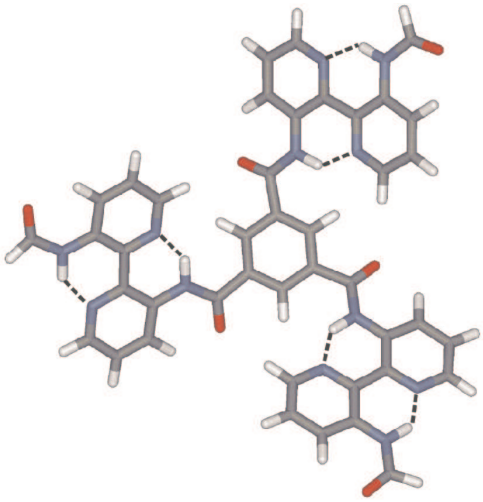

Figure 4.17: *Simplified model of the C_3 symmetrical disc as used for quantum chemical calculations.*

To investigate the rotational displacement of two adjacent layers, a dimeric system was built by placing two optimised monomers at the inter-disc distance distance as obtained from X-ray data [Gorp 05]. The energy of the aggregate was calculated for a series of torsion angles that were set manually. From the resulting energy profile (depicted in Fig. 4.18) the torsion angle was estimated to be $28° \pm 5°$. This corresponds to an approximate helical pitch of 15 Å $\pm$ 3 Å, which is consistent with the values obtained from the X-ray investigations described above. The differences in the helical pitch for systems with chiral and achiral sidechains is about one order of magnitude smaller than the error of the calculations and as the minimum in the energy profile is rather flat, an influence of the sidechains in this order of magnitude seems plausible.

NMR chemical shifts were computed at the DFT(B3-LYP)/SVP level [Becke 93] for the monomer and for a trimer which was obtained by stacking three molecules twisted by the torsion angle known from the energy profile. The chemical shifts were referenced to TMS calculated under the same conditions.

As expected, the comparison of the ^{1}H chemical shifts of the single molecule and the middle molecule of the trimer reveals large π-shifts due to packing effects. From previous studies, these effects are known to be long-ranged [Ochsenfeld 01]. In a study carried out on hexa-*peri*-hexabenzocoronenes [Fischbach 03a], convergence of the chemical shifts was

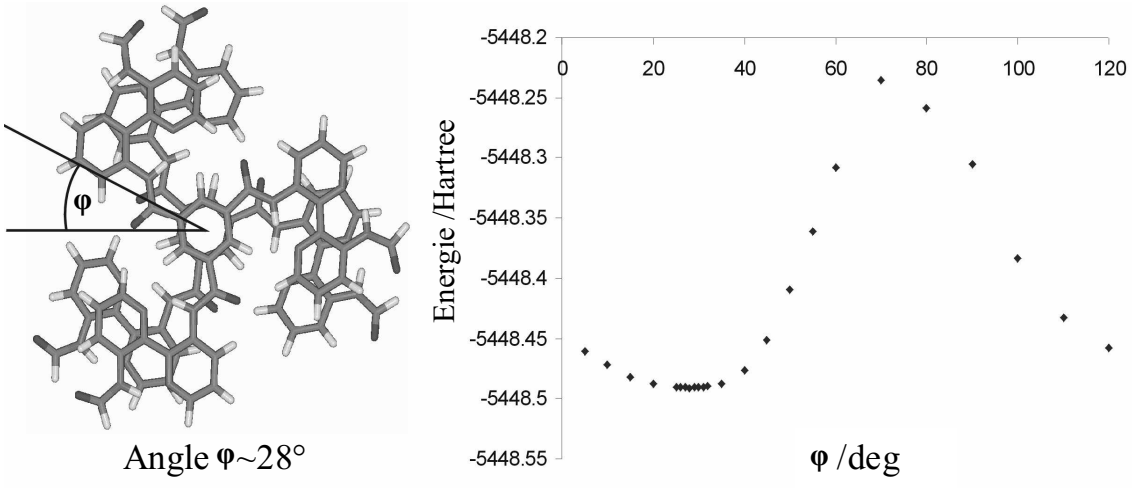

Figure 4.18: *(a) Dimer at the angle corresponding to the lowest energy and (b) dependence of the relative energy on the torsion angle.*

found for a stack of seven molecules, meaning that third-nearest neighbours still have a significant influence on the chemical shielding. Thus, the ^{1}H chemical shifts obtained for the trimer are not expected to match the experimental values, but to represent the principal trend.

4.2.4 Comparison of Experimental and Calculated Chemical Shifts

Combining the calculated chemical shifts and the information on direct bonding of protons and carbons derived from the heteronuclear correlation spectrum, all ^{13}C and ^{1}H resonances could be assigned (see Table 4.2). This assignment was then verified by turning back to the ^{1}H -^{1}H DQ spectrum. All cross peaks expected from close neighbour contacts in the molecular structure are observed in the spectrum (e.g., the neighbouring aromatic protons: 4-5, 5-6, 4'-5',5'-6') and all peaks found in the spectrum can be explained by spatial proximities in the structure. The auto-peak observed at 6.3 ppm confirms the assignment of the proton of the central aromatic ring, since for two neighbouring molecules the distance of these protons is only 3.6 Å. For all other protons, the helical arrangement of the molecules in the stack leads to larger intermolecular distances. This effect is naturally stronger for the outer positions in the molecules and, when taking a closer look at the DQ spectrum, two weak auto peaks are observed for the protons at

Table 4.2: *^{1}H and ^{13}C chemical shifts calculated for the monomer and the central molecule of the trimer, and experimental values obtained from solid-state NMR (all given in ppm).*

	monomer	trimer	···	solid	monomer	trimer	···	solid
ortho	9.5	8.5	···	6.7	130	131	···	128
4	10.1	9.7	···	7.3	127	126	···	127
5	7.1	6.7	···	5.7	122	121	···	122
6	7.9	7.6	···	6.7	135	135	···	138
4'	9.7	9.7	···	8.7	127	127	···	128
5'	7.2	7.0	···	6.0	123	122	···	122
6'	9.3	8.6	···	7.8	138	141	···	141
NH	16.5	16.0	···	13.8	-	-		-
NH'	14.6	13.8	···	13.0	-	-		-

positions 4 and 6' as well as for the inner NH, all of which are situated close to the center. In a DQ spectrum recorded with a longer exitation time of $\tau = 2\tau_{\mathrm{R}}$ (not shown here) the intensities of these auto peaks increases, confirming the stacking geometry.

As can be seen from Table 4.2 the proton chemical shifts experience strong packing effects. To visualize these effects, Fig. 4.19 shows the calculated spectra for the monomer and the trimer structure as well as the experimental solid-state ^{1}H NMR spectrum. Due to packing effects, the spectrum computed for the trimer strucuture is clearly shifted upfield as compared to the monomer spectrum. As expected, these effects are even larger for the experimental spectrum, as π-shifts can also be induced by second and third nearest neighbours. Due to the helical arrangement of the molecules the influence of second next neighbours is larger for protons close to the center of the molecule. As the C_3-symmetrical discs have a tendency to aggregate in solution the variation of the chemical shifts with the size of the stacks can be monitored in concentration-dependent solution NMR measurements. Meijer et al. report that, as expected, on going from lower to higher concentrations all aromatic peaks experience highfield shifts, and this effect is most pronounced for the protons in the interior of the molecule [Palmans 97].

In essence the combination of NMR experiments and quantum-chemical calculations provides a constistent picture of the molecular and stacking geometry. However, no evidence for intermolecular hydrogen-bonding was found and, in fact, for the obtained structure their existence seems highly improbable, as the intermolecular NH$\cdots$O distances are rather large. Yet, from the presented calculations it is evident that the helical arrangement of the stacks arises from the conformation of the molecules and, hence, from

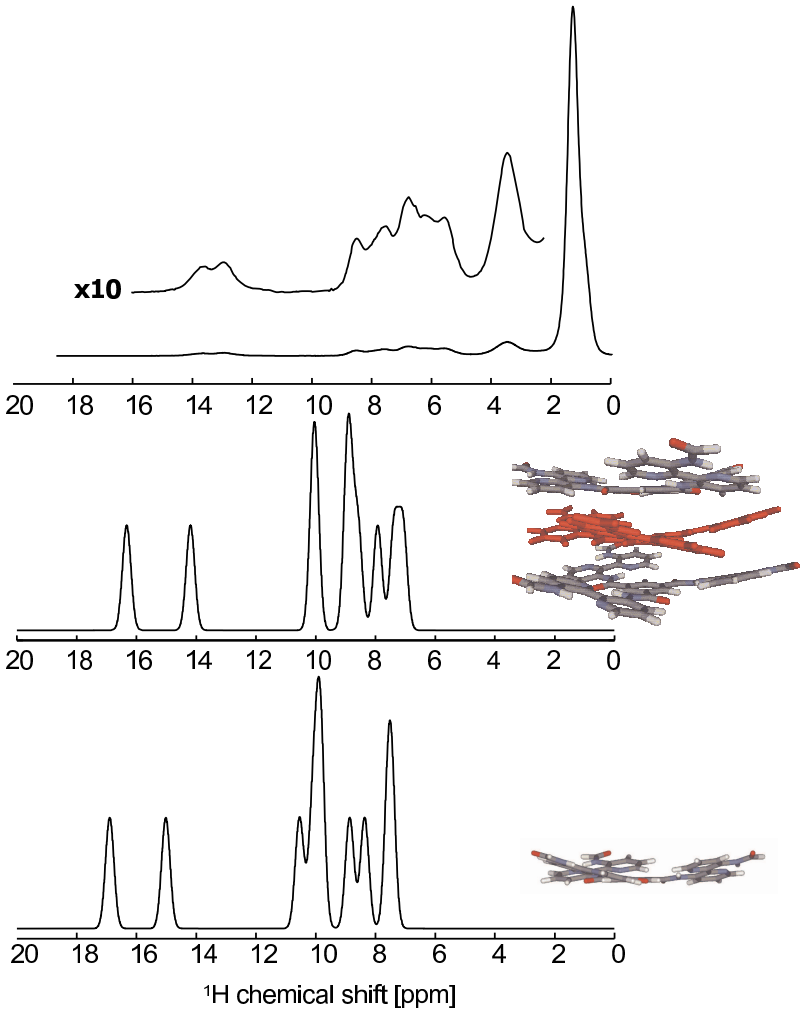

Figure 4.19: ^1H *NMR spectrum of the discs recorded under 30kHz MAS (a).* ^1H *NMR spectra calculated for the central molecule of the trimer (b) and the monomer (c). Gaussian line broadening was applied to the calculated spectra.*

the geometry of the core and does not require the presence of additional intermolecular hydrogen-bonds for stabilisation.

4.3 Discussion

The two examples presented in this chapter show that the combination of NMR experiments and quantum-chemical calculations can provide substantial information on supramolecular assemblies that is presently not accessible by other methods.

For the calix[4]hydroquinone nanotubes, ^{1}H and ^{2}H solid-state MAS NMR spectra and DFT calculations confirm that water molecules link the CHQs through extended one-dimensional chains of $\cdots$O–H$\cdots$ hydrogen bonds. In addition, the investigations proved that acetone is trapped in the CHQ bowls inside the tubes and, moreover, attached to the extended hydrogen-bonded chain via a carbonyl-water hydrogen-bond. Both water and acetone molecules undergo fast reorientation motions in the course of which their protons interchange their positions and average their chemical shifts. A ^{2}H NMR study of this motional process, performed on a sample prepared from D_6-acetone, revealed that some of the acetone molecules are placed deeply inside the CHQ bowls and perforn a 180° jump around the C=O bond, while others are placed less deep inside the CHQ bowls and therefore show a higher mobility.

The investigations on the C_3-symmetric disc confirmed the helical stacking arrangement known from X-ray investigations. However, the assumption that the helicity is induced by intermolecular hydrogen-bonds was not confirmed, rather, the propeller-like geometry of the core is the origin of helicity in these systems. In the stacks, ^{1}H chemical shifts experience large π-shifts due to packing effects that were found to be long-ranged. The influence of packing effects on ^{13}C chemical shifts is on the same order as for ^{1}H chemical shifts (in ppm) and therefore relatively small. However, the combination of ^{13}C chemical shifts obtained from quantum-chemical calculations and experimental ^{1}H -^{13}C correlation spectra has proven to be particularily helpful to assist the proton assignment.

Chapter 5

Summary

In this work, solid-state NMR methods suitable for the investigation of supramolecular systems were developed and improved. In this context, special interest was focused on non-covalent interactions responsible for the formation of supramolecular structures, such as π-π interactions and hydrogen-bonds.

In the first part of this work (chapter 3), solid-state NMR methods were presented that provide information on molecular structure and motion via the investigation of anisotropic interactions, namely quadrupole and dipole-dipole couplings, under magic-angle spinning conditions.

As described in chapter 3.1, a two-dimensional ^{2}H DQ experiment was developed, which is performed under off magic-angle conditions and correlates ^{2}H isotropic chemical shifts with quasistatic DQ-filtered line shapes. From the latter, the quadrupole coupling parameters of samples deuterated at multiple sites can be extracted in a site-selective fashion. Such samples can easily be prepared by recrystallisation from deuterated solvents capable of exchanging their deuterons with the solubilised material, whereby the acidic protons (which usually includes all protons forming hydrogen bonds) are replaced by deuterons. It was also found that ^{2}H MAS NMR spectra, when recorded in a rotor-synchronised fashion, resemble ^{1}H MAS NMR spectra in terms of isotropic chemical shifts and spectral resolution. Therefore, ^{2}H MAS NMR spectra of samples recrystallised from deuterated solvents provide a straightforward means to assist the identification, assignment and investigation of proton resonance lines.

As an example, in L-histidine hydrochloride monohydrate recrystallised from D_2O, the quadrupole coupling parameters were determined with the aid of the 2D ^{2}H DQ OMAS experiment and compared with values obtained from quantum-chemical calculations. Apart

from structural aspects, also questions of molecular dynamics could be addressed, namely the rotation of the ammonium group and the 180° flip of the crystal water, which were both reflected by motional averaging of the quadrupole interaction tensor. The comparison with quantum-chemical calculations revealed that quadrupole coupling parameters are especially sensitive to the geometry of hydrogen bonds. In a full analysis, temperature effects need to be considered in the calculations. The experiments performed on alkylamines (chapter 3.1) showed that the ^{2}H 2D DQ OMAS experiment is particularly suited for investigating mobilities of different (spectrally resolved) positions in a molecule in temperature-dependent experiments.

Furthermore, ^{7}Li quadrupole parameters of lithium intercalated into TiO_2 were determined by NMR experiments performed under static and MAS conditions (chapter 3.2), and could provide information on the crystal geometry. For the determination of ^{7}Li -^{7}Li dipole-dipole couplings, multiple-quantum NMR experiments were performed. A Li_xTiO_2 sample that, according to X-ray diffraction, seemed to be amorphous, turned out to be nanocrystalline in NMR experiments. This demonstrates that these NMR methods are highly suited for the investigation of systems that lack long-range order and can therefore not be characterised by scattering techniques alone.

Turning to the accuracy achievable by recoupling NMR techniques under fast MAS, in chapter 3.3, the ^{1}H -^{13}C REREDOR experiment was found to be capable of determining strong proton-carbon dipole-dipole couplings with an accuracy of 500 Hz, corresponding to a determination of proton-carbon chemical-bond lengths with picometer accuracy. It was found that the limiting factor of the precision is not the experimental setup, but the influence of additional dipole-dipole couplings arising from neighbouring protons. In dense proton systems, these give rise to a multitude of additional geometrical parameters which cannot possibly be handled in the analysis of the data, not only because of their sheer number, but also because multiple sets of parameters would lead to indistinguishable experimental results.

In the second part of this work (chapter 4), solid-state NMR experiments were combined with quantum-chemical calculations in order to aid and optimise the interpretation of experimental results. The investigations on Calix[4]hydroquinone nanotubes (chapter 4.1) have shown that this combined approach can provide information on the presence of disordered and/or mobile species in supramolecular structures. In particular, the sensitivity of ^{1}H chemical shifts on hydrogen bonds and π-shift effects made it possible to determine the position of the acetone molecules trapped inside the CHQ bowls.

As a second example, C_3-symmetric discs arranging in helical columnar stacks were in-

vestigated in chapter 4.2. In these systems, ^{1}H chemical shifts experience large π-shifts due to packing effects, which were found to be long-ranged, as the calculation of three stacked molecules did not yet match the experimental values, but rather represented a principal trend. Moreover, quantum-chemical calculations revealed that helicity in these systems is induced by the propeller-like conformation of the core of the molecules. The influence of packing effects on ^{13}C chemical shifts is of the same order as for ^{1}H chemical shifts (in ppm) and, therefore, relatively small on the ^{13}C NMR scale. However, the combination of ^{13}C chemical shifts obtained from quantum-chemical calculations and experimental ^{1}H -^{13}C correlation spectra has proven to be particularly helpful to assist the proton assignment.

Thus, the work presented in this thesis demonstrates, firstly, how dipolar (^{1}H -^{1}H , ^{1}H -^{13}C , ^{7}Li -^{7}Li and others) and quadrupolar (^{2}H , ^{7}Li) recoupling techniques in solid-state MAS NMR can help to investigate and to understand the phenomena responsible for structure formation in supramolecular aggregates. Secondly, the findings of this thesis show how the combination of different fields and approaches, namely spectroscopy on the experimental side and quantum-chemical computations on the theoretical side, substantially aids the interpretation of data, triggers new methodological developments on both sides and, thus, opens up new possibilities for tackling questions and problems as complex as the characterisation of structure and dynamics of supramolecular architectures and nanostructured materials.

Appendix A

Experimental Details

Instrumentation and experimental parameters
^{1}H , ^{2}H , and ^{13}C MAS NMR experiments were carried out on a digital Bruker DRX spectrometer with a 16.4 T magnet (54 mm bore) corresponding to ^{1}H , ^{2}H , and ^{13}C resonance frequencies of 700.13 MHz, 107.47 MHz, and 176.05 Mhz, respectively. Magic-angle spinning experiments were performed on commercial 2.5 mm double resonance probes (manufactured by Bruker) at spinning speeds ranging from 15 kHz to 32 kHz. The $\frac{\pi}{2}$ pulse length was set to 2.5 μs for all nuclei. In all ^{13}C detected experiments TPPM decoupling was applied for dipolar decoupling. Static ^{2}H experiments on L-histidine hydrochloride monohydrate were carried out on the same probehead; static ^{2}H experiments on NBZOH were carried out on a static single resonance probehead using $\frac{\pi}{2}$ pulse lengths of 4 μs. The echo delay time was 20 μs.

^{1}H and ^{2}H spectra were referenced to H_2O and D_2O (4.8 ppm), respectively; ^{13}C spectra were referenced to the methyne resonance of alanine (51 ppm). If not stated otherwise, all spectra were recorded with bearing gas at room temperature, leading to effective sample temperatures due to frictional heating under MAS as desribed in the following section.

^{7}Li spectra were recorded on a digital Bruker DSX spectrometer with a 11.74 T magnet, corresponding to ^{1}H and ^{7}Li resonance frequencies of 500.12 MHz and 194.37 MHz, respectively. A commercial 4 mm double resonance probe was used for MAS and static ^{7}Li experiments. ^{7}Li spectra were referenced to a 10M solution of LiCl in H_2O (0 ppm).

Temperature calibration
Temperature calibration under MAS was performed using vanadocene as a temperature standard [Koehler 97]. For a spinning frequency of 30 Khz and a bearing gas pressure

of about 3.6 bar, the sample temperature is about 30 K higher than the bearing gas temperature; for 15 kHz MAS and 2.5 bar bearing pressure the temperature is shifted by about +6 K.

Quadrupole coupling parameters of NBZOH

Static spectra recorded on NBZOH were carried out on different sample temperatures. The extracted quadrupole coupling parameters are given in the following table:

Table A.1: *Quadrupole coupling parameters of NBZOH.*

sample temperature	$\frac{\delta}{2\pi}$	η
300 K	107 kHz	0.13
310 K	105 kHz	0.14
320 K	103 kHz	0.15
330 K	101 kHz	0.16

Appendix B

Quantum-Chemical Calculations

^{2}H quadrupole coupling parameters of L-histidine hydrochloride monohydrate
The calculations of electric field gradient (EFG) tensors were performed by Jochen Schmidt. A module for the calculation EFG tensors was implemented within the pseudopotential plane wave programme package CPMD [Hutter 03] and tested on a single water molecule [Schmidt 04]. The calculations were carried out within density functional theory (DFT) using a fully periodic description of the systems, pseudopotentials of the Goedecker type [Goedecker 96], and a plane wave cutoff of 110 Ry. The BLYP gradient-corrected exchange-correlation functional [Becke 88, Lee 88] was applied in all calculations. In a first step, the EFG tensors were calculated for the equilibrium structure as obtained from geometry optimisation. Then, to account for temperature effects, a molecular dynamics (MD) simulation was performed, in which the system was heated to 300 K, and the EFG tensor was calculated for each step of the MD and subsequently averaged.

^{13}C and ^{1}H chemical shifts of CHQ nanotubes
Carbon chemical shifts of a single CHQ were calculated using the program package TURBOMOLE [Ahlrichs 89] at the Hartree-Fock level using a polarized split-valence (SVP) basis [Schäfer 92], after a geometry optimisation carried out at the RI-DFT level using the BP86 functional [Parr 89, Perdew 86, Becke 88] and a SVP basis.
^{1}H NMR spectra were calculated by Dr. Daniel Sebastiani within density functional theory (DFT) using a fully periodic description of the systems within the pseudopotential plane wave programme package CPMD [Hutter 03]. The atomic coordinates were initially taken from X-ray data and subsequently relaxed until the forces fell below 10^{-3} atomic units, using pseudopotentials of the Goedecker type [Goedecker 96] and

a plane wave cutoff of 70 Ry. The BLYP gradient-corrected exchange-correlation functional [Becke 88, Lee 88] was applied in all calculations. The shieldings so obtained were referenced to tetramethylsilane values calculated under the same computational conditions.
The geometry of a CHQ/acetone complex (see Fig. 4.8a) was optimised at the MP2 level using a 6-31G basis set and computed the BSSE-corrected MP2-adsorption energy using a 6-31G(d) basis with the GAUSSIAN98 code [Frisch 98]. In order to separate the dispersion attraction from the hydrogen bonding energy, a full and a partial geometry optimization were done, the former only relaxing the intramolecular degrees of freedom of the two fragments. We found a van-der-Waals interaction of about 12 kJ/mol and a full adsorption energy (including a H-bond CHQ–acetone) of 68 kJ/mol.
The energy hypersurface is very flat and rich in local minima. Thus, for a complete analysis of the finite temperature NMR chemical shifts, one would have to resort to a statistical sampling as in [Sebastiani 02]. Here, a representative acetone position was taken from the partial geometry optimisation done at the MP2 level, and inserted in the periodic nanotube. Four acetone molecules were placed inside a unit cell, which corresponds to filling each CHQ bowl with one acetone molecule. Their exact positions were slightly randomized to yield a better statistics of the chemical shifts, which were subsequently averaged. Intrinsic errors in the calculations such as the use of DFT, incomplete basis sets, pseudopotential approximation, and especially the neglection of temperature effects in these calculations may lead to an estimated maximum error of 1 - 2 ppm.

^{1}H and ^{13}C chemical shifts of C_3-symmetrical discs

All calculations on the C_3-symmetrical discs were performed by Thorsten Metzroth (University of Mainz) using the TURBOMOLE programm package [Ahlrichs 89]. The geometry of the simplified system (see Fig. 4.17) was optimised at the density-functional theory (DFT) level [Parr 89] using the B-LYP functional [Lee 88, Becke 88] as well as the second-order Møller-Plesset theory level [Moeller 34] using a polarised split-valence basis [Schäfer 92] as well as the RI (resolution of identity) [Eichkorn 95] approximation. Single-point calculations were performed for a dimeric system, constructed by using the optimised monomer geometry and assuming an inter-molecular distance determined by X-ray scattering (3.5 Å) [Gorp 05], for a series of twisting angles. NMR chemical shifts were computed at the DFT level using the Becke 3 parameter hybrid functional (B3-LYP[Becke 93])/SVP for the monomer and a trimer constructed by twisting the molecules by the optimal angle determined from the dimer. The chemical shifts were referenced to TMS calculated under the same conditions. In NMR chemical shift calcu-

lations, gauge origin independence is ensured by gauge-including atomic orbitals (GIAO) [London 37, Ditchfield 74, Wolinski 90]. The used method/basis-set combinations were tested for a smaller system, the details of the calculations are subject of a future publication [Metzroth 04].

Appendix C

Irreducible Spherical Tensors

If the Hamiltonian of an interaction in cartesian coordinates is given as a bilinear product

$$\hat{H} = \underline{\hat{I}} \cdot \underline{\underline{A}} \cdot \underline{L} = \begin{pmatrix} \hat{I}_1 & \hat{I}_2 & \hat{I}_3 \end{pmatrix} \begin{pmatrix} a_{11} & a_{12} & a_{13} \\ a_{21} & a_{22} & a_{23} \\ a_{31} & a_{32} & a_{33} \end{pmatrix} \begin{pmatrix} L_1 \\ L_2 \\ L_3 \end{pmatrix} \tag{C.1}$$

the spherical tensor representation reads as

$$\hat{H} = \sum_{k=0}^{2} \sum_{q=-k}^{k} (-1)^q A_{kq} \hat{T}_{k-q} \tag{C.2}$$

with the irreducible spherical spin tensor operators $\hat{T}_{k-q}$ that are listed in table C.1 for the most common interactions.

The spherical tensor components A_{kq} of the space part can be expressed by the Cartesian tensor components A_{ij} $(i, j = x, y, z)$:

$$\begin{aligned}
\underline{A}_0: \quad A_{00} &= \tfrac{1}{3}(A_{xx} + A_{yy} + A_{zz}) = \tfrac{1}{3}\mathsf{Tr}[A] \\
\\
\underline{A}_1: \quad A_{10} &= -\tfrac{i}{\sqrt{2}}(A_{xy} - A_{yx}) \quad \left\{ \overset{PAS}{=} -i\sqrt{2}A_{xy} \right\} \\
A_{1\pm1} &= -\tfrac{1}{2}\{(A_{zx} - A_{xz}) \pm i(A_{zy} - A_{yz})\} \quad \left\{ \overset{PAS}{=} A_{xz} \pm iA_{yz} \right\} \\
\\
\underline{A}_2: \quad A_{20} &= \sqrt{\tfrac{3}{2}}(A_{zz} - A_{00}) \quad \left\{ \overset{PAS}{=} \sqrt{\tfrac{3}{2}}\delta \right\} \\
A_{2\pm1} &= \mp\{(A_{zx} + A_{xz}) \pm i(A_{zy} + A_{yz})\} \quad \left\{ \overset{PAS}{=} 0 \right\} \\
A_{2\pm2} &= \tfrac{1}{2}\{(A_{xx} - A_{yy}) \pm i(A_{xy} + A_{yx})\} \quad \left\{ \overset{PAS}{=} -\tfrac{1}{2}\delta\eta \right\}
\end{aligned} \tag{C.3}$$

The last terms in curly brackets are the tensor components in the principal axis system (PAS) with the anisotropy parameter, δ, and the asymmetry parameter, η.

As described in Chapter 2, the evaluation of most NMR experiments involves rotations of the interaction tensors. In general any rotation can be specified by using three Euler angles α, β, and γ defined as:

α: rotation about the original z axis
β: rotation about the new y' axis
γ: rotation about the final z" axis

The rotation of a tensor T, which is expressed by the components of a spherical tensor, is given by

$$T'_{kq} = \sum_{p=-k}^{+k} T_{kp} D^k_{pq}(\alpha, \beta, \gamma) \tag{C.4}$$

with the Wigner rotation matrices D^k_{pq}

$$D^k_{pq} = d^k_{pq}(\beta) e^{-ip\alpha} e^{-iq\gamma}. \tag{C.5}$$

The elements d^k_{pq} of the reduced rotation matrices are listed in Table C.2 and C.3. A detailed description of the spherical tensor representation and its transformations can be found in [Mehring 83].

Table C.1: *Spherical tensor representation of spin operators (with $\hat{I}_\pm = \hat{I}_x \pm i\hat{I}_y$)*

Interaction	T_{00}	T_{10}	$T_{1\pm1}$	T_{20}	$T_{2\pm1}$	$T_{2\pm2}$
Chemical shift	$-\frac{1}{\sqrt{3}}\hat{I}_z B_0$	0	$-\frac{1}{2}\hat{I}_\pm B_0$	$\sqrt{\frac{2}{3}}\hat{I}_z B_0$	$\mp\frac{1}{2}\hat{I}_\pm B_0$	0
Dipole-dipole	0	0	0	$\frac{1}{\sqrt{6}}\left(3\hat{I}_z\hat{S}_z - \underline{\hat{I}\hat{S}}\right)$	$\mp\frac{1}{2}\left(\hat{I}_z\hat{S}_\pm + \hat{I}_\pm\hat{S}_z\right)$	$\frac{1}{2}\hat{I}_\pm\hat{S}_\pm$
Quadrupole	0	0	0	$\frac{1}{\sqrt{6}}\left(3\hat{I}_z^2 - I(I+1)\right)$	$\mp\frac{1}{2}\left(\hat{I}_z\hat{I}_\pm + \hat{I}_\pm\hat{I}_z\right)$	$\frac{1}{2}\hat{I}_\pm\hat{I}_\pm$

Table C.2: Reduced Wigner rotation matrix elements $d^{(1)}_{pq}$

p \ q	1	0	−1
1	$\frac{1}{2}(1+\cos\beta)$	$-\frac{1}{\sqrt{2}}\sin\beta$	$\frac{1}{2}(1-\cos\beta)$
0	$\frac{1}{\sqrt{2}}\sin\beta$	$\cos\beta$	$-\frac{1}{\sqrt{2}}\sin\beta$
−1	$\frac{1}{2}(1-\cos\beta)$	$\frac{1}{\sqrt{2}}\sin\beta$	$\frac{1}{2}(1+\cos\beta)$

Table C.3: Reduced Wigner rotation matrix elements $d^{(2)}_{pq}$

p \ q	2	1	0	−1	−2
2	$\frac{1}{4}(1+\cos\beta)^2$	$-\frac{1}{2}(1+\cos\beta)\sin\beta$	$\sqrt{\frac{3}{8}}\sin^2\beta$	$-\frac{1}{2}(1-\cos\beta)\sin\beta$	$\frac{1}{4}(1-\cos\beta)^2$
1	$\frac{1}{2}(1+\cos\beta)\sin\beta$	$\cos^2\beta - \frac{1}{2}(1-\cos\beta)$	$-\sqrt{\frac{3}{8}}\sin 2\beta$	$\frac{1}{2}(1+\cos\beta) - \cos^2\beta$	$-\frac{1}{2}(1-\cos\beta)\sin\beta$
0	$\sqrt{\frac{3}{8}}\sin^2\beta$	$\sqrt{\frac{3}{8}}\sin 2\beta$	$\frac{1}{2}(3\cos^2\beta - 1)$	$-\sqrt{\frac{3}{8}}\sin 2\beta$	$\sqrt{\frac{3}{8}}\sin^2\beta$
−1	$\frac{1}{2}(1-\cos\beta)\sin\beta$	$\frac{1}{2}(1+\cos\beta) - \cos^2\beta$	$\sqrt{\frac{3}{8}}\sin 2\beta$	$\cos^2\beta - \frac{1}{2}(1-\cos\beta)$	$-\frac{1}{2}(1+\cos\beta)\sin\beta$
−2	$\frac{1}{4}(1-\cos\beta)^2$	$\frac{1}{2}(1-\cos\beta)\sin\beta$	$\sqrt{\frac{3}{8}}\sin^2\beta$	$\frac{1}{2}(1+\cos\beta)\sin\beta$	$\frac{1}{4}(1+\cos\beta)^2$

Appendix D

Integrated Quadrupolar Phase for the Five-Pulse Sequence under OMAS Conditions

In general, the integrated quadrupolar phase under off-magic-angle spinning conditions can be calculated as:

$$\Omega_{\mathrm{Q}}|_{t_1}^{t_2} = \int_{t_1}^{t_2} A_{20}^{Q,LAB}(t)dt \tag{D.1}$$

$$\begin{aligned}
&= \delta\frac{3}{8\omega_{\mathrm{R}}}\sin^2(\beta)\sin^2(\beta_{\mathrm{M}})\left[\sin(2\omega_{\mathrm{R}}t_2+2\gamma)-\sin(2\omega_{\mathrm{R}}t_1+2\gamma)\right]\\
&- \delta\frac{3}{4\omega_{\mathrm{R}}}\sin(2\beta)\sin(2\beta_{\mathrm{M}})\left[\sin(\omega_{\mathrm{R}}t_2+\gamma)-\sin(\omega_{\mathrm{R}}t_1+\gamma)\right]\\
&+ \delta\frac{1}{4}(3\cos^2(\beta)-1)(3\cos^2(\beta_{\mathrm{M}})-1)(t_2-t_1)\\
&+ \delta\eta\frac{1}{16\omega_{\mathrm{R}}}(1-\cos(\beta))^2\sin^2(\beta_{\mathrm{M}})\left[\sin(2\omega_{\mathrm{R}}t_2+2\gamma-2\alpha)-\sin(2\omega_{\mathrm{R}}t_1+2\gamma-2\alpha)\right]\\
&+ \delta\eta\frac{1}{16\omega_{\mathrm{R}}}(1+\cos(\beta))^2\sin^2(\beta_{\mathrm{M}})\left[\sin(2\omega_{\mathrm{R}}t_2+2\gamma+2\alpha)-\sin(2\omega_{\mathrm{R}}t_1+2\gamma+2\alpha)\right]\\
&- \delta\eta\frac{1}{4\omega_{\mathrm{R}}}(1-\cos(\beta))\sin(\beta)\sin(2\beta_{\mathrm{M}})\left[\sin(\omega_{\mathrm{R}}t_2+\gamma-2\alpha)-\sin(\omega_{\mathrm{R}}t_1+\gamma-2\alpha)\right]\\
&+ \delta\eta\frac{1}{4\omega_{\mathrm{R}}}(1+\cos(\beta))\sin(\beta)\sin(2\beta_{\mathrm{M}})\left[\sin(\omega_{\mathrm{R}}t_2+\gamma+2\alpha)-\sin(\omega_{\mathrm{R}}t_1+\gamma+2\alpha)\right]\\
&+ \delta\eta\frac{1}{4}(3\cos^2(\beta_{\mathrm{M}})-1)\sin^2(\beta)\cos(2\alpha)(t_2-t_1)
\end{aligned} \tag{D.2}$$

Bibliography

[Abragam 61] A. Abragam. The Principles of Nuclear Magnetism. Oxford Univ. Press, Oxford (1961).

[Ahlrichs 89] R. Ahlrichs, M. Bär, M. Häser, H. Horn, C. Kölmel. Electronic Structure Calculations on Workstation Computers: The Program System Turbomole. *Chem. Phys. Lett.* **162**, 165–169 (1989).

[Andrew 58] E. R. Andrew, A. Bradbury, R. G. Eades. Nuclear Magnetic Resonance Spectra from a Crystal Rotated at High Speed. *Nature* **182**, 1659 (1958).

[Ashbrook 02] S. E. Ashbrook, Sasa Antonijevic, Andrew J. Berry, Stephen Wimperis. Motional Broadening: An Important Distinction Between Multiple-Quantum and Satellite-Transition MAS NMR of Quadrupolar Nuclei. *Chem. Phys. Let.* **364**, 634–642 (2002).

[Bak 00] M. Bak, J. T. Rasmussen, N. C. Nielsen. SIMPSON: A General Simulation Program for Solid-State NMR Spectroscopy. *J. Magn. Reson.* **147**, 296–330 (2000).

[Becke 88] A. D. Becke. Density-functional Exchange-energy Approximation with Correct Asymptotic-Behavior. *Phys. Rev. A* **38**, 3098–3100 (1988).

[Becke 93] A.D. Becke. Density-functional thermochemistry. III. The role of exact exchange. *J. Chem. Phys.* **98**, 5648 (1993).

[Bennett 95] A. E. Bennett, C. M. Rienstra, M. Auger, K. V. Lakshmi, R. G. Griffin. Heteronuclear Decoupling in Rotating Solids. *J. Chem. Phys.* **103**, 6951–6958 (1995).

[Bloch 46] F. Bloch. Nuclear Induction. *Phys. Rev.* **70**, 460–474 (1946).

[Blümich 90] B. Blümich, A. Hagemeyer, D. Schaefer, K. Schmidt-Rohr, H. W. Spiess. Solid State NMR Spectroscopy in Polymer Science. *Adv. Mat.* **2**, 72–81 (1990).

[Brinkmann 00] A. Brinkmann, M. Edén, M. H. Levitt. Synchronous Helical Pulse Sequences in Magic-angle Spinning Nuclear Magnetic Resonance. *J. Chem. Phys.* **112**, 8539–8554 (2000).

[Brown 01] S. P. Brown, H. W. Spiess. Advanced Solid-state NMR Methods for the Elucidation of Structure and Dynamics of Molecular, Macromolecular and Supramolecular systems. *Chem. Rev.* **101**, 4125–4155 (2001).

[deAzevedo 99] E. R. deAzevedo, W.-G. Hu, T. J. Bonagamba, K. Schmidt-Rohr. Centerband-Only Detection of Exchange: Efficient Analysis of Dynamics in Solids by NMR. *J. Am. Chem. Soc.* **121**, 8411–8412 (1999).

[Ditchfield 74] R. Ditchfield. Self-consistent Perturbation-Theory of Diamagnetism. 1. Gauge-invariant LCAO Method for NMR Chemical-shifts. *Mol. Phys.* **27**, 789–807 (1974).

[Dusold 00] S. Dusold, A. Seebald. Dipolar recoupling under magic angle spinning conditions. *Ann. Rep NMR Spectrosc.* **41**, 185 (2000).

[Eichkorn 95] K. Eichkorn, O. Treutler, H.Öhm, M. Häser, R. Ahlrichs. Auxiliary basis sets to approximate Coulomb potentials. *Chem. Phys. Lett.* **242**, 652 (1995).

[Ernst 87] R. R. Ernst, G. Bodenhausen, A. Wokaun. Principles of Nuclear Magnetic Resonance in One and Two Dimensions. Clarendon Press, Oxford (1987).

[Feike 96] M. Feike, D. E. Demco, R. Graf, J. Gottwald, S. Hafner, H. W. Spiess. Broadband Multiple-Quantum NMR Spectroscopy. *J. Magn. Reson. A* **122**, 214–221 (1996).

[Fischbach 03a] I. Fischbach. *Supramolecular Order and Dynamics of Discotic Materials Studied by Solid-State NMR Recoupling Methods*. Doktorarbeit, Universität Mainz (2003).

[Fischbach 03b] I. Fischbach, K. Thieme, A. Hoffmann, M. Hehn, I. Schnell. PFG-Assisted Selection and Suppression of ^{1}H NMR Signals in the Solid State under fast MAS. *J. Magn. Res.* **65**, 102–115 (2003).

[Friedrich 98] U. Friedrich, I. Schnell, S. P. Brown, A. Lupulescu, D. E. Demco, H. W. Spiess. Spinning-sideband patterns in multiple-quantum magic-angle spinning NMR spectroscopy. *Mol. Phys.* **95**, 1209–1227 (1998).

[Frisch 98] M. J. Frisch et al. Computer code Gaussian 98, Revision A.7 (1998).

[Goedecker 96] S. Goedecker, M. Teter, J. Hutter. Separable dual-space Gaussian pseudopotentials. *Phys. Rev. B* **54**, 1703 (1996).

[Gorp 05] J. J. van Gorp, Y. Kamikawa, J. A. J. M. Vekemans, E.W. Meijer, T. Kato. Thermotropic Helical liquid crystalline phases of C_3-symmetrical triamides and triureas. *prepared for publication* (2005).

[Gullion 89a] T. Gullion, J. Schaefer. Detection of Weak Heteronuclear Dipolar Coupling by Rotational-Echo Double-Resonance Nuclear Magnetic Resonance. *Adv. Magn. Reson.* **13**, 57–83 (1989).

[Gullion 89b] T. Gullion, J. Schaefer. Rotational-Echo Double-Resonance NMR. *J. Magn. Reson.* **81**, 196–200 (1989).

[Gullion 90] T. Gullion, D. B. Baker, M. S. Conradi. New, Compensated Carr-Purcell Sequences. *J. Magn. Reson.* **89**, 479–484 (1990).

[Gullion 97] T. Gullion. Measurement of Heteronuclear Dipolar Interactions by Rotational-Echo, Double-Resonance Nuclear Magnetic Resonance. *Magn. Reson. Rev.* **17**, 83–131 (1997).

[Hahn 50] E. L. Hahn. Spin Echoes. *Phys. Rev.* **80**, 580–594 (1950).

[Hodgkinson 97] P. Hodgkinson, L. Emsley. The reliability of the determination of tensor parameters by solid-state nuclear magnetic resonance. *J. CHem. Phys.* **3107**, 4808–4816 (1997).

[Hoffmann 04] A. Hoffmann, D. Sebastiani, E. Sugiono, S. Yun, K. S. Kim, H. W. Spiess, I. Schnell. *Chem. Phys Let.* **388**, 164–169 (2004).

[Hong 01a] B. H. Hong, S. C. Bae, C.-W. Lee, S. Jeong K. S. Kim. Ultrathin Single-Crystalline Silver Nanowire Arrays Formed in an Ambient Solution Phase. *Science* **294**, 348–351 (2001).

[Hong 01b] B. H. Hong, J. Y. Lee, C.-W. Lee, J. C. Kim, S. C. Bae, K. S. Kim. Self-Assembled Arrays of Organic Nanotubes with Infinitely Long One-Dimensional H-Bond Chains. *J. Am. Chem. Soc.* **123**, 10748–10749 (2001).

[Hunt 74] M. J. Hunt, A. L. Mackay. Deuterium and Nitrogen Pure Quadrupole-Resonance in Deuterated Amino-Acids. *J. Magn. Reson.* **15**, 402–414 (1974).

[Hutter 03] J. Hutter et al. Computer code CPMD, version 3.8 (2003). Copyright IBM Corp. and MPI-FKF Stuttgart 1990-2003, `http://www.cpmd.org`.

[Ikeda 97] A. Ikeda, S. Shinkai. Novel Cavity Design Using Calix[n]arene Skeletons: Toward Molecular Recognition and Metal Binding. *Chem. Rev.* **97**, 1713–1734 (1997).

[Jaroniec 00] C. P. Jaroniec, B. A. Tounge, C. M. Riestra, J. Herzfeld, R. G. Griffin. Recoupling of Heteronuclear Dipolar Interactions with Rotational-Echo Double-Resonance at High Magic-Angle Spinning Frequencies. *J. Magn. Res.* **146**, 132–139 (2000).

[Jurga 91] S. Jurga, V. Macho, G. Hueser, H. W. Spiess. Chain Dynamics of Bilayer n-Decylammonium Chloride Studied by Deuteron NMR Spectroscopy. *Z. Phys. B.* **84**, 43–49 (1991).

[Kim 02a] K. S. Kim. Self-assembled organic nanotubes and self-synthesized silver subnanowire arrays in an ambient solution phase. *Cur. Appl. Phys* **2**, 65–69 (2002).

[Kim 02b] K. S. Kim, S. B. Suh, J. C. Kim, Byung Hee Hong, Eun Cheol Lee, Sunggoo Yun, P. Tarakeshwar, Jin Yong Lee, Yukyung Kim, Hyejae Ihm, Heon Gon Kim, Jung Woo Lee, Jung Kyung Kim, Han Myoung Lee, Dongwook Kim, Chunzhi Cui, Suk Joo Youn, Hae Yong Chung, Hyuck Soon Choi, Chi-Wan Lee, Seung Joo Cho, Sukmin Jeong, Jun-Hyung Cho. Assembling Phenomena of Calix[4]hydroquinone Nanotube Bundles by One-Dimensional Short Hydrogen Bonding and Displaced π-π Stacking. *J. Am. Chem. Soc.* **124**, 14268–14279 (2002).

[Koehler 97] Frank H. Koehler, Xiulan Xie. Vanadocene as a Temperature Standard for 13C and and for Solution-State 1H MAS NMR NMR Spectroscopy. *Magnetic Resonance in Chemistry* **35**, 487–492 (1997).

[Kolbert 90] A. C. Kolbert, D. P. Raleigh, R. G. Griffin, M. H. Levitt. Spinning sideband enhancement using a rotary resonant field. *J. Magn. Reson.* **89**, 133–138 (1990).

[Koudriachowa 02] M. V. Koudriachowa, N. M. Harrison, S. W. de Leeuw. Open circuit voltage profile for Li-intercalation in rutile and anatase from first principles. *Solid State Ionics* **152-153**, 189–194 (2002).

[Koudriachowa 03] M. V. Koudriachowa, N. M. Harrison, S. W. de Leeuw. Diffusion of Li-ions in rutile. An ab initio study. *Solid State Ionics* **157**, 35–38 (2003).

[Lee 88] C. Lee, W. Yang, R.G. Parr. Development of the Colle-Salvetti correlation-energy formula into a functional of the electron density. *Phys. Rev. B* **37**, 785 (1988).

[Lee 95] Y. K. Lee, N. D. Kurur, M. Helmle, O. G. Johannessen, N. C. Nielsen, M. H. Levitt. Efficient Dipolar Recoupling in the NMR of Rotating Solids. A Sevenfold Symmetric Radiofrequency Pulse Sequence. *Chem. Phys. Lett.* **242**, 304–309 (1995).

[Lehn 78] J.-M. Lehn. Cryptates - Inclusion Complexes of Macropolycyclic Receptor Molecules. *Pure Appl. Chem.* **50**, 871–892 (1978).

[Leverd 00] P. C. Leverd, P. Bethault, M. Lance, M. Nierlich. Successive Inclusion of Water, [H3NCH2CH2NH3]2+ and [H3NCH2CH2NH2]+ in the Aromatic Cavity of (p-Sulfonato)calix[4]arene. *Eur. J. Org. Chem.* **1**, 133–139 (2000).

[Levitt 01] M. Levitt. Spin Dynamics. J. Wiley & Sons Ltd., Chichester (2001).

[London 37] F. London. *J. Phys. Rad.* **8**, 397 (1937).

[Lowe 59] I. J. Lowe. Free Induction Decays of Rotating Solids. *Phys. Rev. Lett.* **2**, 285–287 (1959).

[Lu 99] G. Y. Lu, F. Liu, Y. J. Liu, W. J. He, Q. Li, L. G. Zhu. Crystal structure of the molecular inclusion complex of 5, 17-di-t-butyl-26, 28-disubstituted calix[4]arene with acetone (1:3). *J. Chem. Cryst.* **29**, 1121–1125 (1999).

[Lu 00] G. Y. Lu, W. Song, X. B. Wan. Crystal structure of the molecular inclusion complex tetra-p-nitro-tetra-O-butyl calix[4]arene with acetone (1:2) . *J. Chem. Cryst.* **30**, 185–188 (2000).

[Macho 01] V. Macho, L. Brombacher, H. W. Spiess. The NMR-WEBLAB: an Internet Approach to NMR Lineshape Analysis. *Appl. Magn. Res.* **20**, 405–432 (2001).

[Maricq 79] M. M. Maricq, J. S. Waugh. NMR in Rotating Solids. *J. Chem. Phys.* **70**, 3300–3316 (1979).

[Marion 83] D. Marion, K. Wüthrich. Application of Phase Sensitive Two-dimensional Correlated Spectroscopy (COSY) for Measurements of H-1 H-1 Spin-spin Coupling-constants in Proteins. *Biochem. Biophys. Res. Commun.* **113**, 967–974 (1983).

[Marion 89] D. Marion, M. Ikura, R. Tschudin, A. Bax. Rapid Recording of 2D NMR-Spectra without Phase Cycling- Application to the Study of Hydrogen-Exchange in Proteins. *J. Magn. Res.* **85**, 393–399 (1989).

[Mehring 83] M. Mehring. High Resolution NMR of Solids. Springer-Verlag, Berlin (1983).

[Metz 94] G. Metz, X. Wu, S. O. Smith. Ramped-Amplitude Cross Polarization in Magic-Angle-Spinning NMR. *J. Magn. Reson. A* **110**, 219–227 (1994).

[Metzroth 04] T. Metzroth, A. Hoffmann, A. Rapp, Meijer and coworkers, H. W. Spiess, I.Schnell, J. Gauss. Structure and Stacking Behaviour of C_3-symmetrical Discotics Determined by Quantum-Chemical Calculations and Fast-MAS Spectroscopy (2004). publication in preparation.

[Moeller 34] C. Moeller, M. S. Plesset. Note on an Approximation Treatment for Many-Electron Systems. *Phys. Rev.* **46**, 618 (1934).

[Namor 98] A. F. D. de Namor, R. M. Cleverley, M. L. Zapata-Ormachea. Thermodynamics of Calixarene Chemistry. *Chem. Rev.* **98**, 2495–2525 (1998).

[Ochsenfeld 01] C. Ochsenfeld, S. P. Brown, I. Schnell, J. Gauss, H. W. Spiess. Structure assignment in the solid state by the coupling of quantum mechanical calculations with NMR experiments: A columnar hexabenzocoronene derivative. *J. Am. Chem. Soc.* **123**, 2597–2606 (2001).

[Ochsenfeld 02] C. Ochsenfeld, F. Koziol, S. P. Brown, T. Schaller, U. P. Seelbach, F.-G. Klärner. A Study of a Molecular Tweezer Host-Guest System by a Combination of Quantum-Chemical Calculations and Solid-State NMR Experiments. *Solid-State Nucl. Magn. Reson.* **22**, 128–153 (2002).

[Palmans 97] A.R.A. Palmans, J.A.J.M. Vekemans, H. Fischer, R.A. Hikmet, E.W. Meijer. Extended-Core Discotic Liquid Crystal Based on the Intramolecular H-Bonding in *N*-Acylated 2,2'-Bipyridine-3,3'-diamine Moieties. *Chem. Eur. J.* **3**, 300 (1997).

[Parr 89] R. G. Parr, W. Yang. Density Functional Theory of Atoms and Molecules. Oxford University Press, New York (1989).

[Perdew 86] J. P. Perdew. Density-Functional Approximation for the Correlation-energy of the Inhomogeneous Electron-gas. *Phys. Rev. B* **33**, 8822–8824 (1986).

[Pines 72] A. Pines, W.-K. Rhim, J. S. Waugh. Homogeneous and Inhomogeneous Nuclear Spin Echos in Solids. *J. Magn. Reson.* **6**, 457–465 (1972).

[Pines 73] A. Pines, M. G. Gibby, J. S. Waugh. Proton-enhanced NMR of Dilute Spins in Solids. *J. Chem. Phys.* **59**, 569–590 (1973).

[Purcell 46] E. M. Purcell, H. C. Torrey, R. V. Pound. Resonance Absorption by Nuclear Magnetic Moments in Solids. *Phys. Rev.* **69**, 37–38 (1946).

[Rapp 04] A. Rapp. unpublished results (2004).

[Saalwächter 01] K. Saalwächter, R. Graf, H. W. Spiess. Recoupled Polarization-Transfer Methods for Solid-State ^{1}H-^{13}C Heteronuclear Correlation in the Limit of Fast MAS. *J. Magn. Reson.* **148**, 398–418 (2001).

[Saalwächter 02] K. Saalwächter, I. Schnell. REDOR-based Heteronuclear Dipolar Correlation Experiments in Multi-spin Systems: Rotor-encoding, Directing and Multiple Distance and Angle Determination. *Solid State Nucl. Magn. Res.* **22**, 154–187 (2002).

[Samoson 04] Ago Samoson, Tiit Tuherm, Jaan Past, Andres Reinhold, Tiit Anupõld, Ivo Heinmaa. New Horizons for Magic-Angle Spinning NMR. *Topics in Current Chemistry* **246**, 15–31 (2004).

[Schäfer 92] A. Schäfer, H. Horn, R. Ahlrichs. Fully Optimized Contracted Gaussian Basis Sets for Atoms Li to Kr. *J. Chem. Phys.* **97**, 2571–2577 (1992).

[Schmidt-Rohr 94] K. Schmidt-Rohr, H. W. Spiess. Multidimensional Solid-State NMR and Polymers. Academic Press, London (1994).

[Schmidt 04] J. Schmidt. *Analyse experimenteller NMR-Parameter in Festkörpern mittels Computersimulation.* Diploma thesis, University of Mainz (2004).

[Schnell 01a] I. Schnell, H. W. Spiess. ADVANCES IN MAGNETIC RESONANCE High-resolution ^{1}H NMR Spectroscopy in the Solid State: Very Fast Sample Rotation and Multiple-quantum Coherences. *J. Magn. Reson.* **151**, 153–227 (2001).

[Schnell 01b] I. Schnell, A. Watts, H. W. Spiess. Double-Quantum Double-Quantum MAS Exchange NMR Spectroscopy: Dipolar-Coupled Spin Pairs as Probes for Slow Molecular Dynamics. *J. Magn. Reson.* **149**, 90–102 (2001).

[Schulz-Dobric 04] M. Schulz-Dobrick. *Methoden der Festkörper-NMR-Spektroskopie zur Strukturaufklärung an supramolekularen Systemen: Abstandsmessungen zwischen den Kernen ^{1}5N, ^{1}H und ^{2}H.* Diploma thesis, University of Mainz (2004).

[Schulz-Dobric 05] M. Schulz-Dobrick, T. Metzroth, H. W. Spiess, J. Gauss, I. Schnell. Determining the Geometry of Hydrogen Bonds in Solids with Picometer Accuracy by Quantum-Chemical Calculations and NMR Spectroscopy. *ChemPhysChem* **6**, 1–13 (2005).

[Sebastiani 01] D. Sebastiani, M. Parrinello. A new ab-initio approach for the calculation of NMR chemical shifts in periodic systems. *J. Phys. Chem A* **105**, 1951 (2001).

[Sebastiani 02] D. Sebastiani, M. Parrinello. Ab-initio study of NMR chemical shifts of water under liquid and supercritical conditions. *ChemPhysChem* **3**, 675 (2002).

[Sebastiani 03] D. Sebastiani, G. Goward, I. Schnell, H.-W. Spiess. NMR chemical shifts in proton conducting crystals from first principles. *J. Mol. Struct. (THEOCHEM)* **625**, 283–288 (2003).

[Slichter 96] C. P. Slichter. Principles of Magnetic Resonance. Springer-Verlag, Berlin (1996).

[Sørensen 83] O. W. Sørensen, G. W. Eich, M. H. Levitt, G. Bodenhausen, R. R. Ernst. Product Operator Formalism for the Description of NMR Pulse Experiments. *Progr. NMR Spectrosc.* **16**, 163–192 (1983).

[Stejskal 77] E. O. Stejskal, J. Schaefer, R. A. McKay. High-Resolution, Slow-Spinning Magic-Angle Carbon-13 NMR. *J. Magn. Res.* **25**, 569–573 (1977).

[Terao 86] T. Terao, H. Miura, A. Saika. Dipolar SASS NMR spectroscopy: Separation of heteronuclear dipolar powder patterns in rotating solids. *J. Chem. Phys.* **85**, 3816–3826 (1986).

[Udachin 03] K. A. Udachin, G. D. Enright, C. I. Ratcliffe, J. A. Ripmeester. Locating Dynamic Species with X-ray Crystallography and NMR Spectroscopy: Acetone in p-tert-Butylcalix[4]arene . *ChemPhysChem* **4**, 1059–1063 (2003).

[Ungaro 84] R. Ungaro, A. Pochini, G. D. Andreetti, V. Sangermano. *J. Chem. Soc. Perk. Trans.* **2**, 1979–1985 (1984).

[Vosegaard 02] Vosegaard, Malmendal, Nielsen. The Flexibility of SIMPSON and SIMMOL for Numerical Simulations in Solid and Liquid-State NMR Spectroscopy . *Chem. Monthly* **133**, 1555–1574 (2002).

[Wagemaker 01] M. Wagemaker, R. van de Krol, A. P. M. Kentgens, A. A. van Well, F. M. Mulder. Two Phase Morphology Limits Lithium Diffusion in TiO_2

(Anatase): A ^{7}Li MAS NMR Study. *J. Am. Chem. Soc.* **123**, 11454–11461 (2001).

[Wolinski 90] K. Wolinski, J. F. Hinton, P. Pulay. Efficient Implementation of the Gauge-independent Atomic Orbital Method for NMR Chemical-shift Calculations. *J. Am. Chem. Soc.* **112**, 8251–8260 (1990).

[Zhang 92] P. M. Zhang, Z. T. Huang. *Acta Chem. Sin.* **50**, 209–215 (1992).